Ben-Gurion University of the Negev

School of Electrical and Computer Engineering

Electro-Optics and Photonics Engineering Department

Optical nanoantennas for applications in label-free chemical and biological sensors

Daler R. Dadadzhanov

Under the supervision of **Dr. Alina Karabchevsky** and **Dr. Tigran Vartanyan**

Signature of student: _____ Date: 25/10/2020

Signature of supervisors: _____ Date: 25/10/2020

Signature of Graduate Committee: _____ Date: _____

October 2020

Beer-Sheva

Abstract

The most common method for optical sensing of chemical or biological samples involve the need for labels that recognize unknown molecular events due to changes in their intrinsic optical properties. Since the introduction of these labels creates such complications, as the signal interference between a label and an analyte, sensitivity reduction, and additional chemistry treatment to bond the labels to sensing element, hence the label-free sensors are required. These sensors allow for real-time, highly sensitive detection of chemical or biological interaction without the need for labels.

Among the methods of label-free sensing our approach is based on a well-established phenomenon of collective oscillations of free electrons, known as plasmons. Plasmons can be excited in conductive nanoscale objects composed of noble metals, such as Au, Ag, Pt, Cu, provided that the objects' size is much smaller than the wavelength of the incident light [1]. A highly concentrated localized electromagnetic field near the nanoparticles, along with the sensitivity of plasmonic nanoparticles to their surrounding environment, forms the basis for many sensor systems known as localized surface plasmon resonance (LSPR) sensors. Moreover, the optical properties of metal nanoparticles strongly depend on their shape this allows to tune the frequencies of their localized plasmon resonances for more efficient interaction of nanoparticles with chemical or biological entities [2]. The enhancement of local electric fields makes plasmonic nanoparticles useful in a wide variety of fields, such as nonlinear optics, Raman spectroscopy, and vibrational and luminescent spectroscopy.

The purpose of the Ph.D. thesis is the theoretical and experimental study of the interaction of plasmonic nanoparticles with a quantum emitter, quantum absorber, and biological entity.

Keywords: Plasmonic nanoparticles, localized surface plasmon resonance, label-free sensor, chemiluminescence, metal-enhanced chemiluminescence, metasurface, surface-enhanced near-infrared absorption, overtone spectroscopy, endocytosis, nanoparticle uptake

Contents

List of Figures

List of Tables

Scope of the Thesis

Chapter 1 provides the scientific background of the study, while Chapter 2 describes materials and methods used in the thesis. The original results are discussed in Chapters 3 to 5.

Chapter 3 is devoted to the study of the metal-enhanced chemiluminescence effect. Chemiluminescence, which is an emission resulting from the radiative decay of chemically excited species, also has practical applications, especially in sensing technologies. Unlike devices based on photo- and electroluminescence, chemiluminescence-based devices function without external energy sources. Moreover, chemiluminescence lasts for relatively long periods of time, namely from few seconds to several hours, depending on the concentration of oxidizing species, compared to photo/electroluminescence (about 10^{-8} s). A downside of chemiluminescence is its low intensity. In this chapter, I have addressed this limiting factor and explored the possibility to enhance the chemiluminescent intensity by the introduction of metal nanoparticles that support localized surface plasmon oscillations.

The optimization of the metal nanostructure was performed through the numerical modeling of the optical properties of metal nanoparticles arrays, supported by transparent substrates. Additionally, several systems for widely-used chemiluminescence species were found with an excellent overlap between the chemiluminophore emission band and the localized surface plasmon band of metal nanoparticles. Next, silver nanoparticles arrays with suitable properties have been fabricated via physical vapor deposition. A 1.6-fold enhancement of chemiluminescence intensity upon direct contact of the reagents with a granular silver film was demonstrated experimentally. Special experiments have been conducted to prove that the catalytic action of the metal surface is of minor importance and the chemiluminophore–plasmon coupling is the main cause of the enhancement observed. Corresponding results were submitted to *Sensor and Actuator B: Chemical journal*. The paper is currently under review. The submitted version of the paper can be found in **appendix A**.

The results obtained in Chapter 4 demonstrate the influence of a highly localized

electromagnetic field in gold nanoparticles on the weak overtone absorption bands in the near-infrared range. The near-infrared spectral range encloses overtones of vibrational modes belonging to main functional groups of organic molecules. Considering the current development of near-infrared spectroscopic instrumentation, it would be attractive to use overtone transitions in sensor applications, if the probability of transitions could be enhanced to the level comparable with that of the fundamental vibrations. In this work, I have explored the possibility to enhance the overtone transition probability by placing the molecules in the near-field of metal nanoparticles that possess the localized surface plasmon resonances in the actual spectral range

Resonant coupling between plasmonic nanoantennas and molecular vibrational excitations is employed to amplify the weak overtone transitions that reside in the near-infrared spectral range. The differential extinction of molecular overtone transitions coupled to the localized surface plasmons has been explored for the first time. A nontrivial interplay between the molecular absorption enhancement and suppression of plasmonic absorption in a coupled system in differential extinction spectra were shown. The capabilities of surface-enhanced near-infrared absorption for molecular overtones sensing were then investigated using a gold metasurface. The combination of the localized surface plasmon resonance in prolonged nanoparticles and the Rayleigh anomaly of the periodic lattice of nanoparticles results in the enhancement of the N-H overtone transition by 22.5 times. Corresponding results are summarized in two journal publications. The papers [Dadadzhanov D.R. et al, "Differential extinction of vibrational molecular overtone transitions with gold nanorods and its role in surface enhanced near-IR absorption (SENIRA)." Optics express 27.21 (2019): 29471-29478.] and [Dadadzhanov D.R. et al, "Lattice Rayleigh Anomaly Associated Enhancement of NH and CH Stretching Modes on Gold Metasurfaces for Overtone Detection." Nanomaterials 10.7 (2020): 1265.] can be found in **appendix B** and **C**, respectively.

Chapter 5 is devoted to the experimental and theoretical results of the study of the silver nanoparticles for biomedical application. It is well-known that the dipole plasmon band of a sphere corresponds to three degenerate eigenmodes that represent plasmon oscillations in three independent dimensions. When the sphere approaches a plane boundary between two media with different refractive indices, two eigenmodes that correspond to the oscillations parallel to the boundary remain degenerate while the third one corresponding to the dipole oscillation normal to the boundary shifts faster than two others. This phenomenon has been

proposed to monitor endocytosis – the process in which a cell captures solid particles – in far-field spectroscopy. Endocytosis was modeled as a process of single nanoparticle penetration through a thin cell membrane. Numerical studies of this model have shown that when the silver nanoparticle approaches the boundary of the cell membrane, plasmon degeneracy is partially lifted and it can be seen in the far-field spectroscopic measurements. Silver nanoparticles without the stabilizing ligands, needed for the realization of their high sensitivity to the refractive index of the surrounding medium, were fabricated by laser ablation of a silver target in water. The narrow size and shape distribution of the obtained nanoparticle suspension enables to confidently observe the red-shift of the plasmon absorption band due to the influence of a protein shell (bovine serum albumin) formed around the nanoparticles.

1 Scientific background

1.1 Localized surface plasmon resonance (LSPR) in metal nanoparticles

Investigations related to the interaction of light with objects, whose dimensions are much smaller than the wavelength of the incident radiation, are still the subject of great interest. Particularly, nanoplasmonics is a fast-growing field of science that actively studies metal nanoparticles experiencing the plasmonic resonance [8]. This phenomenon occurs due to the oscillations of free conduction electrons in small metal nanoparticles under incident electromagnetic radiation. Such oscillations correspond to localized surface plasmons that form the background for sensing applications of nanoplasmonics [8, 9]. The large electric field enhancement provides a more intense light-matter interaction, which can be useful in various applications, such as surface-enhanced fluorescence (SEF) [10], surface-enhanced Raman scattering (SERS) [11], or metal-enhanced-chemiluminescence (MEC)[12]. The properties of nanoparticles largely depend on the material and the synthesis method. Among widespread methods, two types can be distinguished: *top-down* and *bottom-up*, a detailed description of each will be given below.

Optical properties of metal nanoparticles can be understood using a theoretical model: a gas of free electrons with a certain material-dependent density N moves relative to rigidly fixed ion core. In general, the equation of motion of a single electron from a plasmon layer induced by the external electric field $\mathbf{E}$ is defined as:

$$m\ddot{\mathbf{x}} + m\gamma\dot{\mathbf{x}} = -e\mathbf{E} \tag{1.1}$$

where m is the effective electron mass; e is the electron charge; γ is the frequency of electron collisions. If the time dependence of the electric field is assumed $\mathbf{E}(t) = \mathbf{E}_0 e^{-i\omega t}$, then the solution for the equation of motion of an electron is of the form $\mathrm{x}(t) = \mathrm{x}_0 e^{-i\omega t}$. The complex

amplitude x_0 of the electron oscillations also accounts for the phase shift relative to electric field oscillations. The amplitude is expressed in the following form:

$$x_0(t) = \frac{e}{m\left(\omega^2 + i\gamma\omega\right)}\mathbf{E_0}(t) \tag{1.2}$$

Hence, the electron shift causes the polarization $\mathbf{P} = -Ne\mathbf{x}$ with the complex amplitude:

$$\mathbf{P_0} = -\frac{Ne^2}{m(\omega^2 + i\gamma\omega)}\mathbf{E_0}, \tag{1.3}$$

Given that the linear susceptibility χ of the metal is related to the equation $\mathbf{P_0} = \chi\mathbf{E_0}$, then from 1.3 one can deduce

$$\chi = -\frac{Ne^2}{m\left(\omega^2 + i\gamma\omega\right)}. \tag{1.4}$$

The optical properties of metals are primarily determined by the behavior of free carriers (electrons) in the metal. The dielectric permittivity can be obtained from the electron response on the incident electromagnetic field. Thus, the model of the free carriers is derived from the equation of motion of an electron, taking into account the collisions with motionless ions as damping.

In this model, commonly known as the Drude model [1], the expression for the dielectric permittivity of metal reads as:

$$\varepsilon(\omega) = 1 - \frac{\omega_p^2}{\omega^2 + i\gamma\omega}, \tag{1.5}$$

where $\omega_p^2 = \frac{4\pi Ne^2}{m}$ is the plasma frequency of free electron oscillation. The complex dielectric permittivity can be written as the sum its real and imaginary parts, $\varepsilon(\omega) = \varepsilon'(\omega) + i\varepsilon''(\omega)$. Using this and Eq. (1.5), one can obtain

$$\begin{aligned}\varepsilon'(\omega) &= 1 - \frac{\omega_p^2\tau^2}{1 + \omega^2\tau^2}\\ \varepsilon''(\omega) &= \frac{\omega_p^2\tau}{\omega\left(1 + \omega^2\tau^2\right)}\end{aligned} \tag{1.6}$$

Under the conditions $\gamma << \omega < \omega_p$ ($\tau >> 1/\omega$), the dielectric permittivity is mainly real (in this case, the absorption is insignificant) and Equation 1.6 reduces to

$$\varepsilon'(\omega) = 1 - \frac{\omega_p^2}{\omega^2}. \tag{1.7}$$

When $\omega < \omega_p$, the real part of the dielectric permittivity is negative, and metal becomes highly reflective. In the high-frequency range, $\omega \geqslant \omega_p$, the free electrons in the metal nanoparticles have no time to follow the fast oscillations of the external field, and the dielectric

permittivity becomes positive. The Drude model accurately describes many optical properties of simple metal nanoparticles. However, it is also necessary to take into account the interband transitions that occur in the optical range resulting in additional losses in the response of the material. Therefore, the introduction of an additional term ε_∞ is required

$$\varepsilon(\omega) = \varepsilon_\infty - \frac{\omega_p^2}{\omega^2 + i\gamma\omega} \tag{1.8}$$

The free electron model is applicable only for the low-frequency region, which is clearly seen when comparing with the experimental data (shown for gold in Figure 1.1) obtained by Johnson and Christy [3]. As can be seen from Figure 1.1, in the high-frequency region, the free-electron model does not consider the region corresponding to interband transitions in metal.
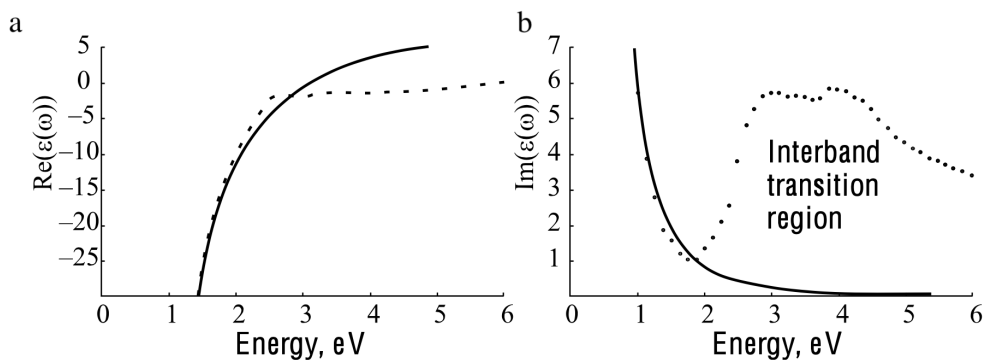
Figure 1.1: (a) The real and **(b)** imaginary parts of dielectric permittivity of gold are in the Vis-NIR range. The solid curve corresponds to the free electron approximation and the dashed curve to the experimental values obtained in Ref. [3]

1.2 Methods for calculating the absorption and scattering spectra of light by small particles of arbitrary shape

1.2.1 Analytical method

A special case in **plasmonics** is the study of the excitation process of plasmons in metal nanoparticles whose diameter is less than the wavelength of the incident light. Plasmons can be represented as quanta of collective oscillation of electrons, similar to oscillations of a harmonic oscillator, with respect to positively charged cores, as shown in Figure 1.2.
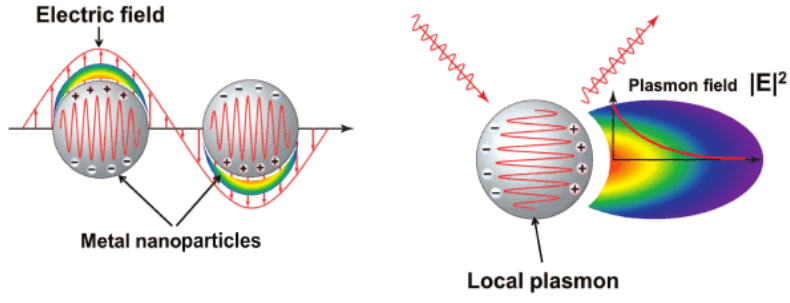
Figure 1.2: Schematic illustration of a localized surface plasmon resonance [4]

First, consider the case of the quasistatic approximation. It can be applied if the nanoparticle size is much smaller than the wavelength of incident radiation. Under this approximation, free electrons are not connected with the ionic core of the crystal lattice and can coherently move under the influence of the applied electromagnetic field. This leads to the fact that polarization charges appear on the surface of the metal nanoparticle, which acts only as a restoring force (Figure 1.2, resulting in the appearance of localized plasmon resonance with a certain frequency. In contrast to plasmons in extended structures (e.g. thin metal film), such oscillations do not propagate, therefore their resonant excitation is called *localized surface plasmon resonance* (LSPR). The spectral position of the localized plasmon resonance depends on several aspects which will be described below. The most common materials used in plasmonics are gold, silver, copper, and aluminum[2].

The optical properties such as the absorption and scattering of light by small spherical metal particles were theoretically described in the works of Maxwell-Garnett in 1906 [13] and Gustav Mie in 1908 [14]. Solving Maxwell's equations for electromagnetic radiation interacting with a spherical metal particle of arbitrary size gives a series of multipole oscillations (dipole, quadrupole, etc) in the absorption and scattering cross-sections of particles depending on the particle size. In the case when the particle is much smaller than the wavelength, its scattering cross-section reduces to the Rayleigh approximation [15]. If an external electromagnetic wave polarizes a particle, then the variable dipole of plasmon oscillations may be expressed through the polarizability:

$$\alpha = 4\pi a^3 \frac{\varepsilon - \varepsilon_b}{\varepsilon + 2\varepsilon_b}, \qquad (1.9)$$

where ε and ε_b are the dielectric permittivity of the nanoparticles and the medium, respectively, a is the radius of the nanoparticle. As follows from Equation 1.9 for polarizability of a spherical nanoparticle, the condition for plasmon resonance is $\mathrm{Re}\left[\varepsilon(\omega)\right] \approx -2\varepsilon_b$. In turn, the scattering and extinction cross-sections of a nanoparticle in the dipole quasistatic approximation are

related to its polarizability α by the following expressions [2]:

$$\sigma_{scat} = \frac{k^4}{6\pi}|\alpha|^2 = \frac{8\pi}{3}k^4 a^6 \left[\frac{\varepsilon(\omega) - \varepsilon_d}{\varepsilon(\omega) + 2\varepsilon_b}\right]^2$$
$$\sigma_{ext} = k\,\mathrm{Im}[\alpha] = 4\pi k a^3\,\mathrm{Im}\left[\frac{\varepsilon(\omega) - \varepsilon_b}{\varepsilon(\omega) + 2\varepsilon_b}\right] \tag{1.10}$$

where $k = 2\pi/\lambda$. Consequently, the absorption cross-section of nanoparticle can be evaluated as:

$$\sigma_{abs} = \sigma_{ext} - \sigma_{sc} \tag{1.11}$$

Quasistatic approximation provides a convenient description of LSPR in nanoparticles of different shape and constitution. In particular, the concise formula may be obtained for prolate and oblate spheroids and for nanoparticles of a general ellipsoidal shape. The polarizability of a confocal ellipsoidal core-shell nanoparticle in a field parallel to one of its main axes can be calculated through the particle polarizability [2, 15]:

$$\alpha = \frac{v\left((\varepsilon_2 - \varepsilon_b)\left[\varepsilon_2 + (\varepsilon_1 - \varepsilon_2)\left(L^{(1)} - fL^{(2)}\right)\right] + f\varepsilon_2\left(\varepsilon_1 - \varepsilon_2\right)\right)}{\left(\left[\varepsilon_2 + (\varepsilon_1 - \varepsilon_2)\left(L^{(1)} - fL^{(2)}\right)\right]\left[\varepsilon_b + (\varepsilon_2 - \varepsilon_b)L^{(2)}\right] + fL^{(2)}\varepsilon_2\left(\varepsilon_1 - \varepsilon_2\right)\right)}, \tag{1.12}$$

where $L^{(i)}$ (i=1,2) are the geometric factors of the core and the shell in the direction of the polarization; ε_1, ε_2, ε_b are the frequency-dependent dielectric permittivity function of the nanoparticle core, the shell and background media, correspondingly; v is the full volume of the nanoparticle with the shell and f is the ratio of the inner core volume to v.

In the following works [2, 16, 17], the authors calculated plasmon resonances for arbitrary-shaped nanoparticles. In particular, an ellipsoidal nanoparticle was considered. Plasmon resonance dipole vibrations oriented along the long axis has a red-shift in the resonance wavelength, and along the short axis is a blue-shift. It was established that the contribution of changes in the intensity and position of the plasmon resonance of an ellipsoidal shape depends on the orientation of the polarization of the incident light wave relative to the axes of the ellipsoid. Table 1.1 summarizes the conditions of plasmon resonance for particles of various shapes with a depolarization factor L in a medium with a dielectric permittivity ε_b [15].

Table 1.1: Plasmon resonance conditions for particles with arbitrary shapes.
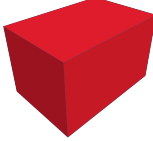
Shape				
	Bulk material	*Cylinder*	*Sphere*	*Ellipsoid*
Resonance condition	$\varepsilon_m = 0$	$(\parallel) \rightarrow \varepsilon_m = 0$ $(\perp) \rightarrow \varepsilon_m = -\varepsilon_b$	$\varepsilon_m = -2\varepsilon_b$	$\varepsilon_m = -\varepsilon_b \frac{1-L}{L}$
Resonance frequency	$\omega = \omega_p$	$\omega = \omega_p$ $\omega = \dfrac{\omega_p}{\sqrt{1+\varepsilon_b}}$	$\omega = \dfrac{\omega_p}{\sqrt{1+2\varepsilon_b}}$	$\omega = \dfrac{\omega_p}{\sqrt{1-(1-1/L)\varepsilon_b}}$

1.2.2 Numerical methods

The optical properties of metallic nanoparticles can be modeled with high accuracy using various rigorous numerical calculation methods, such as finite-difference time-domain method (FDTD), discrete dipole approximation (DDA), and finite element method (FEM) (comparative characteristics in Table 1.2). Furthermore, the use of the numerical methods makes it possible to solve the Maxwell equations for the complex structures (hybrid, multilayer, arbitrary shapes), where the quasi-static approximation or even the Mie theory cannot be applied. Special attention in the following chapters is given to the investigation of the influence of the shape, size, dielectric surrounding, and spatial arrangement on the metal nanoparticles properties using numerical calculation methods.

One of the most common methods for solving the electrodynamic problem is the *DDA* method. Purcell and Pennypacker initiated this method to explain light scattering by interstellar dust grains, which was then and ultimately improved by Draine et al. [18]. By taking the advantage of this method, optical scattering and light absorption for arbitrary shapes, representing an interacting array of dipoles with a certain polarizability tensor referred to individual nanoparticles, [19] can be calculated. The advantage of the DDA method is the ability to consider not only nanoparticles of arbitrary shape, but pairs of particles since there are no restrictions on the nodes of the cubic lattice.

FEM is an alternative state-of-the-art numerical method for solving a system of differential equations for boundary value problems. The main algorithm of FEM is that any continuous

value in a certain region can be approximated by a discrete model, which is created from a set of piecewise continuous functions defined in a finite number of subdomains (elements) presented in the form of tetrahedral or triangular prisms. Usually, such functions are polynomials - linear, quadratic, cubic, etc. The final result of each subdomain is then combined again to solve the problem.

The *FDTD* method is formulated based on the discretization of Maxwell's equations written in a differential space-time formulation, dividing the region into a grid of small cells called 'Yee' cells. The grids for the electric and magnetic fields are offset in relation to each other in time and space by half of the sampling step for each of the variables. Finite-difference equations make it possible to determine the electric and magnetic fields at a given moment of time based on the known values of the fields at a previous moment in time, and under given initial conditions; the computational procedure deploys the solution in time from the reference point with a given step. In addition to the simplicity of the formulation, the FDTD method, like FEM, has undoubted advantages in terms of modeling electrodynamic nanoscale objects with inhomogeneous, anisotropic, and nonlinear media with arbitrary boundary shapes [20]. A minor drawback of the FDTD method may be related to the accuracy and efficiency of the calculation with a large distance between the mesh cells. However, an increase in the density mesh avoids computational errors, despite the increase in the calculation time.

Table 1.2: Characteristics of various computational method for nanoscale objects.

Method	Type	Possible structure	Mesh type
Mie theory	Analytical	Spheres (core/shells)	Not used
DDA	Numerical (frequency domain)	Arbitary	Cubic
FEM	Numerical (frequency domain)	Arbitary	Triangular or tetrahedral
FDTD	Numerical (time domain)	Arbitary	Rectangular

1.3 Size, substrate, lighting-rod, and lattice effects

The localized plasmon resonance of metal nanoparticles is highly dependent on the size, shape, arrangement, environment of the nanoparticles, and also the material which the nanoparticle is made of [2]. Using nanoparticles with a specific LSPR position is an important condition for effective energy transfer between an organic molecule and plasmonic nanoparticle.

Due to the fact that many applications require the use of metal nanoparticles on a substrate, this inevitably leads to a violation of the symmetry of the dielectric environment, thereby changing the metallic properties. When collective vibrations are excited in a plasmon nanoparticle, image charges in the dielectric substrate can be induced. As a result, one can observe a strong interaction of plasmon oscillations with charge images. LSPR band of metal can be adjusted by changing the dielectric permittivity of the utilized substrate leading to blue-shift for small values and red-shift for large ones [21].

Another optical effect in nanoscale metal particles is a *lightning rod effect*. Under the shape modification of nanoparticles other than spherical, the external field changes its shape, and the lines of force are concentrated on the tip of the nanoparticle, leading to an increase in the electric field strength. This effect is practically independent on the frequency of the external field and is often used in hybrid nanoparticle/dye structures. The luminescent intensity of dye molecules located near the nanoparticles in the enhanced local field can be enhanced as well.

Within the framework of the quasistatic approximation, the local field enhancement for a spherical nanoparticle can be described by Equation 1.13, while for the ellipsoidal particle by Equation 1.14.

$$\left|\frac{E}{E_0}\right|^2 = \left|\frac{3\varepsilon_b}{\varepsilon + 2\varepsilon_b}\right|^2 \tag{1.13}$$

$$\left|\frac{E}{E_0}\right|^2 = \left|\frac{1}{1 + (\varepsilon/\varepsilon_b - 1)L}\right|^2 \tag{1.14}$$

The effect of *lattice plasmon coupling* between nanoparticles in arrays plays a prominent role. The interaction of metal nanoparticles in an array leads to collective plasmon resonance by means of multiple scattering of radiation, which is not possible for an isolated nanoparticle. To calculate the optical properties of periodically arranged nanoparticles on a substrate, one needs take into account the factor S, which is responsible for the contribution of the sum of the scattered fields created by other particles in the array:

$$S = \frac{1}{4\pi\varepsilon_0} \sum_j \exp\left(ikr_j\right) \left[\frac{(1 - ikr_j)\left(3\cos^2\theta_j - 1\right)}{r_j^3} + \frac{k^2\sin^2\theta_j}{r_j}\right], \tag{1.15}$$

where $\varepsilon_0 \approx 8.854 \times 10^{-12}$F/m, r_j determines the distance between nanoparticles, θ_j is the angle between the x-axis and the radius-vector of the nanoparticle with the number j.

Hence, the effective polarizability should be rewritten taking into account the polarizability for the isolated nanoparticle from Equation 1.9:

$$\alpha^* = \frac{1}{1/\alpha - \varepsilon_0 S} \tag{1.16}$$

The nature of the appearance of lattice plasmon resonance is due to the fact that the polarization in the array becomes large, in particular when the real parts of $\frac{1}{\alpha}$ and S are equal. The study of a periodic array of metal nanoparticles, experiencing collective lattice plasmon resonances, was done in the following work [22], where Humphrey *et al.* discussed the lattice plasmon resonances near the diffraction edge of the array. If the real part of the denominator in Equation 1.16 goes to zero, then it results in a strong peak (blue curve) in Figure 1.3a.
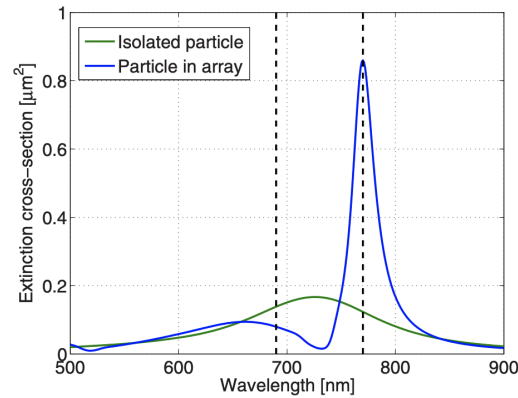
(a) Calculated extinction cross-section per particle
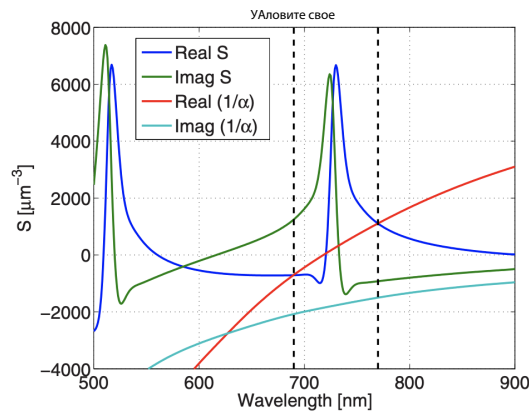
(b) 1/α and S

Figure 1.3: Appearance of lattice plasmon resonance. **(a)** The computed extinction cross-section for the isolated silver nanodisk and silver nanodisk in array, **(b)** appropriate computed array S factor (real and imaginary part) [5].

If the real part of the denominator in Equation 1.16 goes to zero, a strong peak (blue curve) appears in the spectrum, as shown in Figure 1.3a. A more visual manifestation of the lattice plasmon resonance due to diffraction is seen in Figure 1.3b where the intersection occurs between Re[S] and Re[$\frac{1}{\alpha}$] at 727 nm.

1.4 Fabrication methods of plasmonic nanoparticles

The synthesis of nanoparticles and nanostructures is divided into two types: 1) *top-down*, realized on the basis of the lithographic methods or pulsed laser ablation (PLA) [23], and 2) *bottom-up*, where the synthesis method can be represented by chemical growth of nuclei, subsequently stabilized by a ligand layer or by the method of self-organizing nanoparticles on a substrate, for example, physical vapor deposition (PVD).

As mentioned above, lithography refers to the top-down method. Among the relatively practical methods, electron beam lithography (EBL) should be considered. The technological process is almost similar to photolithography but there is no photomask. EBL technique involves electron beam exposure for the treatment of the photoresist layer, which changes its properties under the influence of accelerated charged particles. An electron microscope is used to pattern the necessary nanostructures at a specific dose of energy. Once the metal layer is sprayed over the photoresist, after subsequent lift-off of the photoresist, only ensembles of nanoparticles retain on the surface.

One of the simplest methods is PLA [24]. The principle of the method is to remove the matter from the surface using a laser pulse. Pulse laser ablation was developed in the 1960s, shortly after the advent of the ruby laser pulse principle. Since then, in many numerical experiments, laser ablation has been performed in gas, liquid media, a rarefied medium, and in a vacuum. Among the attractive features there is a relatively simple experimental technique, absence of mechanical contact during the synthesis, ability to obtain stable nanoparticles free from the stabilizer for a long time, and use of various solvents. Such benefits are useful for very promising practical applications as catalysis research [25], electronics [26, 27], nonlinear optics [28], biomedicine [29], SERS [11, 30], and SEF [10, 31] application.

The main features of laser ablation are as follows:

1. Laser ablation is associated with direct absorption of laser pulse energy in a substance

2. The result of laser ablation is the formation of a plasma cloud

3. Laser ablation occurs at the interface between the condensed and gas (or vacuum) or liquid phases

4. Laser ablation is of a threshold nature

5. When there are liquids, it is likely the synthesized particles participate in the secondary interaction with the laser beam. In this case, the nanoparticles are heated and coagulate with each other under prolonged exposure to a pulsed laser.

The experimental work in [32] describes the possibility to obtain small silver nanoparticles with sizes ranging from 4.34 to 4.9 nm using the PLA method. They utilized polymer coating polyvinylpyrrolidone (PVP), poly(vinyl-alcohol) (PVA), which provides good control over particle size distribution. Another interesting work [33] is devoted to tuning plasmon properties of chemicals-free silver nanoparticles by PLA in various organic liquids. Besides, the silver nanoparticles were functionalized in the same solvent as the original liquid. The procedure is simple and involves the adding stabilizer molecules to the colloidal solution. As a result, this led to a red-shift of the absorption band of silver nanoparticles due to changes in the surrounding dielectric permittivity. The next work proposed a reliable and well-controlled method for gold and silver nanoparticles fabrication realized by the use of a continuous wave laser [34]. The variation of laser intensity and effective irradiation time strongly influences on the average diameter of synthesized nanoparticles according to the transmission electron microscope images.

Chemical synthesis based on the surfactants and stabilizing ligands allows to obtain nanoparticles of various shapes and sizes (nanospheres, nanorods, nanotriangles, nanocubes, etc.) with the advantage of controlling the size, adjusting plasmon resonance bands and a favorable shape with enhanced near-field. The formation of nanoparticles by the chemical method involves adding a precursor such as chloroauric acid $HAuCl_4$ for gold nanoparticles or metal precursor $AgNO_3$ for silver nanoparticles with a reducing agent. It is worth noting, the growth rate plays a crucial role and determines the size of the nanoparticles as shown in [35].

Another way among the most promising and fairly common methods for creating nanoparticles is their thermal deposition in specific high-vacuum equipment, also called PVD (physical vapor deposition) technique. PVD provides increased purity, a high degree of adhesion to the substrate, and structural uniformity.

1.5   Principles of chemiluminescence spectroscopy

Chemiluminescence, or "liquid light" effect, is an emission of photons resulting from an exothermic reaction [36]. This fascinating optical effect finds its use in various applications

from forensic science targeted to detection the blood traces at crime scene [37], to industrial bio-chemistry [38, 39]. One of the vivid examples of a chemiluminophore is luminol, which generates blue light under certain conditions [40]. Forensic investigators use luminol to detect trace amounts of blood at crime scenes since it reacts with the iron in hemoglobin; biologists use it in cellular assays to detect copper, iron, and specific proteins [41]. However, the intensity of chemiluminescence of many chemiluminophore molecules is very low, which significantly limits its potential applications. One of the efficient experimental tools for observing the chemiluminescence effect is a microfluidic chip. Such chips are employed to study low volume samples by isolating key phenomena from the influential surrounding environment [42]. The flow-injection in microfluidic chips helps in obtaining the efficient chemical reaction when the chemiluminophores and their oxidants are mixed to emit light. Crucial developments for the fabrication approaches in the field of microfluidic technology platforms have already created high-demanded applications such as the lung-on-a-chip platform [43–45], single-cell functional proteomics [46, 47]. Moreover, these developments allow measuring the dynamics of green fluorescence protein [48, 49]. However, the efficient enhancement of poor quantum emitters, such as the chemiluminophore luminol, has never been proposed. This efficient emission of luminol is expected to find applications in forensic science-on-a-chip, and accurate DNA profiling.

1.5.1   Mechanism of metal-enhanced chemiluminescence

As it was previously reported [50, 51], in contrast to the metal-enhanced fluorescence (MEF)[52, 53], where the molecule must be initially pumped by external light, metal-enhancement chemiluminescence (MEC) origins stems from a chemical oxidation process, as shown in the Jablonski diagram in Figure 1.4(c). It is important to note that the quantum efficiency of the chemiluminescence process is quite low due to the competition with a multitude of non-radiative decay processes [54]. Hence, radiative decay acceleration of the chemiluminophore excited state is a reliable way to enhance the chemiluminescence yield, and this is a possibility that attracts the attention of many scientists [36, 55, 56]. The surface plasmon resonance in metallic nanoparticles [57, 58] can be employed for the acceleration of these radiative transitions. Figure 1.4 summarizes the schematics of the chemiluminescence enhancement mechanism.
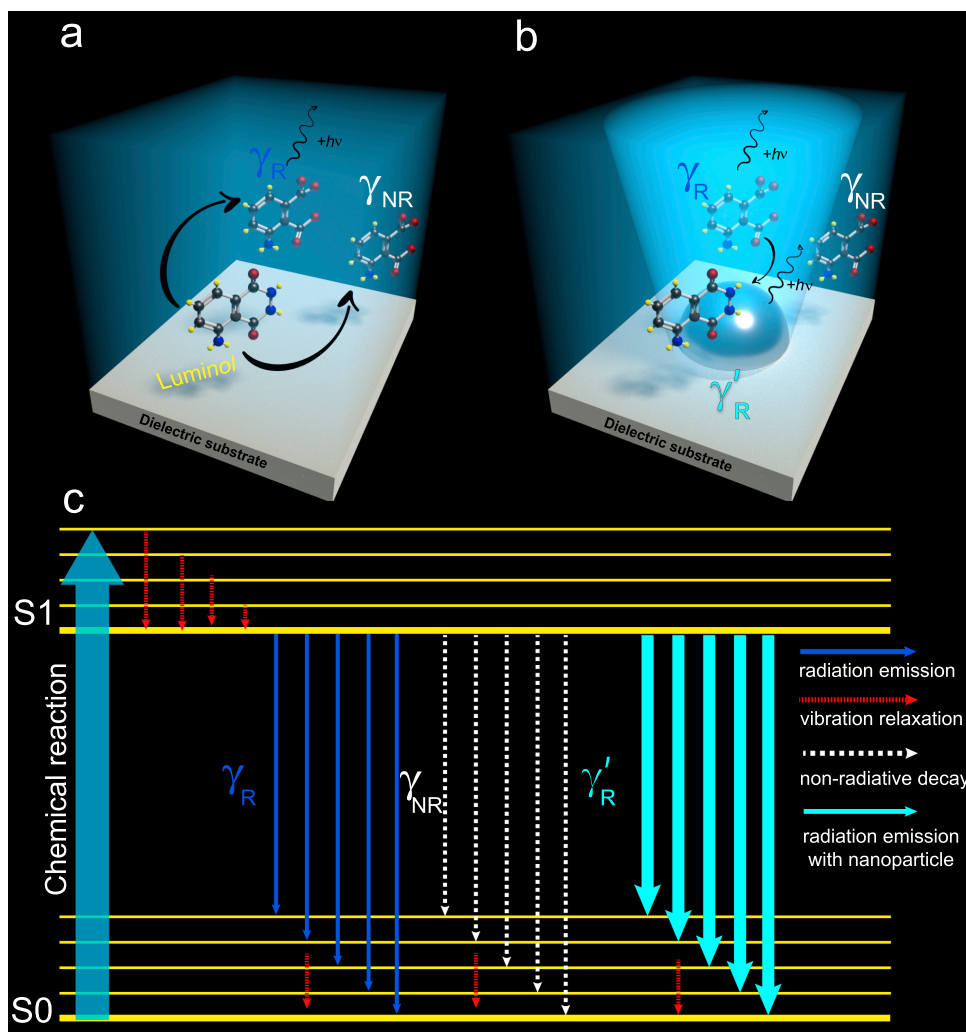
Figure 1.4: Schematics of the enhancement mechanism of the chemiluminescence effect. **(a)** The luminol oxidation leads to competitive processes of radiative decay (emission of a photon) and non-radiative decay (production of heat). The blue color emission is attributed to the emission of luminol. **(b)** The mechanism of the metal-enhanced chemiluminescence in the presence of SNP. **(c)** The general Jablonski energy level diagram modified for the chemiluminescence emission in the presence of SNP [6]. The chemiluminescence emission origin as a result of the chemical oxidation process. The molecular transition from the excited (*S1*) to the electron ground state (*S0*) leads to the photon emission and production of heat. γ_R and γ_{NR} are the radiative and non-radiative decay rates of the luminol molecules. γ'_R is the radiative decay rate of luminol molecules in the vicinity of SNP.

Figure 1.4a represents the luminol excitation in the course of a chemical reaction with an oxidizer followed by two competitive decay routes: radiative and non-radiative. The effect of silver nanoparticles (SNP) on the luminol emission is depicted in Figure 1.4b. The expected chemiluminescence enhancement is due to the Purcell effect that couples the luminol emission with the enhanced local fields in the vicinity of SNP [51]. As a result, the density of photon

states increases, and the process of chemiluminescence is boosted. This effect reaches its maximum in close proximity of the nanoparticles and vanishes at larger distances. At the same time, direct contact with the metal surface is known to lead to the luminescence quenching. Since the luminescence quantum yield (η) is determined by the competition of radiative (γ_R) and non-radiative (γ_{NR}) decay processes, then for the case when γ_{NR} is larger or the same order of magnitude as γ_R growth of γ_R, it leads to the substantial growth of the luminescence quantum yield provided the growth of γ_{NR} is smaller than the growth of γ_R. Therefore, the chemiluminescence quantum yield in the presence of metal nanoparticles grows according to the formula $\eta \propto \frac{\gamma'_R}{\gamma'_R + \gamma'_{NR}}$, where γ'_R and γ'_{NR} are the modified radiative and non-radiative decays with the presence of metal nanoparticles. Thus, the chemiluminescence intensity can be increased by plasmon nanoparticles provided the condition of the increased radiative decay rate ($\gamma'_R > \gamma_R$) is fulfilled while γ_{NR} does not substantially grow.

To maximize the chemiluminophores-nanoparticles pair interaction, metal nanoparticles have to be placed at an optimum distance from the chemiluminophores [59]. The shape and material of the particles have to be accurately chosen to ensure the overlapping of their absorption plasmonic band with the emission band of the chemiluminophores[60]. Several studies were performed to investigate the use of plasmons for enhancing the radiative decay in a microfluidic chip [36]. However, those researchers did not use the non-resonant nanoparticles. There was a new proof-of-concept experiment conducted with a microfluidic chip [36], wherein the commercially available nanoparticles with the non-optimized spectral location of the plasmon absorption band were utilized. Therefore, chemiluminescence yield can be further improved with specially designed surfaces. As a result, two conditions are to be satisfied for the effective interaction between the plasmonic nanoparticle and the chemiluminophore: 1) the plasmon band has to overlap with the chemiluminescence emission band [36, 60, 61] and 2) the chemiluminophore molecules need to be in the close proximity with metal nanoparticles (not larger than the decay length of plasmon near-field) [36, 62]. According to [39], both the purely chemical catalytic effect of the contact with the metal surface and the Purcell electromagnetic effect contribute to the MEC activity. Nevertheless, the relative role the two effects play in the observed enhancement is not clearly determined.

1.6 Principles of overtone stretching modes for near-infrared spectroscopy

Near-infrared (NIR) spectroscopy is one of the spectroscopy fields that studies the absorption, reflection, and transmission spectra of molecules whose vibrational transitions have higher energy than their fundamental vibrations in the middle region of the infrared spectrum. The NIR region includes the wavelength range from 750 nm to 2500 nm, or in other words, wavenumbers 4000 - 13333 cm^{-1}. The first mention of infrared radiation referred to the experiments of William Herschel in the 1800 year. The most prominent signatures in this area are related to C-H stretching vibrations of methyl, methylene, aromatic functional groups, and OH-stretching vibrations. Molecular signatures of the following groups are less common: methoxy-C-H stretching, carbonyl-associated C-H stretching; N-H from primary amides, secondary amides (both alkyl and aryl groups), N-H from primary, secondary and tertiary amines and N-H from amine salts. This list also includes combination modes, which are also located in the NIR range, provided that two or more fundamental vibrations are excited simultaneously. The main drawback of such overtone vibrations is their relatively weak absorption intensity, usually approximately 10-100 times weaker than fundamental vibrational modes. To explain the principles, let us consider the vibrations of a diatomic molecule so that the atoms oscillate in a simple harmonic potential. The vibrational movement of molecules consists of a periodic change in the relative arrangement of nuclei. In this case, one can assume that the vibration frequency of a diatomic molecule is expressed as follows:

$$\nu = \frac{1}{2\pi}\sqrt{\frac{k}{\mu}},$$
(1.17)

where μ, k are the effective mass and the force constant. According to quantum mechanics, the absorption of electromagnetic radiation in NIR by a molecule is explained as a vibration transition between different energy states of a molecule due to the interaction with an external electromagnetic field. The vibrational energies of molecules can take only discrete values as can be seen from equation:

$$E(n) = \left(n + \frac{1}{2}\right)h\nu,$$
(1.18)

where n is a quantum number that takes only integer values.

In Figure 1.5, the harmonic oscillator is determined by the parabolic potential curve. This means that the elastic force and potential energy increase with increasing distance from the equilibrium position x_E.
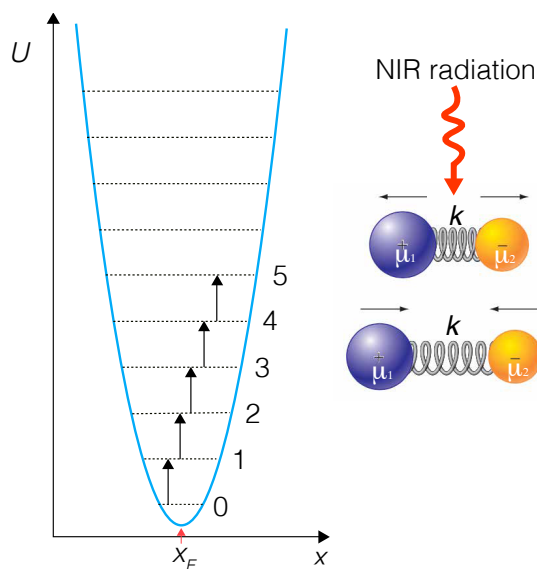
Figure 1.5: Potential energy, energy levels and allowed transitions in the the harmonic oscillator.

On the one hand, within the dipole approximation the vibrational transitions cannot occur between any two levels. According to the selection rules, the vibrational transitions are possible when the condition of $\Delta n = \pm 1$ is satisfied (the variation in the vibrational quantum number is equal to one) [63]. Particularly, the selection that governs the cases when a given matrix element is not equal to zero (the dipole transition is not forbidden, or allowed). The derivation of the selection rules for transitions of various types is reduced to the calculation (or evaluation based on symmetry) of the corresponding matrix elements. In this respect, the vibrational levels are distributed equidistantly (see Figure 1.5, that is, the transition energy between neighboring levels is the same. For example, the spectrum of a diatomic molecule has a single absorption line.

On the other hand, the shape of the potential curve of a molecule with increasing the distance between the centers of atoms deviates from a parabola. Figure 1.6 demonstrates the behavior of the potential energy curve of a diatomic molecule. In this case, the potential energy can be represented through the analytical equation of the Morse potential

$$V(Q) = D_e \left[1 - e^{-\alpha(Q-Q_e)} \right]^2,$$ (1.19)

where $\alpha = \sqrt{k/(2D_e)}$
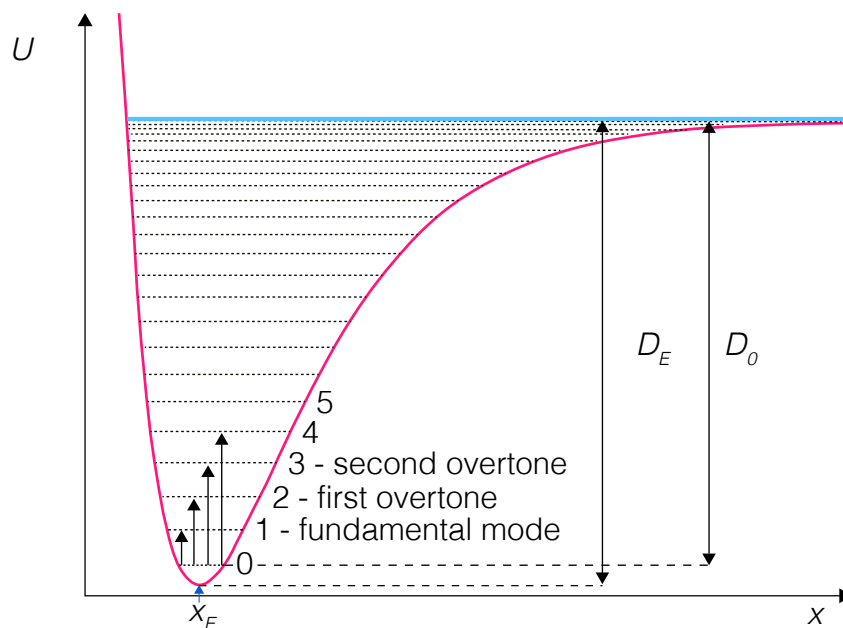
Figure 1.6: Potential energy, energy levels and allowed transitions from the ground state to high-order states in the anharmonic oscillator. D_e and D_0 are the well depth of potential energy curve and dissociation energy, respectively.

As a result, the oscillation frequency, bandwidth, and intensity can be more accurately described within the framework of the anharmonic oscillator approximation. Consequently, the vibrational transitions, for instance, 0→2 and 0→3 are allowed. One can note, that the intensity of absorption band depends on the probability of transition from the initial state to a higher energy state and the molecular dipole moment. The absorption intensity of 0→2 vibrational transition is weaker than 0→1 transition transition.

A much more accurate expression for the vibrational energy of the anharmonic oscillator is now given as follows:

$$E(n) = \left(n + \frac{1}{2}\right) h\nu - \frac{(h\nu)^2}{4D_e} \left(n + \frac{1}{2}\right)^2 \tag{1.20}$$

In this regard, the vibrational spectrum of the anharmonic oscillator, in contrast to the harmonic spectrum, contains a number of bands with frequencies ν_1, ν_2, ν_3 , etc. The absorption band with the frequency $\nu_1 = \nu_0$ (1 - 2X) is called fundamental (transition between vibrational levels with $n = 0$ and $n = 1$), a band with a frequency $\nu_2 = 2\nu_0$ (1 - 3X) is called the first overtone (transition between levels with $n = 0$ and $n = 2$); then the second overtone $\nu_3 = 3\nu_0$ (1 - 4X) comes, whereas $X = \frac{h\nu_0}{4D_0}$.

1.6.1 Surface Near-Infrared Absorption Spectroscopy

Surface Near-Infrared Absorption Spectroscopy (SENIRA) is a fast-growing practical analytical technique that allows to detect a weak molecular overtone vibration in the NIR region due to the amplified electromagnetic field in plasmon nanoparticles (nanoantennas). In particular, in order to achieve effective amplification, the molecular sample should be placed in close proximity where the field of the plasmon nanoparticle is much stronger than the incident field. Among the possible ways to facilitate a better SENIRA signal are:

- use of plasmon nanoparticles with a certain aspect ratio (or size), so that the plasmon resonance band is in the NIR region

- the plasmon band and overtone is overlapped (spectrally tuned to the molecular vibrations)

- use of elongated nanoparticles which provide a lightning-rod effect with electric field enhancement at sharp ends

- placing analyte within an intense electromagnetic field in "hot spots" between a pair of nanoparticles or an ensemble
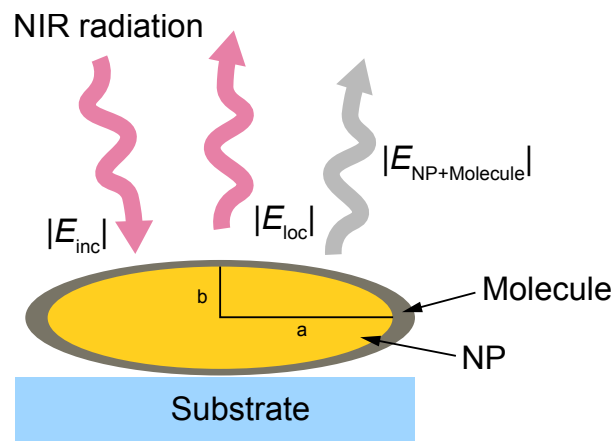
Figure 1.7: Schematics of the mechanisms of SENIRA activity.

Consider a simple model of an elongated ellipsoid surrounded by a thin layer of analyte (Figure 1.7), where the aspect ratio is defined as $AR = a/b$ (a is the half-axis along the length of the axis, b is the half-axis along only a short axis). Assume that a layer of a molecule with a dielectric permittivity ε_{mol} covers the metal nanoparticle uniformly. Under normal incidence

of light with polarization along the axis of the nanoparticle, a dipole plasmon resonance is excited, accompanied by an amplified electric near-field. It is worth noting,the amplified electric near-field around the nanoparticles is much larger and inhomogeneous compared with the incident one. If one can consider elongated nanoparticles, then the greatest enhancement takes place with a small radius of curvature, for example, in rod-like nanoparticles. The overtone amplification mechanism can be described as follows. External electromagnetic radiation induces a dipole moment in the nanoparticle, then multiple scattering processes occur between the nanoparticles and analyte molecules, and the signal can subsequently be detected in a far-field. As a result, the absorption intensity is proportional to the contributions of the scattered radiation from the antenna itself and the re-emitted signal from the analyte molecule.

Thus, the interaction of molecular overtones and metal nanoparticles, supporting plasmon vibrations in the NIR region, allows to demonstrate a significant increase in the intensity of the vibration signal.

1.7 Cellular uptake of nanoparticle in course of endocytosis

Due to the unique optical properties, nanoparticles have found applications in various therapeutic and diagnostic techniques, in biomedicine, namely, contrast-enhanced medical imaging, photothermal cancer therapy using metal nanoparticles, and targeted delivery of biomolecules and their release by heating. However, the lack of a clear understanding of the uptake mechanisms of nanoparticles into cell media and their interaction with biological media still requires more detailed studies. As the nanoparticle approaches the cell membrane, it interacts with a plasma membrane consisting of a double lipid layer. Further in the process of endocytosis, membrane enveloping occurs leading to the appearance of individual vesicles with nanoparticles. There are five different mechanisms of endocytosis, which depend on the type of cell (proteins, lipids, and other molecules): phagocytosis clathrin-mediated endocytosis, caveolin-mediated endocytosis, clathrin / caveolae-independent endocytosis, and macropinocytosis [7].

No less important challenge in this direction is to learn how the interaction of the biological medium and plasmon nanoparticles reveals in the optical response. It was previously mentioned
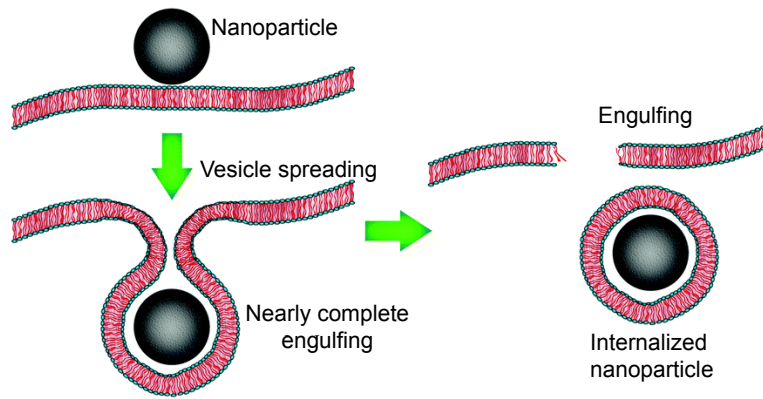
Figure 1.8: Schematic demonstration of the internalization of NP into the liposome as a results of endocytosis [7].

that the metal nanoparticles can be identified based on the optical response — absorption or scattering. A change in the dielectric permittivity of a medium can greatly alter the position of the LSPR band. In these articles [64, 65] it was shown that nanoparticles are absorbed during receptor-mediated endocytosis, and then a lipid bilayer surrounds the nanoparticles (as depicted in Figure 1.8, which subsequently tend to undergo agglomeration. A thorough study of the optical properties of metallic nanoparticles introduced into human breast adenocarcinoma Sk-Br-3 cells using hyperspectral visualization of a dark field has recently been conducted. It was noted that the spectrum of spherical nanoparticles with a length of 100 nm is significantly broadened and shifted to the red side by 78.6± 23.5 nm after 24 hours. To avoid agglomeration of nanoparticles, the thickness of the ligand layer can be increased, however, this will lead to a loss of sensitivity of plasmon resonance.

An analytical analysis and detailed numerical simulation of the transition of a silver nanosphere through a plane interface between two media showed [66, 67] that a plasmon resonance which is triple degenerate in a homogeneous medium, splits into two components with different frequencies when a spherical nanoparticle approaches the interface. As it approaches the dielectric interface, the splitting initially increases, then decreases, changes the sign, grows again, and finally disappears when the particle completely transfers to the second medium and moves away from the interface. It splits into a doubly degenerate mode of electron density oscillations along the interface and a non-degenerate mode of vibrations perpendicular to the boundary. More complex processes accompanying endocytosis, such as enveloping a particle with a cell membrane, also lead to noticeable changes in plasmon resonance; they have not been investigated yet and can be detected experimentally.

2 Materials and methods

2.1 Fabrication techniques for plasmonic nanoparticles

maybe some intro on typical fabrication techniques? or find one in your ch1 and move it here

2.1.1 Synthesis of colloidal silver nanoparticles (SNPs) in liquid using laser ablation technique

In this work, the silver nanoparticles (SNPs) using the laser ablation technique were synthesized. The experimental setup that was built is shown in Figure 2.1. A silver target with 99.99% purity to synthesize the nanoparticles was used. As a source for the laser ablation technique, was used a pulsed Nd: YAG solid-state laser (SOLAR Laser Systems), with pulse energy set to 100 mJ, and the pulse duration and repetition rate were set to 10 ns and 5 Hz respectively. The laser source enables the second harmonic generation with 532 nm and turned in the Q-switching regime during the ablation process.

Ablation was performed in cylindrical glass containers filled with distilled water with a volume of 3 ml. The laser beam with a diameter of 5 mm, using a spherical lens with a focal distance of F=60 mm, through transparent deionized water was focused on the surface of the silver target. The surface of the liquid remained free, and the layer above the surface of the target was several centimeters thick. To get SNPs with a broad size distribution the target for a certain time (see Section 5) were irradiated.
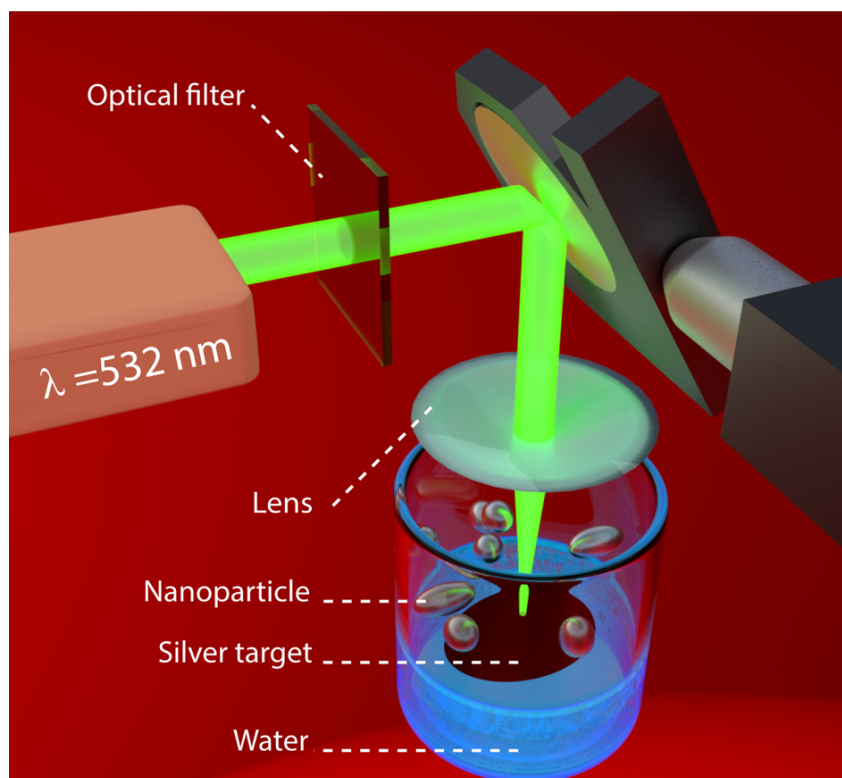
Figure 2.1: Illustration of the experimental set up of pulsed laser ablation of silver target in water. The dimensions are not to scale.

2.1.2 Synthesis of silver nanoparticles metasurface on dielectric substrate using physical vapor deposition

SNPs on the glass microscope slide were fabricated using physical vapor deposition (PVD) in a vacuum chamber PVD-75 (Kurt J. Lesker). SNPs ensemble were grown according to the Volmer-Weber mechanism [68]. The equivalent thickness of the SNP ensemble was 5 nm and controlled by a quartz crystal microbalance during the growth. The silver plate (99.99% purity) was evaporated in a high vacuum, then, the obtained silver film was annealed at 200 °C. The spectral position of the plasmon absorption band was controlled by the amount of the evaporated metal and the evaporation rate as well as by the temperature and the duration of the subsequent annealing according to the procedure in Ref. [69].

To provide a better adhesion of SNPs to the substrate and ensure their stability in the oxidizing environment in the course of the chemiluminescence studies, the laser-assisted approach was conducted. The laser exposure was realized by the third harmonic (355 nm) of a Q-switched Nd:YAG laser (SOLAR Laser Systems). The pulse duration and the repetition rate were 10 ns and 10 Hz, respectively. The laser beam, with a diameter of 8 mm, was focused on

the SNP ensemble supported on a glass substrate and scanned over the entire film. The pulse energy was controlled by filters and set to 20 mJ. Increase the adhesion of the SNPs to the substrate, the samples were irradiated with 100 laser pulses. The SNPs substrate covered with 2 nm SiO_2 layer was prepared to estimate the role of the catalysis effect from silver.

2.2   Samples characterization

2.2.1   Far-field measurement

Extinction spectra of the colloidal solution in a cuvette with a path length of 1 cm were collected using an SF-56 spectrophotometer (LOMO) with 1 nm resolution in the range of 250-800 nm at room temperature. The chemiluminescent spectra of Luminol were recorded with a charge-coupled device (CCD), Lumenera Infinity 2-3C (Lumenera Corporation, 7 Capella Crt. Ottawa, Ontario, Canada).

2.2.2   Microscope methods

The morphology studies of the sample with SNPs synthesized using pulsed laser ablation were performed using an atomic force scanning microscope (AFM) on Solver PRO-M (NT-MDT) system using silicon probes NSG01. Microscopic examination was performed in the tapping (semi-contact) mode. The resonance frequency and curvature radius of the probe in the tapping mode was 283 kHz and 10 nm, respectively. Scanning electron microscopy images of inspected SNP were obtained by MERLIN Carl Zeiss microscope at 15 kV.

2.3   Formation of silver nanoparticles/chemiluminophores complexes

A stock solution (denoted as *"solution 1"*) of 3-aminophthalhydrazide (luminol, Figure 2.2) with a concentration of $2.8 \cdot 10^{-5}$ M in deionized water, purchased from Sigma Aldrich, was mixed with sodium hydroxide (NaOH), which has the concentration of 1 mM. A 5% solution of sodium hypochlorite (NaOCl) was used as an oxidizing agent (next denoted as *"solution 2"*). Chemiluminescent radiation occurs as a result of a chemical reaction between organic chemiluminophore molecules and an oxidizing agent. In addition, an experiment with
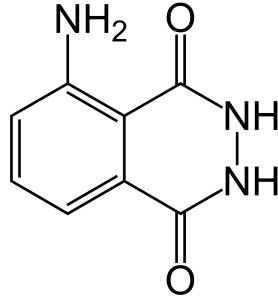
Figure 2.2: The chemical structure of 3-aminophthalhydrazide (luminol).

9,10-diphenylanthracene (DPA) was conducted. All chemiluminophore species were placed between two microscope glass slides, one of which is partially covered with SNPs embedded in advance.

2.4 Numerical modeling

pictures of your numerical models might be useful here

To calculate the absorption (ACS), scattering (SCS), and extinction (ECS) cross-section spectra of complex systems comprising gold nanoparticles and molecular shells in the framework of Chapter 4 (Section 4.2), 3D full-wave computational models implemented in the commercial software COMSOL Multiphysics 5.4 in the scattered field formulation was used. In particular, the wave optics module for electromagnetic waves in the frequency domain was utilized. The perfectly matched layer (PML) in the form of a physical domain was included to absorb all scattered light. The ACS (σ_{abs}) was calculated by integrating the power loss density over the particle volume, while the SCS (σ_{sc}) was derived by integrating the Poynting vector over an imaginary sphere around the particle, and the ECS is the sum of the ACS and SCS.

For Chapter 3, the total field formulation using a port configuration was used. The ACS, SCS, and ECS spectra of hemisphere SNPs varying its shapes and substrates to predict their behavior in combination with chemiluminophores have been calculated. A 3D box that contains two domains, with a width of 200 nm, was built for the dielectric substrate and surrounding media. The thickness of the perfectly matched layer (PML) is defined as half of the incident wavelength. The PML layer was divided by 8 equidistant layers. The silver hemisphere was placed in the center domain with subsequent meshing in the form of tetrahedral elements. The maximum elements size of the surrounding medium, dielectric substrate, and nanoparticle

were chosen as $\lambda/6$. The electromagnetic incident field oscillated parallel to the substrate with a k-vector perpendicular to the substrate.

The complex refractive index of the SNPs was obtained from the experimental work of Johnson and Christy[3]. The amendments to the optical constants of material associated with small particle sizes were not taken into account. Since the dephasing time of plasmon SNPs (for $r > 10$ nm) deposited on a dielectric substrate remained practically unchanged as shown in [70], the correction for intrinsic quantum size effect was neglected. The dispersion of BK7 used as a substrate was taken from Ref. [71].
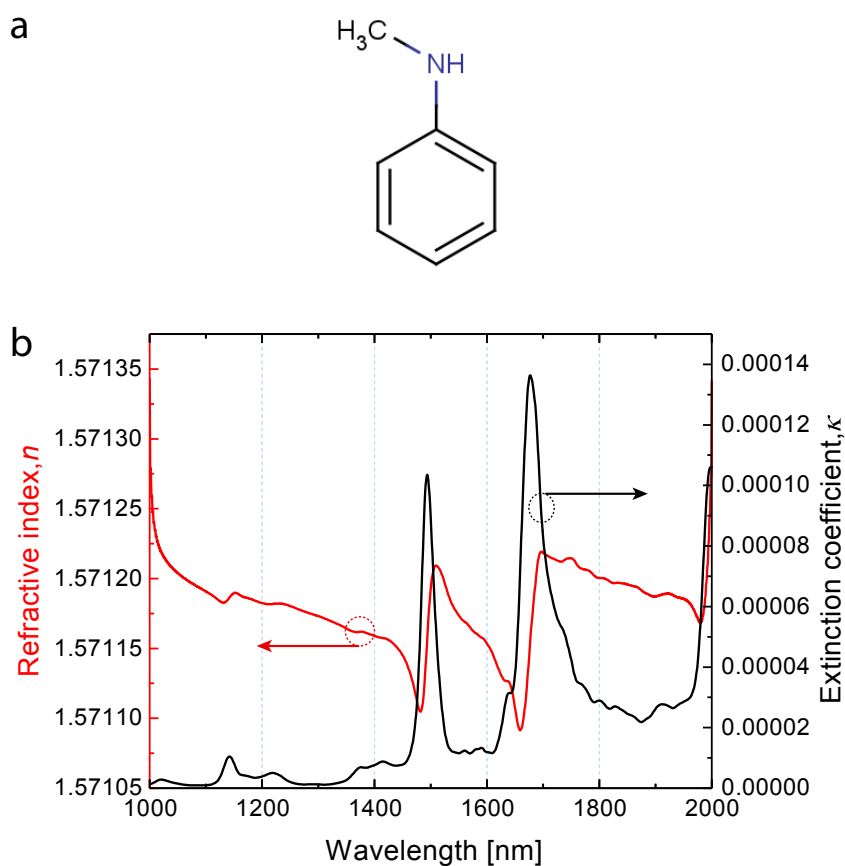
Figure 2.3: **(a)** The chemical structure of N-Methylaniline organic molecule and **(b)** dispersion characteristic of NMA molecules as a function of the wavelength in near-infrared region.

The N-Methylaniline (NMA) species (Figure 2.3) was chosen as a representative probe molecule example of an organic molecule that possesses overtone bands in the NIR spectral range [12, 72, 73]. The absorption bands at wavelengths of 1494 nm and 1676 nm are associated with the first overtones of N-H and C-H stretching modes. These bands are accompanied by the anomalous dispersion regions calculated based on a measured absorption spectrum as it follows from the Kramers-Kronig relations [72] as depicted in Figure 2.3.

To facilitate the comparison of the obtained theoretical results with the future experimental data, the notion of differential transmission (DT) was introduced which helps to single out the effect of the gold metasurface on the overtone absorption intensity. A transparent dielectric film characterized by a dispersionless purely real refractive index was employed as a reference for DT calculations. DT is computed as a difference between transmissions of analyte and immersion oil films of the same thickness. Transmission spectra of plane parallel films without gold nanoparticles were calculated analytically [74]. The refractive index of this film was chosen to be equal to the mean value of the NMA refractive index in the actual spectral range (n_{av} = 1.5712). Experimentally, such a film may be readily realized utilizing an appropriate immersion oil.

3 Metal-Enhanced Chemiluminescence effect

As was mentioned above in Chapter 1, it is important to note that the quantum efficiency of the chemiluminescence process is quite low due to the competition with a multitude of non-radiative decay processes [54]. Hence, the radiative decay acceleration of the chemiluminophore excited state is the reliable way to enhance the chemiluminescence yield and attracts the attention of many scientists [36, 55, 56]. The metal-enhanced chemiluminescence (MEC) phenomenon was firstly introduced in the experimental work [75, 76], where the authors used a silver island film to enhance the luminescence of chemiluminophore molecules. In this case, the transition to the excited state was conducted by the interaction of several standard chemiluminescence kits mixed with a hydrogen peroxide solution. In order to couple the chemiluminescent species with surface plasmons, molecules were deposited on the silver island film and then covered by two glasses on both sides in a sandwich-like form. Thus, the chemiluminescence intensity of luminophore placed in close proximity of the silver island film is significantly enhanced. The surface plasmon resonance in metallic nanoparticles [57, 58] also can be employed for the acceleration of these radiative transitions. In turn, the shape and material of the particles have to be accurately chosen to ensure the overlapping of their plasmonic bands with the emission bands of the chemiluminophores [60]. Several studies have been performed to investigate the use of surface plasmons for enhancing the radiative decay in microfluidic chips [51]; however, in those research works the non-resonant nanoparticles were used. For example, in proof-of-concept experiment [36] with a microfluidic chip the authors utilized the commercially available nanoparticles with the non-optimized spectral location of the plasmon absorption band. Therefore, chemiluminescence yield can be further improved with specially designed surfaces. Consequently, it seems feasible to fulfill the requirements for the effective acceleration of radiative transitions in luminol and other chemiluminescence

substances.

As regarding the synthesis of metallic nanoparticles, the most effective methods are thermal deposition of metal vapors on dielectric substrates in a vacuum and laser ablation of a metal target in liquids. However, a large variation in the shapes and sizes of nanoparticles obtained by self-organization leads to the inhomogeneous broadening of the extinction spectra. To modify the extinction spectra of metallic nanoparticles and reduce the width of their distribution in shapes and sizes, island metallic films can be thermally annealed. During this process, an increase in self-diffusion of metal atoms along the surface of the nanoparticles leads to the formation of more round particles with narrower distribution of plasmon resonance frequencies [69, 77].

In this chapter, the novel metal-enhanced chemiluminescence (MEC) sensor, which has significantly improved resistance to organic solvents and mechanical damage, is proposed. So far, in all attempts to enhance the weak chemiluminescence of luminol by plasmonic nanoparticles the enhancement mechanism was not clearly stated. According to [39], both the purely chemical catalytic effect of the contact with the metal surface and the Purcell electromagnetic effect contribute to the MEC activity. However, that relative role, which the two effects play in the enhancement observed, is not clearly determined. Table 3.1 represents a brief overview of the latest results related to the chemiluminescent enhancements of luminol as well as chemiluminescent species used in glow sticks [76, 78, 79]. The main peculiarity of luminol is bio-compatibility, which in turn allows its application for pharmaceuticals and biological sciences. Based on the recent work [36] using the colloidal solution of metal nanospheres with luminol flowing in a microfluidic chip, the switching from large consumable volumes of nanoparticles to small ones by using a planar metasurface of silver nanoparticles was realized. To the best of our knowledge, this is the first application of the plasmon metasurfaces fabricated on a dielectric substrate for luminol chemiluminescence enhancement. Our experimental results provide clear evidence that the catalytic action of silver is of minor importance compared to the Purcell effect. In this regard, the metal metasurface optimization, which allows for chemiluminescence intensity enhancement by means of the electromagnetic effects, is particularly important. Numerical modeling allows us to choose the experimentally realizable shape of metal nanoparticles that ensures perfect overlap between the plasmon bands of metal metasurface and chemiluminescent bands of chemiluminophores.

Table 3.1: An overview of Chemiluminescence sensors using different enhancement strategies.

Chemiluminescent system	Comments	Reference
Ag and Au with luminol-NaOH	The CL enhancement in microfluidic chip initiated by small sphere nanoparticles. The enhancement factor is up to 4-fold.	[36]
Ag-luminol-H_2O_2-HRP	A silver modified immunoassay for determination mycotoxins using luminol with amplified chemiluminescence on the chip through the surface plasmon resonance phenomenon. The enhancement factor is $\sim$ 2-fold.	[80]
Cr, Cu, Ni, and Zn metal films with green dye	The chemiluminescence intensity from chemiluminophore (commercially available kits, Omnioglow company - acridan oxalate system) was enhanced by metal films. The enhancement factor is up to 3-fold.	[78]
Al, Au, Ag metal films with red, green and blue dyes	The luminophores dyes excited the surface plasmons on thin continuous metal films without incident excitation light. The CL species/SPR coupling demonstrates a highly polarized and directional emission. The enhancement factor was not estimated.	[79]
Ag SIF with green dye-H_2O_2	The commercially available chemiluminophores from glowstick (commercially available kits, Omnioglow company) was enhanced by metal films. The enhanced chemiluminescence intensity is around 20-fold.	[76]

3.1 Numerical studies for SNP/luminol configuration

The Figure 3.1 shows the spectral overlap of the plasmon resonance bands of the truncated SNPs and the normalized emission spectrum of luminol. Firstly, let us consider (Figure 3.1, green curve) the main luminol chemiluminescence emission bands that appear at 452 nm and 489 nm, respectively. From the literature it is well-known, that the plasmon resonances of small silver and gold nanospheres in the aqueous environment have their maxima at the wavelengths of 415 nm and 528 nm respectively [36]. Hence, the most promising way to establish the desired resonance interaction is to choose silver as the material of the nanoparticles and change its 1) size, 2) shape, and 3) surrounding. These three ways may be employed to shift the localized surface plasmons in SNPs to longer wavelengths. Thus, the dedicated plasmonic-chemiluminophore system design that takes advantage of plasmonic nanoparticles tuning can lead to efficient enhancement of the chemiluminescence effect. By taking advantage of the fabrication of SNPs on dielectric substrates using PVD in ultrahigh vacuum, the long-wavelength shift of the plasmon bands of SNPs can be achieved either by direct contact of the metal nanoparticles with a substrate having a higher dielectric permittivity than water or the oblate shape of the nanoparticles obtained on the substrate surface during the deposition process. To explore if these two mechanisms may be well-balanced to provide the desired conditions for the plasmon band, the common transparent dielectric substrates were considered: glass, quartz (SiO_2), sapphire (Al_2O_3), magnesium fluoride (MgF_2), and titanium dioxide (TiO_2).

Figure 3.1 shows extinction, absorption, and scattering cross-sections spectra computed for nanoparticles supported on the glass substrate. The supported SNPs were assumed to be submerged in a luminol solution. Since luminol is expected to be diluted with a high ratio in water, the refractive index of the surrounded media was set to that of water, 1.33.
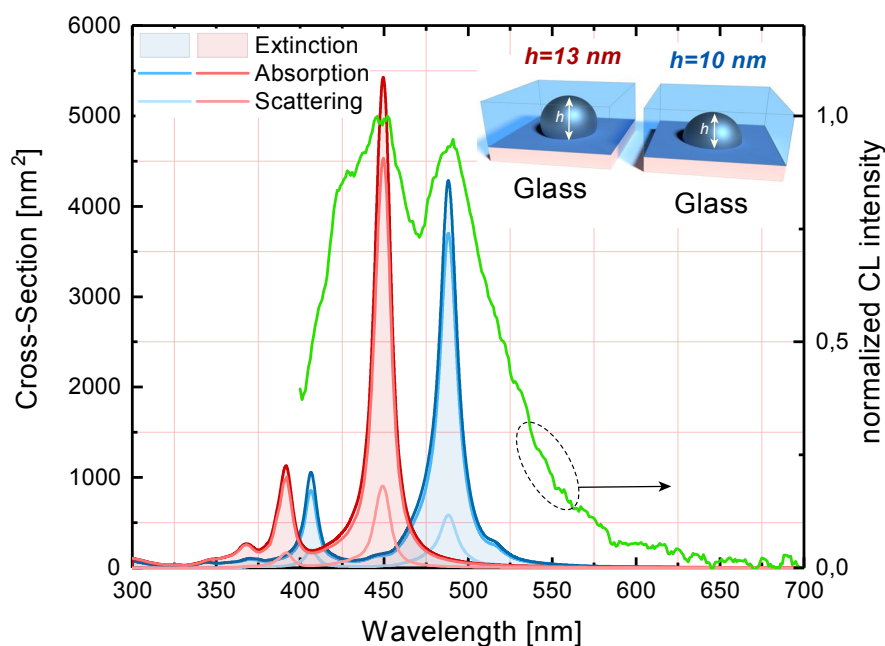
Figure 3.1: The overlap between the normalized chemiluminescence intensity spectra of the luminol solution (green line) and the calculated extinction spectra of SNPs supported on different substrates and submerged into the luminol solution. Extinction cross-section spectra of SNPs with h = 13 nm for the enhancement of luminol chemiluminescence emission band at 452 nm and with h = 10 nm for the luminol band at 489 nm. The diameters of SNPs in both cases are 20 nm. The 3D models of silver nanoparticles placed on the respective substrates and submerged into the luminol solution are illustrated in the inserts.

The shape of nanoparticles obtained by PVD was assumed to be a hemisphere while their diameter was continuously changed to match the absorption plasmon band to the chemiluminescent emission spectra of luminol. It was revealed (Figure 3.1) that the absorption cross-section of the optimally tuned SNPs is 12 times larger than the geometrical cross-section of SNPs. According to numerical results presented in Figure 3.1, an ideal matching with the first luminol emission peak at 489 nm is achieved for silver hemispheres with 20 nm diameter deposited on the glass substrate (refractive index n = 1.51).

However, the calculations show that the absorption plasmon band of SNPs on the glass substrate provides no spectral overlap with the second luminol chemiluminescence emission peak located at 452 nm even using the smallest hemispheres nanoparticles. Yet the resonance condition between the absorption plasmon band and the luminol emission peak at 452 nm may

be restored for the truncated sphere of 20 nm in diameter and the height of h = 13 nm. It should be noted that the possibility for resonance plasmon band tuning of gold nanoparticles toward long-wavelength range was numerically demonstrated by means of the truncating the spherical nanoparticles[81]. It also should be noticed that the high refractive index substrates (e.g. sapphire having the refractive index as high as 1.77 [82, 83] and titanium dioxide substrate) lead to inefficient overlapping of the silver nanoparticle plasmon band with the luminol emission since the long-wavelength shift is too large even for the very small silver hemispheres. On the contrary, the high refractive index substrates can be considered for those chemiluminophore molecules that have emission bands in the long-wavelength part of the spectrum. Therefore, the glass substrate is a more reasonable choice to enhance the chemiluminescence of luminol using the SNPs array.

3.2 Numerical calculation for alternative metal-enhanced chemiluminescence configuration on dielectric substrate

As luminol is not the sole substance to be widely applied as chemiluminophore, here a manifold of substrate-nanoparticle pairs optimized for the metal-enhanced chemiluminescence are presented. The following well-known chemiluminophores: $KMnO_4$ in Figure 3.2, Lucigenin in Figure 3.3a, b, Ce (IV) in Figure 3.3c,d, and bis-(2,4,6-tricholorophenyl) oxalate (TCPO) in Figure 3.3e,f have been considered.
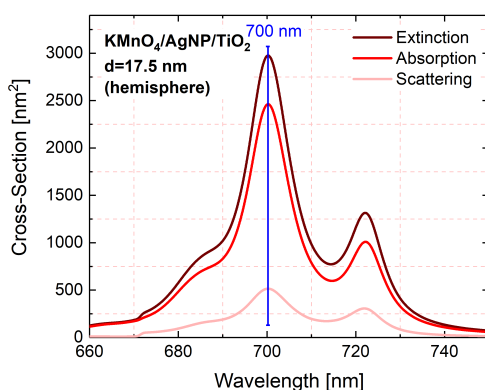
Figure 3.2: Calculated absorption, scattering and extinction cross-section spectra of the silver nanoparticles deposited on the TiO_2 substrate. The diameter of the hemisphere is d = 17.5 nm.

The diameters of silver hemispheres were optimized for KMnO$_4$ chemiluminescent emission spectra (Figure 3.3) with the emission band maximum at 700 nm [84]. As an alternative example of a chemiluminescent agent, Lucigenin is considered. This substance is widely used in analytical science whereas its emission band maximum is located at 480 nm [85–88] (see Figure 3.3a,b). The scattering, absorption, and extinction cross-section spectra of silver hemisphere optimized for Cerium (IV) chemiluminescent emission spectra are presented in Figure 3.3c,d. The emission band maximum lies at $\sim$ 550 nm [89, 90]. Then, the suitable parameters for the plasmon nanoparticle on top of the dielectric substrate for TCPO chemiluminescence emission spectra were computed. The emission band maximum is at 485 nm (Figure 3.3e,f) [91].
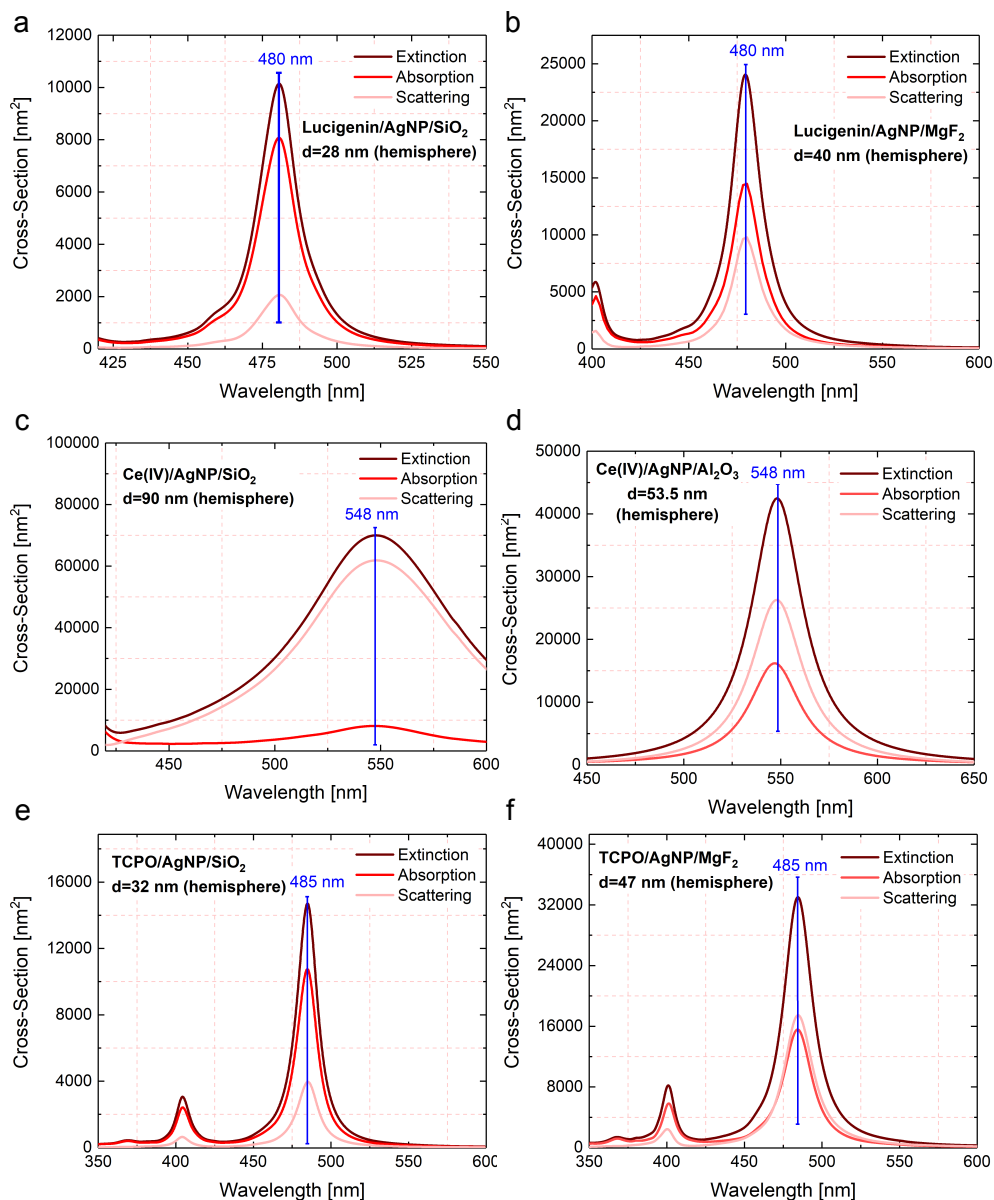
Figure 3.3: Calculated absorption, scattering and extinction cross-section spectra of the silver nanoparticle: **(a)** deposited on the SiO$_2$ substrate for Lucigenin. The diameter of the hemisphere is d = 28 nm. **(b)** the silver nanoparticle on the MgF$_2$ substrate with diameter of 49 nm for Lucigenin system. **(c)** deposited on the SiO$_2$ substrate for Ce (IV). The diameter of the hemisphere is d = 90 nm. **(d)** the silver nanoparticle on the Al$_2$O$_3$ substrate (d = 53.5 nm). **(e)** deposited on the SiO$_2$ substrate for TCPO system. The diameter of the hemisphere is 32 nm. **(f)** the silver nanoparticle on the MgF$_2$ substrate with the diameter of 47 nm for overlapping with TCPO chemiluminophore.

3.3 Experimental results

In this section the relative contributions of plasmonic and catalytic mechanisms in the chemiluminescence intensity enhancement due to the silver metasurface was experimentally investigated. Firstly, let us consider the process scheme of step-by-step morphology modification starting from a deposited thin film to the inhomogeneous ensemble of silver nanoparticles, as shown in Figure 3.4. This technique was used to obtain plasmonic nanoparticles optimized for the luminol chemiluminescence enhancement. Chemiluminescence of different chemiluminophores may be enhanced via the suggested technique, the dedicated choices of substrates, and annealing procedures [69].
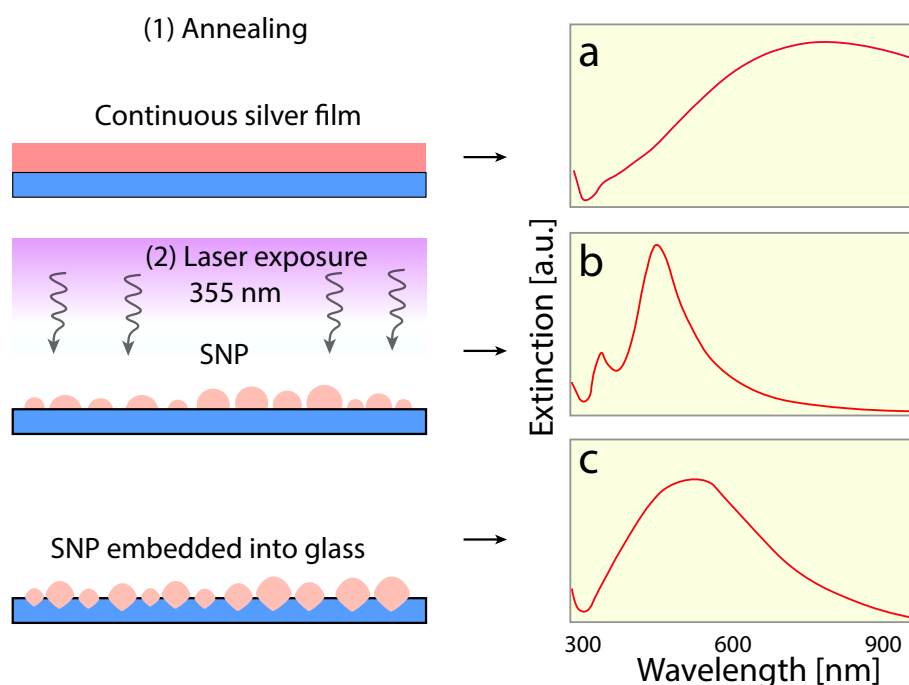
Figure 3.4: The proposed process scheme of silver nanoparticles ensemble preparation and the extinction spectra evolution: **(a)** a continuous film, **(b)** after annealing treatment, and **(c)** after laser exposure.

Using the time/temperature dependence of the annealing process, the desired SNPs shape and size distributions that lead to the plasmonic band in the needed spectral range were achieved. However, the fabricated self-organized metasurfaces of SNPs were mechanically unstable and may be damaged by organic/non-organic solvents, i.e. water, ethanol, hexane, and others. To overcome this limitation, a novel approach for strong adhesion of SNPs to the dielectric substrates was developed. In particular, after the annealing process, the thin silver film was

exposed to the pulsed laser irradiation at the wavelength of 355 nm.

Figure 3.4a shows the extinction spectrum of the continuous silver film, whose plasmon absorption band is out of the spectral region necessary to overlap with the luminol emission band. As it is seen in Figure 3.4b, the extinction spectrum after the subsequent annealing process is characterized by the sharp absorption plasmon resonance band in the visible range. Under the laser irradiation, the plasmon band broadens whereas its overlap with chemiluminescence emission spectra becomes greater (Figure 3.4c). From the experimental point of view, it is essential to improve the chemical and mechanical stability of the metal films because the chemical reagents used in the chemiluminophore solution are very aggressive. It was found that dripping the mix of *"solution 1"* and *"solution 2"* (for more details, see Section 2.3) does not degrade the substrate with the SNP metasurface. It is worth noting, the adhesion of SNPs to the substrate also improved (Figure 3.4c). This property was confirmed by scratching the film with a sharp object. Thus, the laser irradiation leads to the formation of stable in organic solvents and resistant to mechanical damages samples. These samples are suitable for chemiluminescence experiments, unlike the untreated samples.

To clarify the morphology of the prepared SNP metasurface, the SEM images before and after the annealing process were analyzed, as depicted in Figure 3.5.
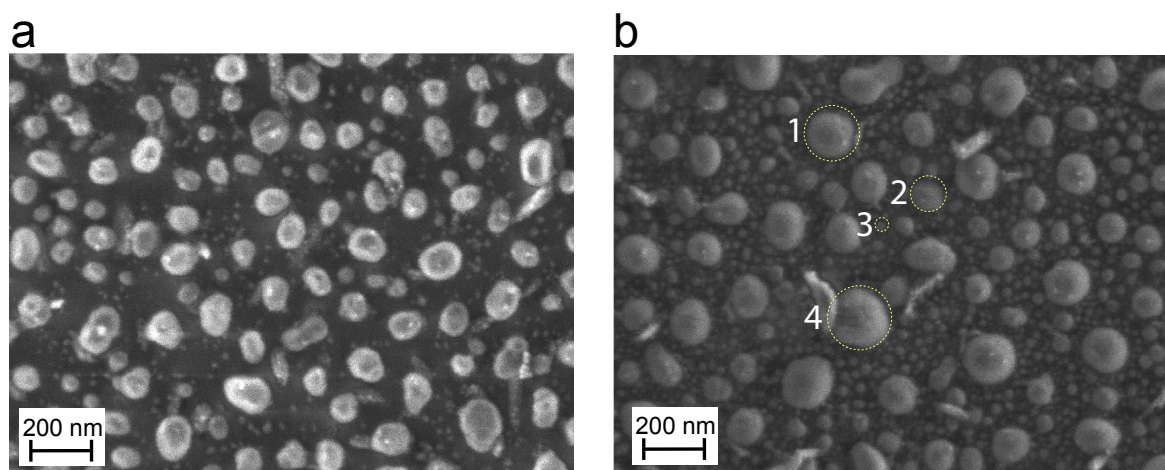
Figure 3.5: Scanning electron microscope images of SNPs on the glass substrate. The scale bar is 200 nm. The size distribution of SNPs before **(a)** and after laser exposure **(b)**. SNPs in **(b)** varing from 10 to 200 nm (1 - 155 nm, 2 - 105 nm, 3 - 20 nm, 4 - 200 nm).

Two distinct ensembles of larger and smaller nanoparticles in both images are observed. The image of SNPs obtained after the annealing procedure shows the presence of rather similar

larger nanoparticles with diameters not exceeding 160 nm. After the laser irradiation, all SNPs become larger and more rounded. At the same time, the size distribution becomes broader and the distinction between ensembles of larger and smaller particles becomes more pronounced. (Figure 3.5). As a result, the extinction spectrum shifts and broadens as can be seen in Figure 3.4.

The measured extinction spectra of the SNP metasurface after the laser irradiation exhibit the pronounced plasmon bands in the range of 350 to 650 nm with a maximum at 482 nm (Figure 3.6).
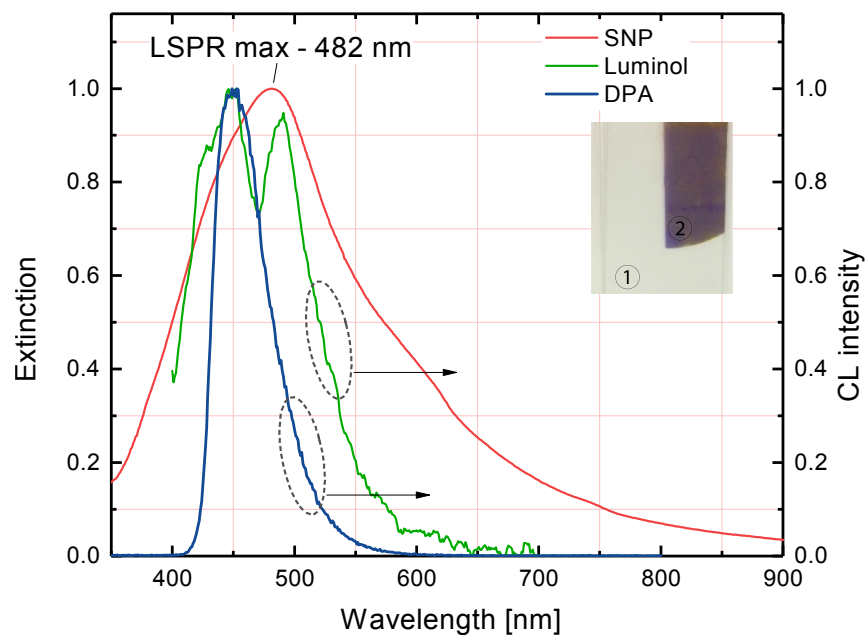
Figure 3.6: The extinction spectra overlap of SNPs obtained via PVD with subsequent thermal annealing/laser exposure (red curve) with the chemiluminescence (CL) emission spectra of: luminol (green curve) and DPA (blue curve). The inset shows an image of the cover-glass (1) partially covered with SNPs (2). All spectra are normalized.

The inset of Figure 3.6 shows the image of the substrate (1) with the SNPs (2) fabricated via PVD and subjected to both the subsequent annealing and laser irradiation. It was noticed that the film has a definite brown color that corresponds to the spectral position of the absorption band of the fabricated SNPs, as shown in Figure 3.6. As it was mentioned above, boosting the chemiluminescent emission requires the spectral overlap between the chemiluminophore (donor) luminescent band and SNPs (acceptor) absorption band. To show this overlap, the normalized chemiluminescent spectrum (CL) of luminol is plotted in the same graph. The

chemiluminescent spectra of luminol consist of two overlapping emission bands with maxima at the wavelengths of 452 nm and the wavelengths of 489 nm, respectively. The plasmon band of the prepared SNP samples is overlapped with both luminol chemiluminescence emission bands. In addition, it was observed that the DPA chemiluminescent emission band (Figure 3.6) spectrally overlaps with the plasmon band.

Finally, the influence of the synthesized SNPs on chemiluminophore molecules has been investigated. A straightforward experimental procedure in order to show the MEC effect was employed. 30 μl of "solution 1" was dripped onto the bare glass substrate just at the edge of SNPs, as shown in the inset of Figure 3.6. Then, 30 μl of "solution 2" was dripped onto another glass slide and both slides are pressed to each other in such a way to mix the both solutions. The thickness of the gap between two substrates was estimated to be about 10 μm based on the simulation of the oscillations in the transmission spectrum [92]. The sharp jump in the chemiluminescence intensity of both luminol and DPA is clearly seen at the edges of SNP covered regions (Figure 3.7). In this respect, it was shown that the chemiluminescence intensity of luminol in the presence of SNPs is enhanced 1.6 times, while in the case of DPA the enhancement factor reaches 1.5.
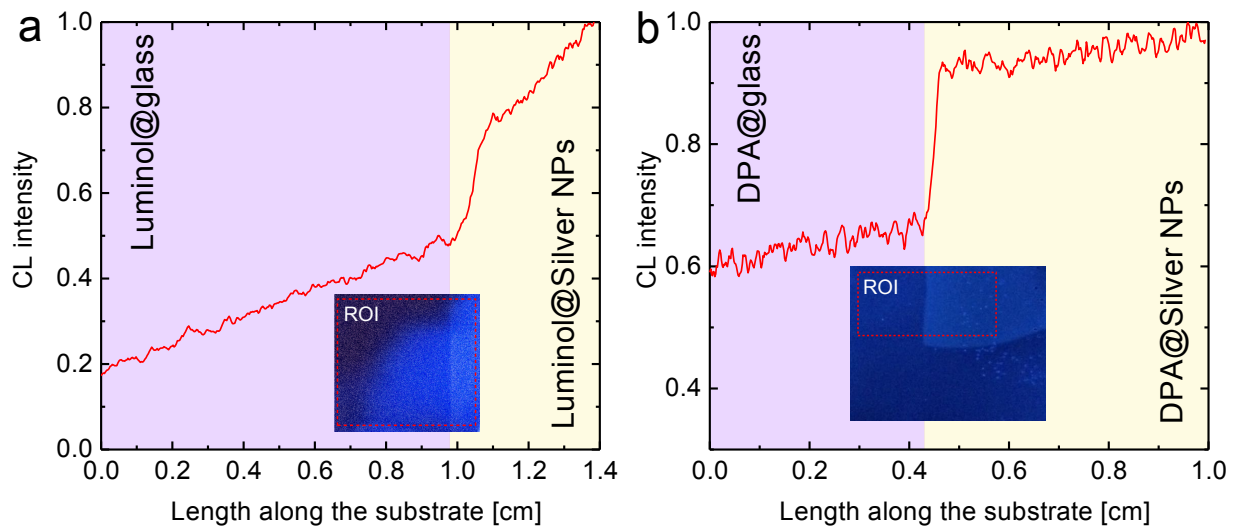
Figure 3.7: Distribution of chemiluminescence intensities over the indicated regions of interest (ROI) for Luminol **(a)** and DPA **(b)**. Red curves represent the chemiluminescence intensity integrated over the vertical axes and plotted against the horizontal axes of the corresponding chemiluminescent images. The jumps at the borders of the dedicated silver metasurfaces are clearly seen both in the pictures and in the plots. The plots background colors are used to guide the eyes.

3.4 Influence of the Purcell effect on the MEC

When reagents are contacted directly to the silver metasurface with the plasmon resonances absorption band within the chemiluminescence bands of luminol, the chemiluminescence intensity is increased 1.6 times. To clarify the relative role of the Purcell effect and the catalytic effect of silver in this enhancement, additional experiments were performed. An identical SNPs substrate was covered with 2 nm SiO_2 spacer layer (the inset of Figure 3.8a). It was expected that the catalytic effect of SNPs completely disappears since it requires direct contact between the reactants and nanoparticles. Nevertheless, in spite of the increased distance between the reactants and SNPs, the Purcell effect remains. Indeed, in the presence of the spacer, the enhancement factor drops to 1.3 factor (Figure 3.8a).
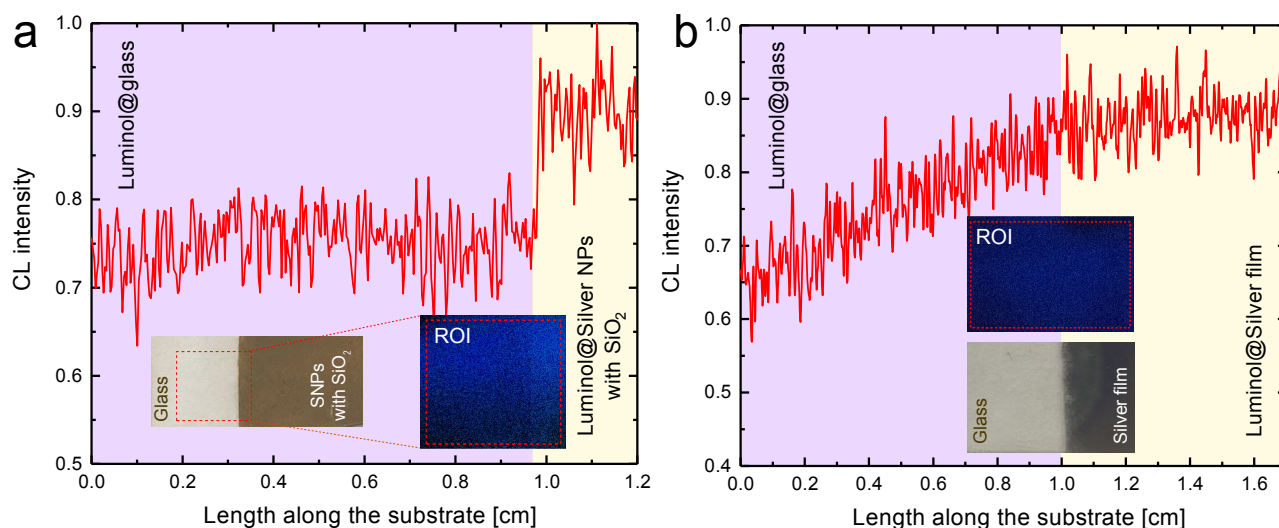
Figure 3.8: Distribution of chemiluminescence intensities over the indicated ROI for luminol on the dedicated silver metasurface covered by a 2 nm thick SiO_2 spacer **(a)** and on the silver film that have plasmon resonances detuned from the chemiluminescence bands of luminol **(b)**. The insets also show the images of the substrates before the luminol addition.

Thus, the decisive role of the Purcell effect was confirmed. In this case, an increase in chemiluminescence enhancement with a decrease in the distance between reagents and SNPs was naturally explained. In order to estimate the role of catalysis in chemiluminescence enhancement in the absence of the spacer, the experiment with a silver film that has no plasmon resonances in the chemiluminescence bands of luminol was also conducted. If chemiluminescence is also enhanced in this case, this enhancement should be attributed to the catalytic effect of silver. However, in Figure 3.8b one can observe no difference in the

chemiluminescence intensities from the regions of the plain dielectric substrate and silver film without plasmon resonances. Consequently, the 1.6-fold enhancement of chemiluminescence, which is observed upon direct contact of the reagents with a silver film with plasmon resonances in the spectral range of chemiluminescence bands of luminol, can be completely attributed to the Purcell electrodynamic effect.

3.5 Summary

In summary, a novel approach has been proposed in designing new materials assembled from nanoparticles for enhancing chemiluminescence. All of them are promising in terms of delivering substantial enhancement in specific and accurate detection of analytes, which are impossible via traditional approaches. The proposed technique was used to fabricate the supported silver nanoparticles ensemble with the plasmon band that peaks at 482 nm and overlaps well with the luminol emission bands. Laser treatment is shown to provide the enhanced chemical and mechanical stability of the obtained thin films. The combination of these materials with recent advances in the chemiluminescence enhancement effect for applying in flow-injection systems opens the door for new chemiluminophores-based light sources. These light sources, where a poor quantum emitter (chemiluminophore) is coupled with an efficient plasmonic nanoantenna, failed to be achieved by conventional manufacturing processes with the particle size and shape fixed. It was revealed that the particle arrangement on the surface of the transparent dielectrics enables to control the distance between the light-emitting species and nanoantennas to elucidate the role of the Purcell effect in the observed chemiluminescent enhancement. The inert layer, placed on top of the self-organized metasurface of SNPs, allows to eliminate the catalytic effect contribution to the MEC activity and shows a gain in the luminescence intensity of chemiluminophore molecules due to the retained Purcell effect. I have concluded that the fabrication of SNPs using the physical vapor deposition technique in a vacuum, followed by the self-organization of nanoparticles, is an affordable and convenient method leading to the plasmonic enhancement for the luminol and *9,10*-diphenylanthracene chemiluminescence.

4   Surface-enhanced near-infrared absorption (SENIRA) spectroscopy

In this chapter, the mechanism of local field enhancement in molecular overtones was explored for the first time. The local field enhancement can be realized with plasmonic materials by means of collective oscillations of free electrons in form of extended surface plasmon-polariton (SPP) in thin metal films [1, 8, 93–96] or localized surface plasmon resonance (LSPR) in plasmonic nanoantennas [36, 97–99]. Meanwhile, the influence of extended surface plasmon on absorption by molecular overtones was explored. It was shown that 100 times enhancement can be achieved [100]. This enhancement was observed when the absorption band of the molecular vibration N-H was detuned from the plasmonic resonance. Previously it was found that the electronegative gold nanospheres are readily adsorbed on the tapered microfiber and electrostatically bonded to amine-based molecules. Despite the non-resonant condition between the gold nanospheres and the amine-based molecules, it was shown that the enhancement of the integrated overtone absorption in diffuse light propagation depends on the concentration of nanospheres [101]. Very interesting experimental results were reported in [102]. The authors prepared porous gold nanodiscs that possess a broad plasmon resonance in the near-infrared range. When a random array of such nanodiscs is covered by a thin film of a material possessing absorption bands in the same spectral region, enhanced absorption of the composite material may be observed. Very large, up to four orders of magnitude, enhancement claimed in [102] is due to the use of analyte in the form of a self-assembled monolayer. In this case, an analyte presents exclusively in hot-spot regions. In the general case, the analyte occupies much larger volumes where the field enhancement is lower. Hence, the overall enhancement becomes lower as well. Despite this experimental observation of surface-enhanced near-infrared absorption (SENIRA) of molecular overtones with plasmonic nanoantennas, this effect was not explored theoretically. The first work is related to the coupling

of vibrational mode and plasmonic dipole oscillation of gold nanorods was theoretically implemented using a homogeneous weakly absorbing medium [103].

4.1 The *isolated* gold nanoparticles with prolonged shape coupled with stretching overtone modes

In this section, the possibility to enhance absorption by molecular overtone transitions in the near-field of plasmonic nanoantennas such as gold nanorods (GNRs) due to the combination of localized plasmon resonance and lightning rod effect [104] has been theoretically explored. Below it was shown that when the resonance conditions are met at 1.5 μm the differential extinction due to the excitation of overtones of N-H and C-H stretching modes can be enhanced by two orders of magnitude as compared to the ordinary extinction of the same amount of molecules.

Figure 4.1 shows the system was studied. Gold nanorods were modeled as cylinders capped by hemispheres on both sides. Dimensions of all elements are given in the text and figure captions. Weakly absorbing medium, described by the complex permittivity of N-Methylaniline molecule, encapsulates a gold nanorod and nanoellipsoid in a homogeneous shell-like manner. The incident beam is directed perpendicular to the gold nanoparticles as indicated by vector $\boldsymbol{k}$ and polarized along the gold nanoparticles.
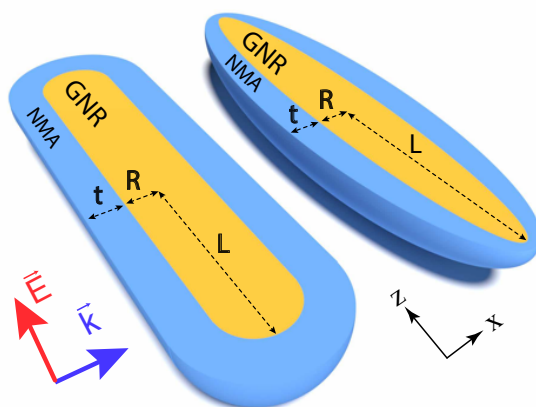
Figure 4.1: Schematics of systems with gold nanorods (left) studied in numerical simulations and nanoellipsoids (right) used in the analytical model. The shells are made of N-Methylaniline (NMA). L and R are semi-major and semi-minor axises of gold nanoparticles respectively, while t is the thickness of molecular shells. The incident wave is polarized along the rod.

The contribution of GNR parameters in the effect of SENIRA by molecular overtones was studied . For this, an analytical model of a confocal ellipsoidal core-shell nanoparticle was built. In the framework of quasi-static approximation, the absorption, scattering, and extinction cross-sections were expressed through the particle polarizability [2, 15]

First, it was analyzed how the LSPR position depends on the analyte shell thickness, t. Since the enhanced near-field rapidly decays with the distance from the surface, effective interaction is possible here only at distances comparable to the nanoantenna dimensions. In addition, the aspect ratio of the nanoantenna should provide the resonant interaction between the longitudinal plasmon and an overtone excitation. Therefore, the semi-minor axis of the gold nanoellipsoid was chosen as 5 nm, while varying the semi-major axis until the LSPR band overlaps with an overtone mode. For this, the extinction cross-sections of gold nanoellipsoids covered by thin shells of NMA were calculated in the form of confocal ellipsoids as demonstrated in 4.2.
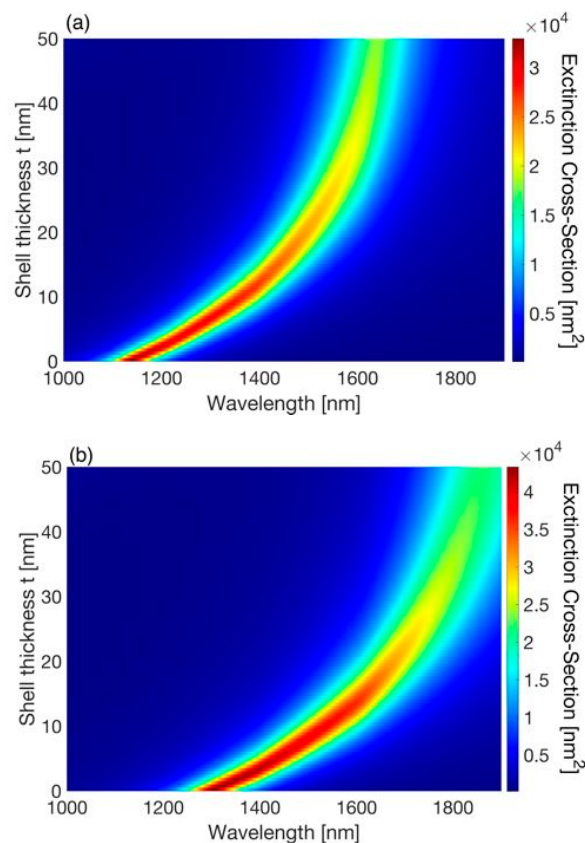
Figure 4.2: Extinction cross-sections of gold nanoellipsoids with NMA shells of different thicknesses. **(a)** the semi-major axis of the gold core is L = 55.9 nm **(b)** the semi-major axis of the gold core is L = 68.1 nm. The semi-minor axis is R = 5 nm in both cases.

Figure 4.2a shows the extinction cross-section of GNR as a function of the NMA shell thickness. The semi-major axis of the gold core is L = 55.9 nm that leads to the exact resonance with the first overtone of N-H mode when the shell thickness is t = 20 nm. Figure 4.2b shows the same dependence when the semi-major axis of the gold core is L = 68.1 nm that leads to the exact resonance with the first overtone of C-H mode when the shell thickness is t = 20 nm. The long-wavelength shift of plasmon bands as a function of the shell thickness t is rather strong at small shell thicknesses for $t < 40$ nm but saturates at shell thicknesses larger than $t > 40$ nm.

As a proof-of-concept, a numerical model using COMSOL was built, where the tuning of the plasmon bands of GNR with the NMA overtone bands was shown based on the numerical calculation. Figure 4.3 shows calculated extinction (ECS), absorption (ACS) and scattering (SCS) cross-section of gold nanorods with NMA shell for $L = 49.9$ nm (Figure 4.3(a)) and for $L = 60.6$ nm (Figure 4.3(b)). The nanorod diameter is 10 nm. The length of GNR was chosen such that it overlaps with the overtone bands of N-H located at 1494 nm and C-H located at 1676 nm. Considering the results presented in Figure 4.3 it was found that extinction is governed by absorption, while the scattering contribution is negligible.
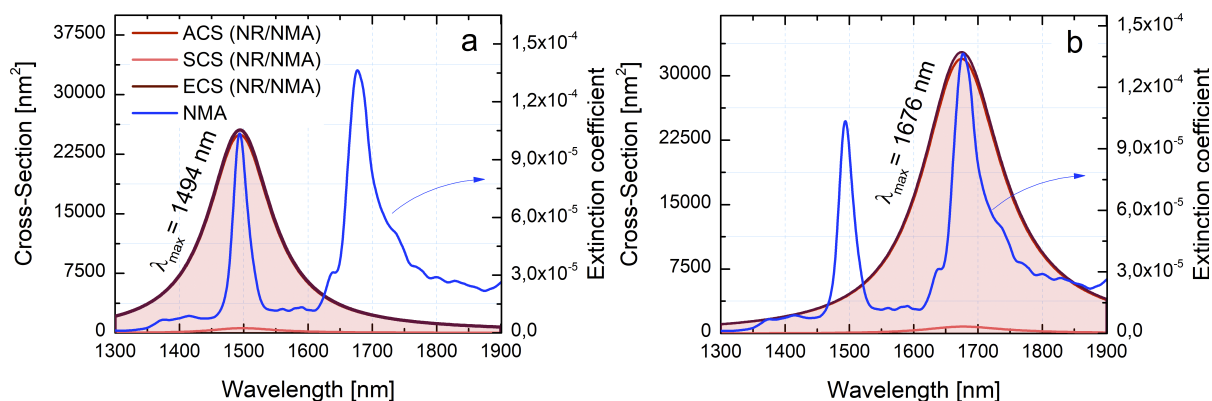
Figure 4.3: Extinction (brown), absorption (red) and scattering (pink) cross-sections of gold nanorods with NMA shell. The nanorod diameter is set to 10 nm for **(a)** $L = 49.9$ nm, **(b)** $L = 60.6$ nm. The thickness of the NMA molecular shell is homogeneous and equals to t = 20 nm. Extinction coefficient of NMA (blue) is also shown for comparison.

The advantage of using GNR becomes evident when the concept of differential extinction is employed [100]. Experimentally, the differential absorption can be realized by comparing the extinction cross-section of a GNR surrounded by the analyte shell with that of a GNR surrounded by a shell of non-absorbing material that mimics only the mean value of the analyte's refractive index. Thus, the difference between cross-sections of absorbing and

non-absorbing materials represents the influence of the analyte absorption and anomalous dispersion on the LSPR intensity and spectral position. On the other hand, it includes also the influence of the LSPR on the analyte absorption.

Quantitatively, differential extinction, DE, as [100, 103]:

$$\text{DE} = \sigma_{ext}^{NR/NMA} - \sigma_{ext}^{NR/NMA*} \tag{4.1}$$

where the first term $\sigma_{ext}^{NR/NMA}$ represents the extinction cross-section of GNR with NMA shell, while the second term $\sigma_{ext}^{NR/NMA*}$ represents the same value with NMA replaced by a dummy medium of constant dielectric permittivity. Figure 4.4 shows the calculated DE in spectral ranges of the first overtones of the N-H and C-H stretching modes. Interestingly, the sign of wavelength dependent DE alternates in both cases.
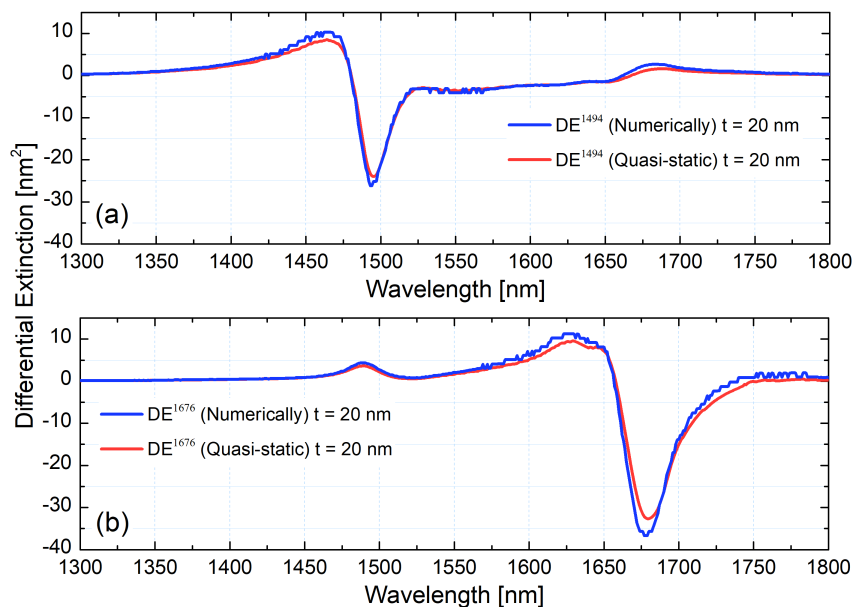
Figure 4.4: Comparative analysis of differential extinction (DE) spectra of gold nanorod and nanoellipsoid with NMA shells: **(a)** with semi-major axes L = 49.9 (*nanorod*) and L = 55.9 nm (*nanoellipsoid*). **(b)** L = 60.6 (*nanorod*) and L = 68.1 nm (*nanoellipsoid*). Blue curves correspond to numerically calculated results (*nanorod*) while the red curves correspond to results obtained in the quasi-static approximation (*nanoellipsoid*)

The aspect ratio of nanorods was chosen in Figure 4.4a as L/R = 9.98 and the aspect ratio of nanorods for the Figure 4.4b as L/R = 12.12. Numerically calculated DEs (blue) are very well reproduced by the DEs obtained in the quasi-static approximation (red) provided the aspect ratios of the GNRs are adjusted to match the plasmon resonance with the corresponding

overtone (L/R = 11.18 Figure 4.4a and L/R = 13.62 in Figure 4.4b). It is important to note that in the case exact resonance between the plasmon in the GNR and the molecular overtone transition the sign of DE alternates. Contrary to that in the non-resonant case DE is strictly positive. It may be clearly seen in Figure 4.4 for C-H overtone transition at 1676 nm when the plasmon in the nanorod is tuned on 1494 nm (Figure 4.4a) and for N-H overtone transition at 1494 nm when the plasmon in the nanorod is tuned on 1676 nm.

To explore the role of GNRs in the detectivity enhancement of small amounts of NMA, extinction cross-sections of pure NMA shells (without GNR) were compared with the DE. Figure 4.5 shows the dependence of both values on the NMA shell thickness.
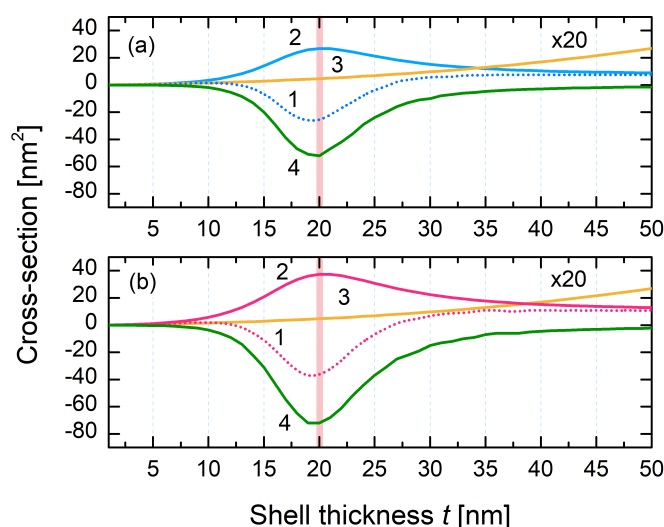
Figure 4.5: (a) Optical cross-section as function of shell thickness of NMA: (1) differential extinction, (2) absorption cross-section of NMA shell encapsulating GNR, (3) extinction cross-section of the NMA shell without the GNR, and (4) the difference between ACSs of the GNR -with and -without the NMA shell GNR semi-major axis **(a)** L is 49.9 nm and the wavelength is set to 1494 nm. Absorption cross-section of the NMA shell when the GNR is absent is multiplied by 20. **(b)** same graphs as in subplot **(a)** for the case when the wavelength is set to 1676 nm, while L is 60.6 nm.

When the resonance conditions are met, the DE values exceed the extinction cross-sections of the pure NMA shells by two orders of magnitude. In particular, the first overtone of N-H stretching mode located at 1494 nm is enhanced 114 times, while the first overtone of C-H stretching mode located at 1676 nm is enhanced 135 times. Figure 4.5a shows variations in cross-sections versus shell thickness for $\lambda = 1494$ nm and the GNR semi-major axis is equal 49.9 nm. The resonance conditions for the plasmon excitation are met when the shell thickness is equal to 20 nm. Similarly, the optical properties in the form of ECS and ACS as a function of

the shell thickness are presented in Figure 4.5(b) whereby $\lambda = 1676$ nm with GNR semi-major axis $L = 60.6$ nm. Enhanced absorption in the NMA shell due to the plasmon near-field is accompanied by reduced absorption in the GNR due to the screening effect [105]. As a matter of fact, neither enhanced absorption in the shell nor the reduced absorption in the core can be observed in the far-field separately. However, they combine favorably leading to very large DE values.

DE dependence on both: the NMA thickness and the incident radiation wavelength based on the analytical model is presented in Figure 4.6.
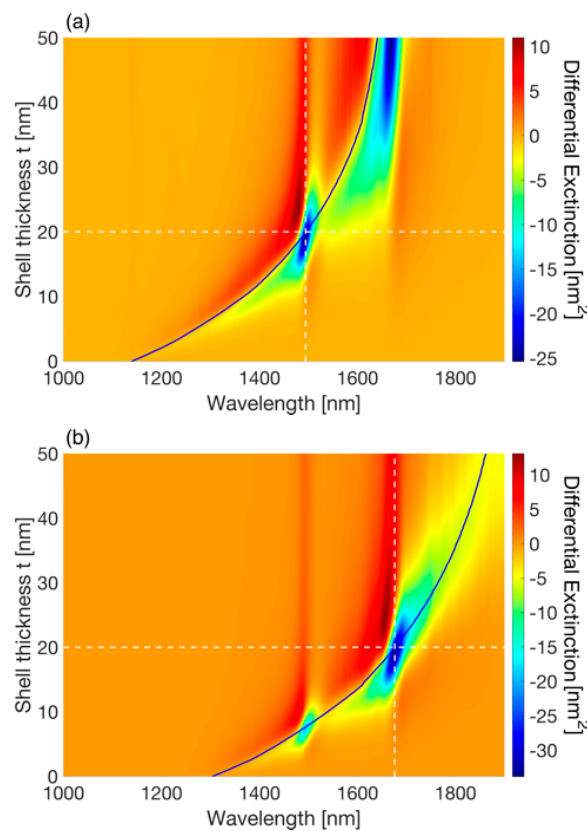
Figure 4.6: Differential extinction (DE) values are given as the functions of the NMA shell thickness and the incident radiation wavelength for GNR with semi-major axis of: $L = 55.9$ nm **(a)** and $L = 68.1$ nm **(b)**, respectively. The vertical dashed lines show the position of two overtone bands, while the horizontal dashed lines mark the shell thickness ($t = 20$ nm) that leads to tuned plasmon resonance with the corresponding overtone band. The dark curve is drawn through the maxima of the plasmon resonances.

In both plots, the dark curve corresponds to the maxima of the LSPR. The vertical dashed lines mark the location of overtone bands, while the horizontal dashed lines correspond to NMA thickness of 20 nm that leads to a coincidence of the LSPR in the chosen nanorod with

the corresponding overtone band. Inspection of Figure 4.6 leads to the conclusion that the largest absolute value of DE is obtained at the resonance and the sign of this largest DE value is negative. The main features of DE already noted in particular cases presented in Figure 4.4 and Figure 4.5.

4.2 The *metasurface* of gold nanoparticles coupled with stretching overtone modes

Earlier, it have been shown that the size and the aspect ratio of prolate gold nanospheroids may be chosen in such a way that their LSPR bands overlap with first-order overtones of C-H and N-H stretching modes of organic substances [106]. In the previous section, the size and the shape of a rod-like gold nanoparticle were optimized to lead for the maximum overtone absorption enhancement [107]. However, using the isolated gold nanoparticles implies that only a very small fraction of the analyte is placed in the amplified near field. This circumstance limits the overall enhancement provided by LSPR. To get the most of the plasmon field amplification, metal nanoparticles are to be arranged in a dense array forming a metasurface. This way, a larger portion of analyte molecules may be placed in the regions of enhanced electromagnetic near-field of nanoparticle [108]. Moreover, electromagnetic interaction between neighbor nanoparticles leads to an additional mechanism of local field enhancement when the conditions for Rayleigh anomaly are fulfilled [5, 109–117]. Fabrication of nanoparticle arrays of required density is feasible via electron beam lithography (EBL) [118, 119] although the shapes of the nanoparticles defined by EBL on a substrate are closer to nanoscale parallelepipeds (NPs) rather than nanorods or nanospheroids.

Because of that, this section is devoted to the investigation of planar metasurfaces consisting of nanoparallelepipeds (NPs) that can be fabricated easily and prepared specifically for overtone detection in the range of wavelengths around 1.5 μm and around 1.67 μm. The proposed structure utilizes a combination of localized plasmon resonance in isolated gold NP with Rayleigh anomalies of their periodic array. By incorporating the plasmonic metasurface into a weakly absorbing organic medium a 22.5-fold enhancement of the first overtone of N-H stretching mode in the NIR spectral range has been demonstrated for the first time. Application of the designed gold metasurface may be beneficial in biomedicine [120], non-destructive testing [121], food quality analysis [122–124] and etc.

4.3 Numerical model

To obtain a realistic model an infinite array of gold nanoantennas was considered in the form of parallelepipeds arranged in a square lattice on a dielectric substrate and covered by a thin layer of analyte molecules. Periodic boundary conditions were used to study the influence of lattice periodicity on the enhancement of overtone absorption bands. Thus, the gold metasurface is modeled as a square lattice of prolonged NPs with variable length L, while width w and height h were fixed and equal to 20 nm (depicted in Figure 4.7a, b).

Since the periodic boundary conditions were used, the results are strictly valid for the infinite structures, while all real structures are finite. There are several studies devoted to the relation between the optical properties of finite structures of different sizes and the corresponding infinite structure [125–127]. Although there is no general solution, in most cases several hundreds of periods are enough for the convergence.
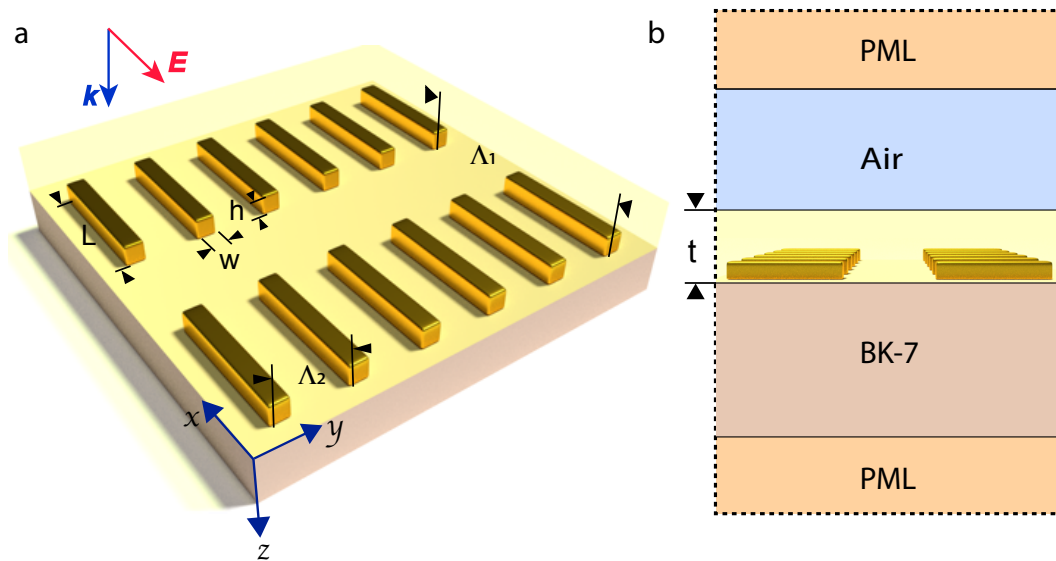
Figure 4.7: **(a)** 3D schematics of the gold metasurface modeled in COMSOL Multiphysics software. The width and height of gold nanoparallelepipeds (NPs) in the array are of $w = h = 20$ nm, while the length is varied. The longitudinal and transverse lattice constants are defined as Λ_1 and Λ_2. t designates the analyte film thickness. The incident light propagation direction k and polarization E are also shown. **(b)** Schematics of 2D cross-section of the model. Furthermore, the gold metasurface submerged into the analyte layer, the structure involves a BK7 glass substrate and an air layer with refractive index $n = 1$. The sample is placed between perfectly matched layers (PML).

4.4 Optimization of the metasurface

When the lattice periods become comparable to the sizes of the individual nanoantennas, plasmon resonances start to interact with the lattice resonances. Hence, the optimization procedure becomes very complex. To facilitate the optimization, the Rayleigh anomaly was studied that corresponds to the first diffraction order which starts to propagate into the substrate with the refractive index $n = 1.5$ at the wavelength of N-H overtone $\lambda = 1494$ nm (in a vacuum). The rough approximation of the lattice constant is $\Lambda_1 = \lambda/n$, as shown in Figure 4.7a, gives a value of 1 μm. Next, the length of the nanoantenna is to be chosen in such a way that the effective polarizability of the nanoantennas comprising the metasurface α^* reaches its maximum value. According to the well-developed theory of diffractively coupled localized plasmon resonances in the framework of the coupled dipole approximation (CDA) [5], α^* may be calculated as follows:

$$\alpha^* = \frac{1}{\frac{1}{\alpha} - S}, \tag{4.2}$$

where α denotes the polarizability of an isolated nanoantenna that depends solely on its size and shape (at the fixed wavelength). The dipole sum S accounts for the dipole-dipole interaction between nanoantennas and only depends on the lattice periods Λ_1, Λ_2 (see Figure 4.7a). According to Equation (4.2) α^* reaches its maximum when the real parts of S and α^{-1} are equal. From the calculated results presented in [5], it was learned that S is very small anywhere but at the narrow window around $\frac{\Lambda_2}{\lambda} \approx 1$ it has a maximum. On the other hand, the LSPR wavelength of NP of a fixed cross-section is a monotonic function of its length as it may be seen below in Figures 4.8 and 4.9. Hence, to maximize the effective polarizability at the wavelength of the molecular overtone transition, the length of the nanoantenna should vary together with the lattice periods. The length of the resonance antenna is expected to have a minimum as a function of the lattice period. Considering this, the numerical simulation was performed and the structures of gold metasurfaces with certain LSPR bands were found, optimized for sensing of functional groups overtone transitions at $\lambda = 1494$ nm and $\lambda = 1676$ nm.

4.5 Dependence of the collective LSPR spectral position on the gold metasurface parameters

The dependence of the transmission dip location on the nanoparticle length has been investigated. The simulations for the light polarized along the length of gold NPs (x-axis) at normal incidence were performed. Figure 4.8 shows the transmission spectra of gold metasurfaces with fixed lattice periods and varying lengths of nanoantennas. In close analogy
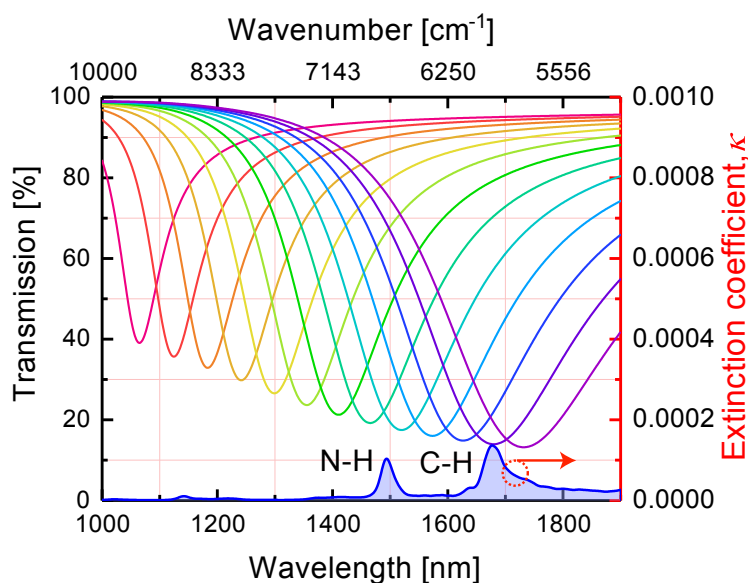
Figure 4.8: Calculated transmission spectra of gold metasurfaces with NPs of lengths L varied from 100 nm (crimson curve) to 220 nm (purple curve) in 10 nm steps, whereas lattice periods were fixed at Λ_1 = 400 nm and Λ_2 = 200 nm. The extinction coefficient of NMA is shown below the transmission curves. The gold metasurface was embedded in NMA with a thickness of 100 nm.

to the well-known dependence of the LSPR spectral position on the aspect ratio of an isolated prolate spheroid, the dip in transmission shifts toward the long-wavelength range when the NPs length L grows. At particular values of length L the transmission dip is defined by collective LSPR overlaps with and couples to the N-H and C-H overtone absorption bands in near-infrared. The transmission dip location depends linearly on the NP's length L as can be seen in Figure 4.9. Figure 4.9 shows the dependence of the LSPR spectral position as a function of NP's length. The gold metasurface was covered by a 100 nm – thick NMA film. The long-wavelength shift of LSPR in longer nanoparticles corresponds to the known from the quasistatic theory behavior of LSPR in prolate particles.
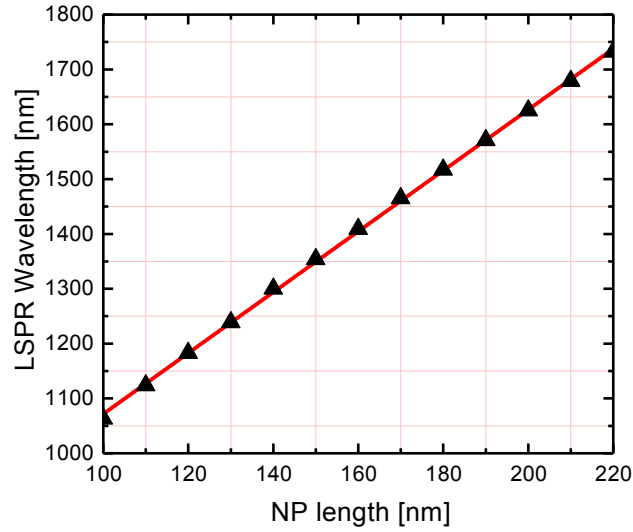
Figure 4.9: The LSPR spectral position as a function of NPs length L. The metasurface parameters were set to the following values: $w = h$ = 20 nm, t = 100 nm, Λ_1 = 400 nm, and Λ_2 = 200 nm.

4.5.1   Near-field enhancement

In this section, the distribution of the enhanced near-field around the gold NP covered by NMA was analyzed. The incident field is polarized along the x-axis while the lattice constants are fixed at Λ_1 = 400 nm and Λ_2 = 200 nm, respectively. Figure 4.10 shows the near-field distribution around one of the gold nanoantennas in the array when the collective LSPR of the metasurface is tuned to coincide with one of the analyte overtones at 1494 nm. The top (a) and side (b) views are both shown in Figure 4.10. Electric near-field polarized along the long axis of the NP exhibits strong enhancement and localization around the antenna tips. Figures 4.10c,d show the corresponding field distributions along the x and z axes. We note that the calculated results shown in Figure 4.10 demonstrate the lightning-rod effect (subplots a, b) as well as the rapid near-field decay (subplots c, d) inside the homogeneous layer of organic molecules and the dielectric substrate. Indeed, the length of NP is more than eight times larger than its width and height. Hence, the main prerequisite for the field concentration at the sharp edges of the nanoparticle and the lightning-rod effect observation is fulfilled. Large jumps of the electric field at the metal surfaces seen in Figure 4.10 is due to the large value of the real part of gold permittivity at λ = 1494 nm (about minus one hundred).
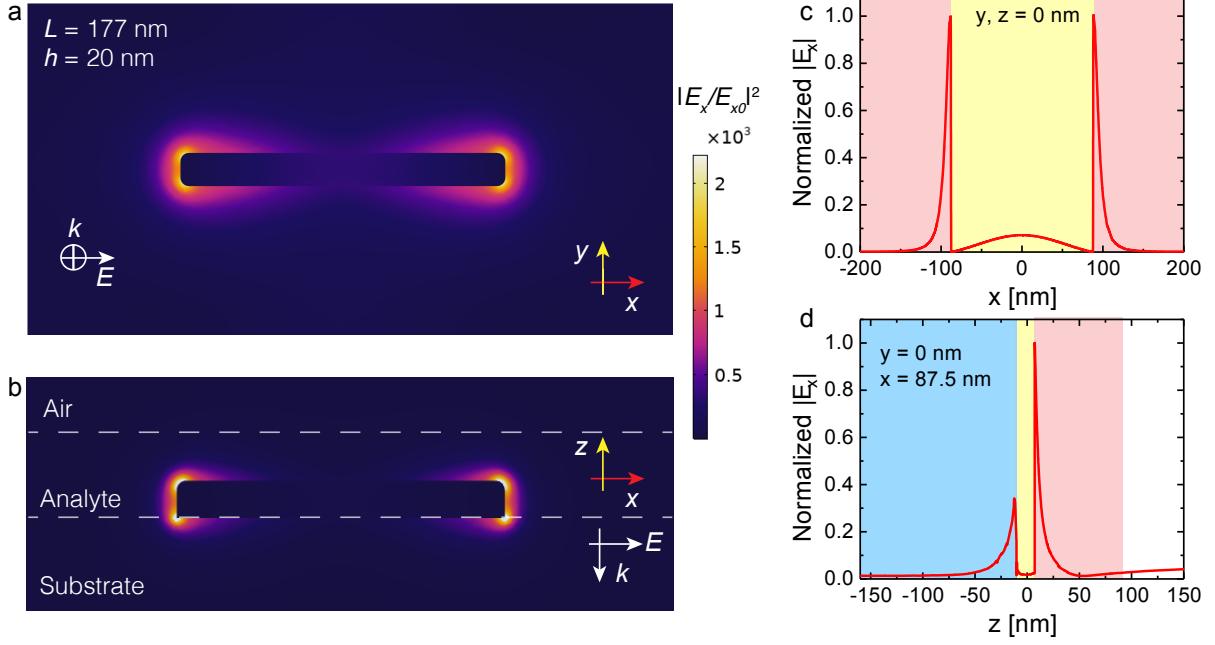
Figure 4.10: The electric field enhancement $|E_x/E_{x0}|^2$ distribution around the gold NP in an array ($\Lambda_1 = 400$ nm and $\Lambda_2 = 200$ nm) surrounded by NMA layer: top view (**a**) and side view (**b**). Normalized electric field distribution along the x-axis goes through the NP center (**c**), the same for the z-axis (**d**) at $x = 87.5$ nm. Color encoding in (**c**) and (**d**): blue—the BK-7 glass substrate, yellow—gold nanoparticle, red—thin layer of NMA layer, white—air. The excitation wavelength is $\lambda = 1494$ nm. The colorbar corresponds for colormaps in (**a**) and (**b**) subplots.

4.5.2 Differential transmission computations

Computation of the differential transmission (DT) spectra is an important step in metasurface design for sensing purposes where the crucial feature is the detection of a small amount of analyte. In particular, the enhanced absorption of the analyte molecules in the near-field of the metasurface is still much smaller than the own absorption of the metasurface in the absence of molecules. In this regard, to reveal the contribution of the gold metasurface, the NPs absorption excluding the presence of molecules must be subtracted from the measured absorption with molecules. Furthermore, it is important to take into account that the metasurface absorption spectra shifts when the permittivity of surrounding changes. Therefore, measurement of the metasurface transmission in air seems infeasible. Instead, the metasurface transmission in contact with a thin film of a transparent material should be considered. The refractive index (RI) of this material should be chosen close to the RI mean value of analyte in the actual spectral range and the film thickness should be the same as that

of an analyte. Based on that, calculation of DT becomes a reliable way to reveal the presence of the analyte and the spectral position of its absorption bands [108]. Figure 4.11 displays an example of the DT spectrum.
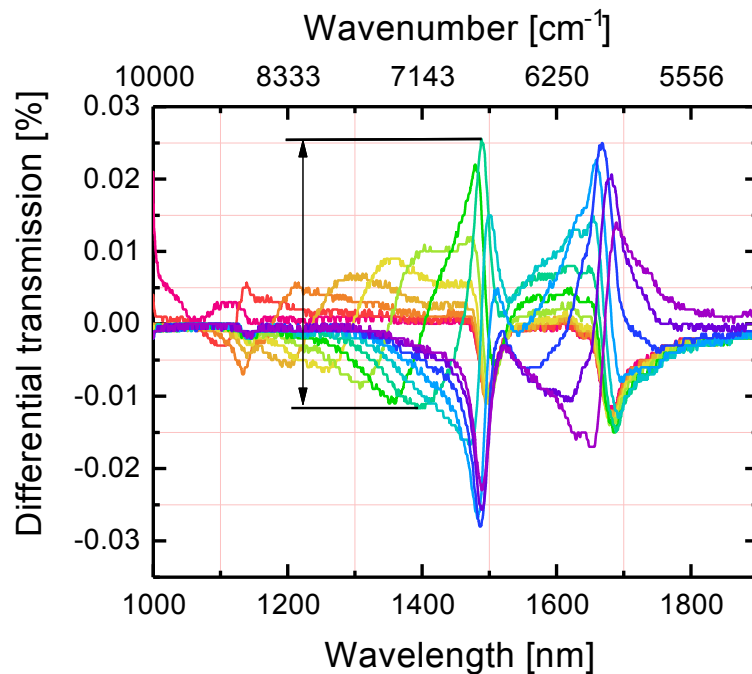
Figure 4.11: Differential transmission (DT) of metasurfaces with 100 nm thick analyte overlayers. The length of NPs varies from 100 (crimson curve) to 220 (purple curve) nm with steps of 10 nm while the lattice periods are of Λ_1 = 400 nm and Λ_2 = 200 nm. The DT contrast is defined as the difference between the maximum and minimum values of DT in the spectral range of the N-H overtone transition and is shown by an arrow for one of the metasurfaces.

Compared to what is shown in the literature [128, 129], the plasmon enhanced absorption DT spectrum demonstrates complex behavior (see Figure 4.11). DT changes its sign as a result of combined action of absorption and anomalous dispersion (Figure 2.3) of the analyte in the spectral ranges of overtone transitions. The regions of enhanced and reduced transmission alternate. Figure 4.12a,b demonstrate the spectral regions where the counterintuitive relation between transmission of the metasurface embedded in NMA and transmission of the same metasurface embedded in immersion oil takes place. The structure covered by a dispersive and absorptive NMA film transmits more light than the same structure embedded in the transparent and dispersionless immersion oil film.
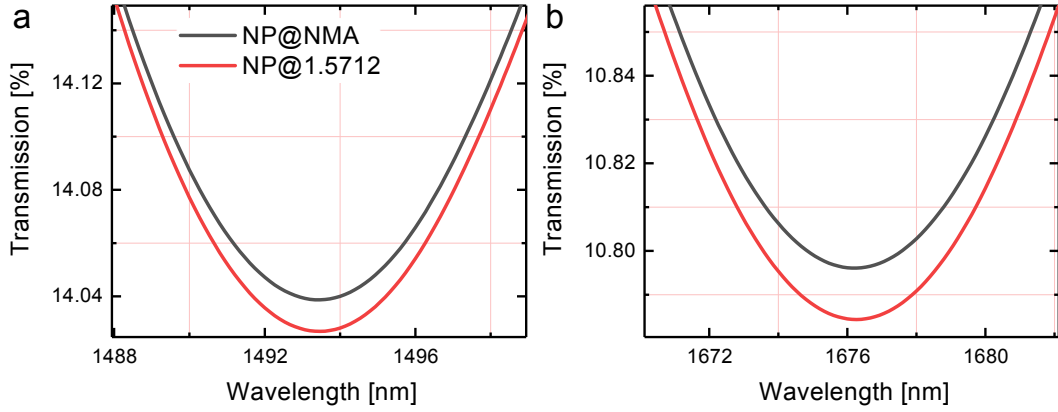
Figure 4.12: A closer look at the transmission spectra of metasurfaces covered by the NMA layer (black curves) and immersion oil with $n_{av} = 1.5712$ (red curves) of the same thickness $t = 35$ nm. The NPs lengths L were chosen to provide for the coincidence of the collective LSPRs of the metasurfaces with the NMA overtone transitions: $L = 196$ nm for N-H band (a), and $L = 234$ nm for C-H band (b).

For the sensing purposes, the difference between the DT maximum and minimum (hereinafter referred to as '*DT contrast*') is of paramount importance, since it is the variation magnitude that determines the metasurface sensitivity. Then, the enhancement factor (EF) can be expressed as $EF = \frac{DT}{DT_0}$, where DT_0 is the DT value of the same analyte film placed on a bare substrate without gold metasurface. DT_0 values were obtained via elementary calculations (described in Section 2.4) and presented in Figure 4.13a for a range of analyte film thicknesses up to t = 100 nm. Figure 4.13b shows the DT contrasts for the arrays of nanoantennas of different lengths presented in Figure 4.11. It was noticed that the EF provided by metasurface utilization depends on the nanoantennas lengths. Hence, the optimization procedure is essential to maximize the EF for the particular overtone transition.
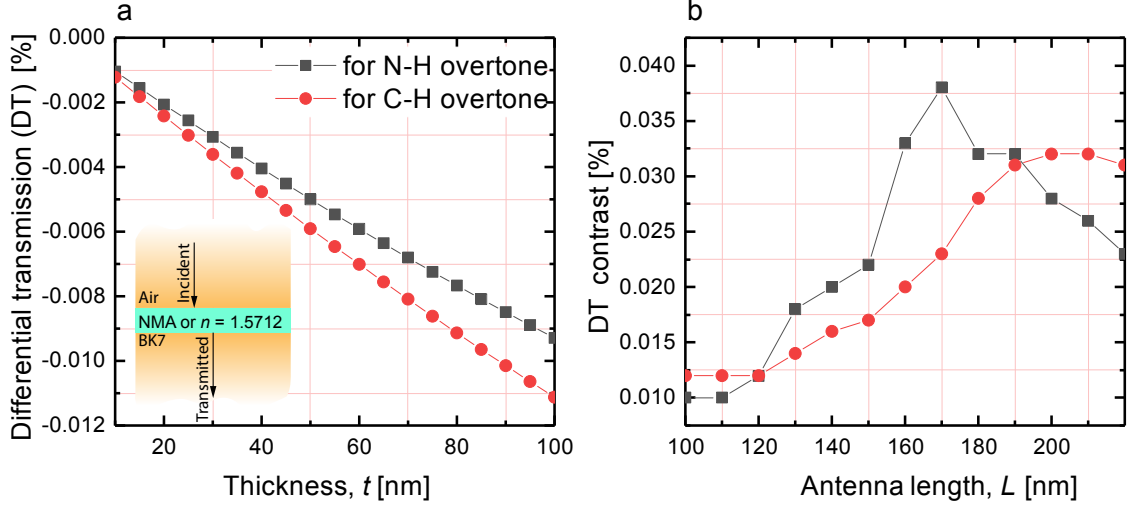
Figure 4.13: **(a)** DT of NMA films on a bare substrate as function of the film thickness. The insert shows the structure of the parallel films used for the calculation under the normal incidence illumination. **(b)** The DT contrast estimated from the data presented in Figure 4.11 as a function of the nanoantenna length.

4.5.3 Enhancement factors of the optimized metasurfaces

In this section, the dependence of the DT enhancement factor with varied the lattice periods was discussed. While exploring the metasurface configuration optimized for the enhancement of the particular overtone transition, the nanoantenna lengths as well as both periods of the square lattice were varied. To reach the maximum field enhancement, the nanoantenna length that maximizes the collective polarizability at the desired wavelength was found for a number of lattice periods combinations. At the final step, the enhancement factors were calculated as presented in Figures 4.14 and 4.16. The analyte film thickness was set to 35 nm. This choice provides reasonable utilization of the near-field enhancement region. Indeed, according to Figure 4.10d, the maximum field enhancement is achieved at the surface of the nanoparticle and rapidly drops with the distance. Hence, from the perspective of the sensitivity enhancement, the analyte layers should not be thicker than 35 nm.
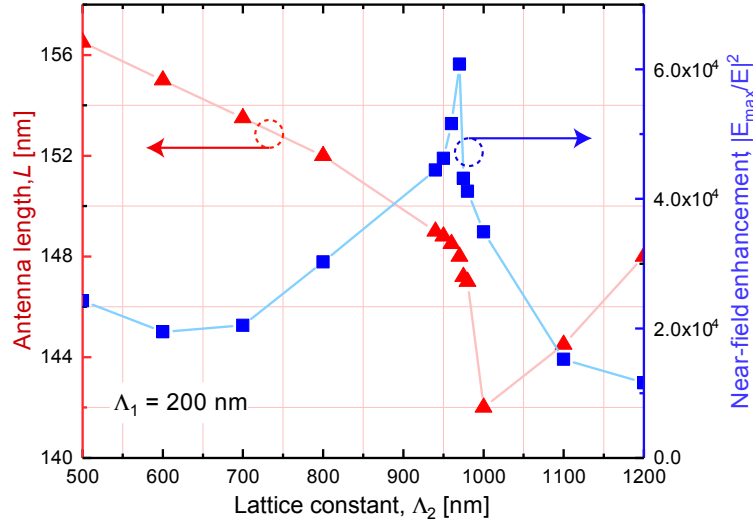
Figure 4.14: Variation of the local field enhancement (blue curve) and the resonant nanoantenna length L (red curve) with the lattice period Λ_2 when the other lattice period is fixed at Λ_1 = 200 and ensuring constant collective LSPR band at λ = 1494 nm. The analyte film thickness t = 35 nm.

The red curve in Figure 4.14 shows the variation of the resonant nanoantenna length L with the lattice period Λ_2 when the other lattice period is fixed at Λ_1 = 200 nm and ensuring constant collective LSPR band at λ = 1494 nm. In agreement with the numerical results presented in Figure 4.14, L reaches a minimum near the wavelength corresponding to the Rayleigh anomaly at about 1000 nm. Almost simultaneously, at Λ_2 = 970 nm the near-field enhancement reaches its maximum (blue curve in Figure 4.14). Qualitatively, this behavior may be understood as follows: if one can assume that $\Lambda_2 > 996$ nm, then the first diffraction order of the radiation with the wavelength λ of 1494 nm (in vacuum) can propagate in the substrate with refractive index n_{sub} = 1.5. However, when $\Lambda_2 < 996$ nm, all diffraction orders becomes evanescent since $\Lambda_2 ¡ \lambda n_{sub}$. The evanescent wave decays fast from the boundary. In addition, it carries no energy. Therefore, its amplitude may exceed the incident wave amplitude without violation of energy conservation law. This is the origin of the lattice contribution to the local field enhancement.

Subsequently, Λ_2 at 970 nm was fixed and adjusted the second lattice period Λ_1 varying it from 50 to 220 nm, as it is illustrated in Figure 4.16 (blue curve). Simultaneously with Λ_1 variation, the NPs length L was adjusted to keep the collective LSPR of the metasurface at the resonance with the overtone transition in NMA, as it is illustrated in Figure 4.15. The absolute maximum was found at Λ_1 = 75 nm that corresponds to the field enhancement of 2×10^8.
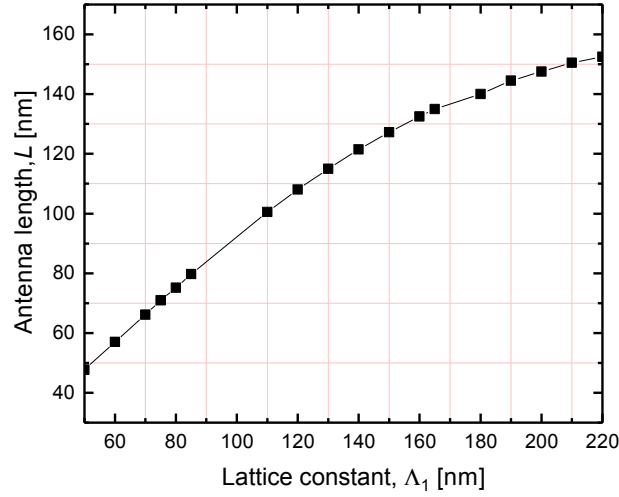
Figure 4.15: Dependence of the resonance antenna length L on the longitudinal lattice period Λ_1 at the fixed Λ_2 = 970 nm.

Finally, it was checked that this metasurface design also provides the largest enhancement factor for sensing application which reaches an unprecedented value of 22.5 (red curve, Figure 4.16). To double-check that the absolute maximum of the DT enhancement factor is evaluated, the Λ_2 was varied again around the value of 970 nm. The inset of Figure 4.16 supports the conclusion that the absolute maximum is found.
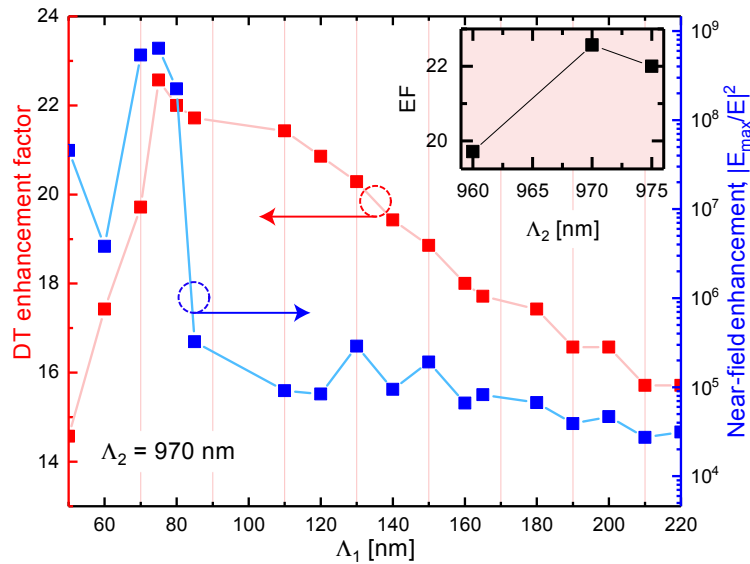
Figure 4.16: Variation of the local field enhancement (blue curve) and the DT enhancement factor (EF) with the lattice period Λ_1 when the other lattice period is fixed at Λ_2 = 970 nm. The inset shows EF against the lattice constant Λ_2 at fixed Λ_1 = 75 nm. Additionally, the direction and color of the horizontal arrow indicate the corresponding axis for the red and blue curves.

4.6　Summary

In the first part, the *differential extinction* of forbidden molecular overtone transitions coupled to the localized surface plasmons was explored for the first time. It was shown that the differential extinction provides the SENIRA with two orders of magnitude enhancement. The nontrivial consequence of the simulations is that the enhanced absorption in the analyte is accompanied by the reduced absorption in the gold nanorods that overruns the absorption enhancement of the analyte. In the second part, I numerically demonstrated the sensing capabilities of the rectangular lattice of gold nanoparallelepipeds on a transparent substrate while tuned on the specific transitions in the near-infrared. The shape of the metasurface unit-cells was adjusted to be readily manufacturable by electron beam lithography or focused ion beam milling. To optimize the metasurface for a particular overtone transition registration, I varied the periods of the lattice and the elements lengths simultaneously.

I found that one of the optimized lattice periods is very close to that corresponding to the Rayleigh anomaly. As I am trying to anticipate the response of the actual applications, I do not place the analyte within the near-field enhancement factor maxima, but rather, as a 35 nm thick homogeneous film covering the whole metasurface. Because of that, a relatively small proportion of the analyte experiences the largest field enhancement. Consequently, the structure optimized for the sensing of N-H overtone transition at 1494 nm has shown the differential transmission enhancement factor of 22.5. This rather large enhancement may be explained by the concerted action of the LSPR, the lattice resonance and the high surface density of gold nanoparticles on the substrate. Thus, the way to optimize the gold metasurface for sensing the weak overtone transitions in the near-infrared have been demonstrated. This approach may be extended for sensitive registration of other functional group overtones in the near-infrared by tailoring the lattice periods and the aspect ratios of a metasurface unit-cells.

Thus, the gold metasurface may be employed to identify the spectral position of the analyte absorption bands even when the available amount of analyte is very small. The reported results allow bringing new insight to enhanced light-matter interaction field with overtone transition as well as improve the limit of detection of conventional label-free sensors operating in the near-infrared range.

To conclude, the rapid spectral variation of the refractive index in the spectral range of the analyte anomalous dispersion was leveraged. As the anomalous dispersion is associated

with its overtone absorption band, by measuring the differential transmission of a metasurface tuned to the specified spectral range the tiny amount of an analyte may be detected. In practice, several arrays of nanoparallelepipeds tuned to different spectral ranges may be fabricated on a single chip. In this case, the combination of the responses of all arrays in the chip will lead to the recognition and characterization of the analyte.

5   Metal nanoparticles for intracellular uptake monitoring

As mentioned in Chapter 1, nanoparticles have a number of unique optical, electrical, and magnetic properties that have been actively used in various applications in recent decades [130]. The use of metallic nanoparticles allows for new possibilities in the study of intracellular processes. Nanoparticles fabricated by laser ablation in a liquid have a higher sensitivity compared to nanoparticles chemically prepared with stabilizers due to the absence of stabilizer molecules. Eliminating stabilizer molecules makes it possible to obtain information near the environment of a nanoparticle in the process of cellular uptake. To realize these opportunities, the fabrication of stable aqueous solutions of metal nanoparticles with extremely narrow plasmon absorption bands plays a fundamental role.

5.1   Experimental results

Based on the constructed experimental setup shown in Figure 2.1, SNPs in distilled water were synthesized. The silver target was ablated by a pulsed laser with different exposure times. Our goal was to find the optimum exposure time leading to the formation of a colloidal particle solution with a large extinction and narrow plasmonic absorption band. The measured extinction spectra of colloidal SNPs possess pronounced plasmon bands in the spectral range from 300 to 600 nm as shown in Figure 5.1a. The exposure time was converted to the number of pulses (N) at a known repetition rate. In Figure 5.1b, the dependence of the maximum optical density (OD) and full width at half maximum (FWHM) against N was plotted. It was found that when OD has a maximum when N reaches 6000 pulses, with a sharp drop in the OD for $N > 6000$. At N = 10800 pulses, the OD is halved. Since SNPs are formed only in a certain volume, the liquid can repeatedly be subjected to laser radiation due to convective

motion. This causes weakening of the laser radiation power in the target region, decreasing the efficiency, and changing the particle size distribution during laser irradiation.
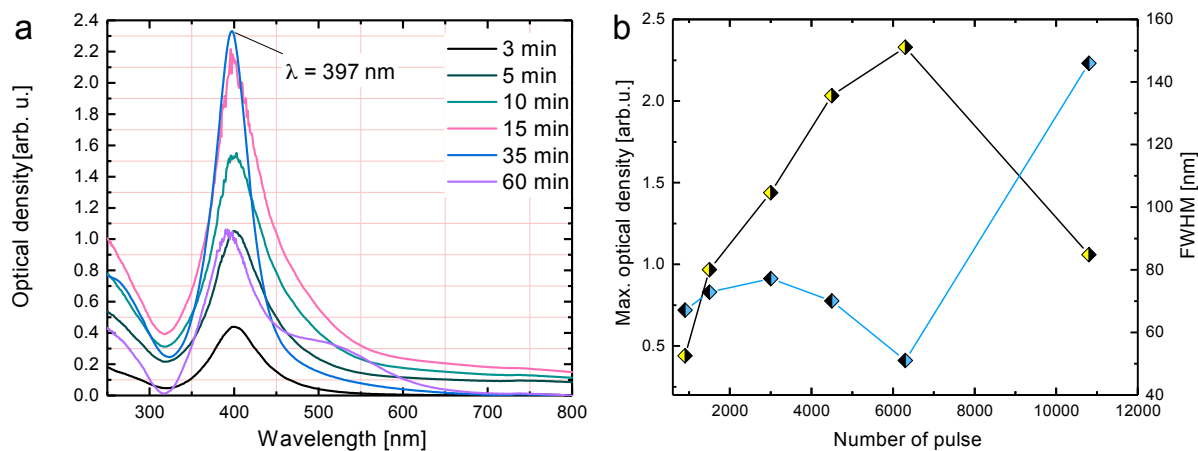
Figure 5.1: (a) Extinction spectra of the colloidal SNPs prepared during the exposure time and **(b)** the influence of the number of pulses on the plasmon properties of SNPs.

The plasmon resonance in the optical density spectrum of SNPs corresponds to the wavelength of 397 nm. The laser radiation from the second harmonic at wavelength of 532 nm is absorbed by SNPs, which then leads to the appearance of a pronounced additional peak around 530 nm as exhibited in Figure 5.1a. One of the most important requirements for sensors that measure fine changes in the analyte's refractive index is the width of the NP plasmon band. The narrower the plasmon band the higher sensor sensitivity is. Laser ablation of a silver target for 35 minutes leads to the formation of SNPs with the narrow plasmon band centered at 397 nm, which is favorable for endocytosis.

After fabrication, the nanoparticles with SEM and AFM techniques were characterized. Based on the SEM (Figure 5.2a) micrographs, the size distribution of nanoparticles were estimated. The histogram in Figure 5.2b shows that the colloidal solution contains fabricated nanoparticles with a broad size distribution. The fabricated ensembles of SNPs were characterized by uniformity of shape being close to spherical. The average diameter of SNPs is 24.6 nm.
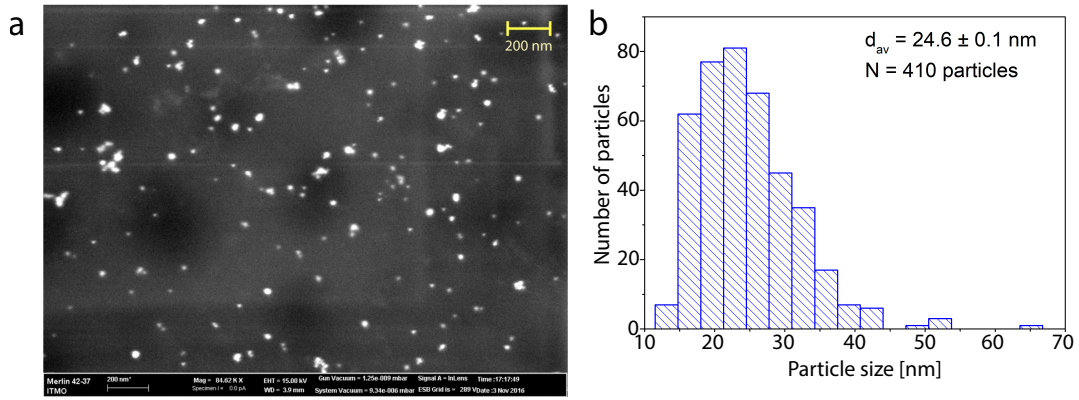
Figure 5.2: (a) Scanning electron microscope image of silver nanoparticles on the carbon grid. The scale bar is 200 nm. (b) The size distribution of silver nanoparticles d_{av} = 24.6 nm.

The dried SNPs on a quartz substrate were imaged using AFM, as shown in Figure 5.3 a, b. According to AFM data (Figure 5.3c), the particle height for a specific region in AFM image varies from h=10 to h=60 nm, taking into account the shape of the AFM probe, while their dimensions in the direction parallel to the substrate plane are from 10 to 50 nm.
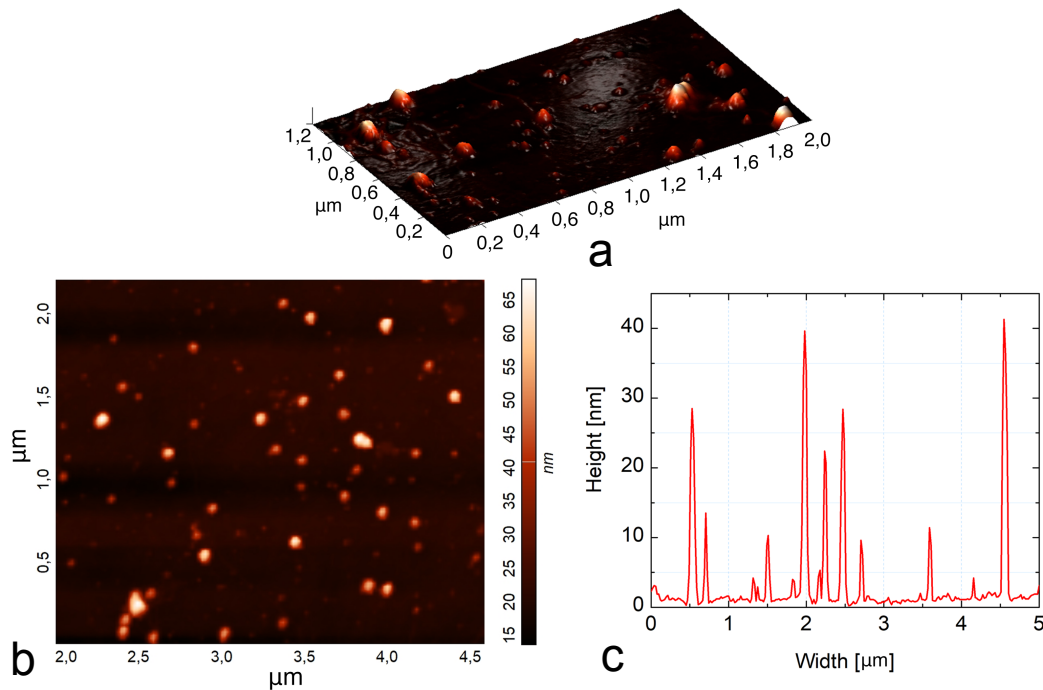
Figure 5.3: (a) 3D atomic force microscopy image of silver nanoparticles dried on the quartz substrate obtained in the tapping mode regime; (b) atomic force microscopy image (the top view) with size scale bar from 15 to 65 nm; (c) the cross-section profile of fabricated silver nanoparticles; the height of nanoparticles varied from 10 to 60 nm.

Particular attention was paid to the refractive index of the bovine serum albumin (BSA)

molecules, which mainly depends on the concentration of BSA molecules in solution. Based on the method described in Ref. [131], a stock solution was prepared with the concentration of 0.3 mg/ml , resulting in a refractive index close to 1.4 [132]. Figure 5.4 shows the extinction spectra of colloidal SNPs in water with and without BSA molecules. A comparative analysis of the data showed that the absorption bands of colloidal solutions of SNPs with BSA are shifted with the respect to the absorption bands of bare SNPs in water. The SNPs extinction spectra maximum shifted by 13 nm after the SNPs were introduced into the BSA environment.
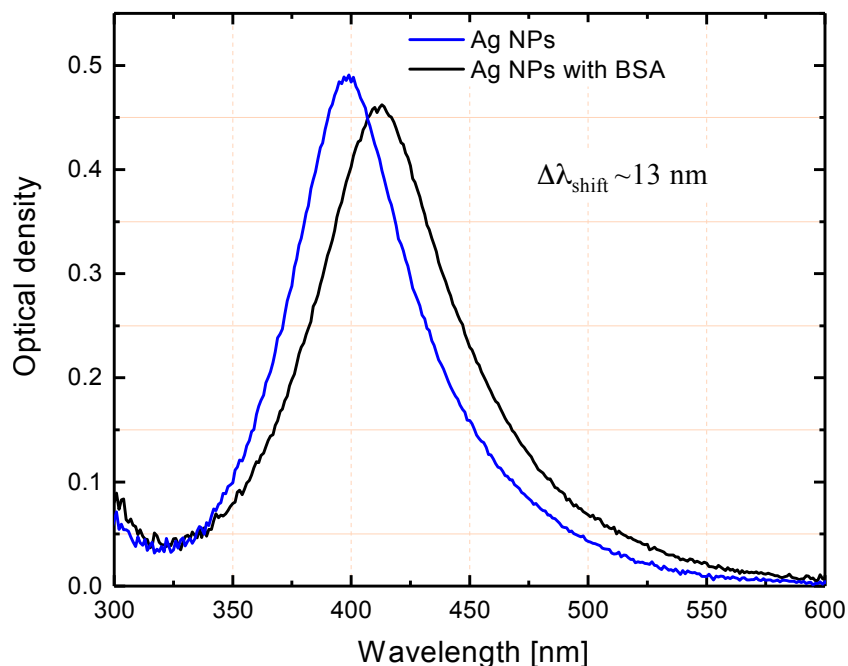
Figure 5.4: Extinction spectra of a colloidal solution of SNPs in water and BSA.

5.2 Numerical calculation of silver nanoparticle traffic

The experimental results obtained in the previous section demonstrate the optical response (red-shift) of SNPs to the presence of a biological object, but they exclude intermediate states when the nanoparticles are embedded into the biological interface. It is well-known [130, 133] that the dipole plasmon band of a sphere corresponds to three degenerate eigenmodes that represent plasmon oscillations in three independent dimensions. When the sphere approaches a plane boundary between two media with different refractive indices, two eigenmodes that correspond to the oscillations parallel to the boundary remain degenerate, while the third relates to the dipole oscillation normal to the boundary shifts faster than two others. Thus, the three-fold degeneracy of the plasmon band of a sphere is partially lifted when the sphere

approaches the boundary. This conclusion holds for the spheres approaching the boundary from both sides. The dependence of eigenfrequencies on the distance to the boundary means that they have to coincide at a point where the three-fold degeneracy revived.

From this qualitative reasoning, it can be seen that in the course of nanoparticle penetration through the cell membrane, the plasmon degeneracy is lifted twice and revives once in the process of movement. To obtain the dependence of plasmon resonance splitting contrast on the particle position for various optical properties of the adjacent media, the plasmon resonance excitation in a spherical nanoparticle with polarization in the $-x$ (top excitation) and the $-z$ (side excitation) direction was examined.

As shown in Figure 5.5a a scheme of the numerical model in which both plasmon modes in the sphere (along x and z) can be excited by a plane-polarized wave. The wavevector direction is specified by k_x and k_z. It was assumed that the biological medium has the refractive index 1.4, according to Ref.[134, 135], and the biological medium (BM) as a sphere with the diameter of 200 nm was modeled numerically.
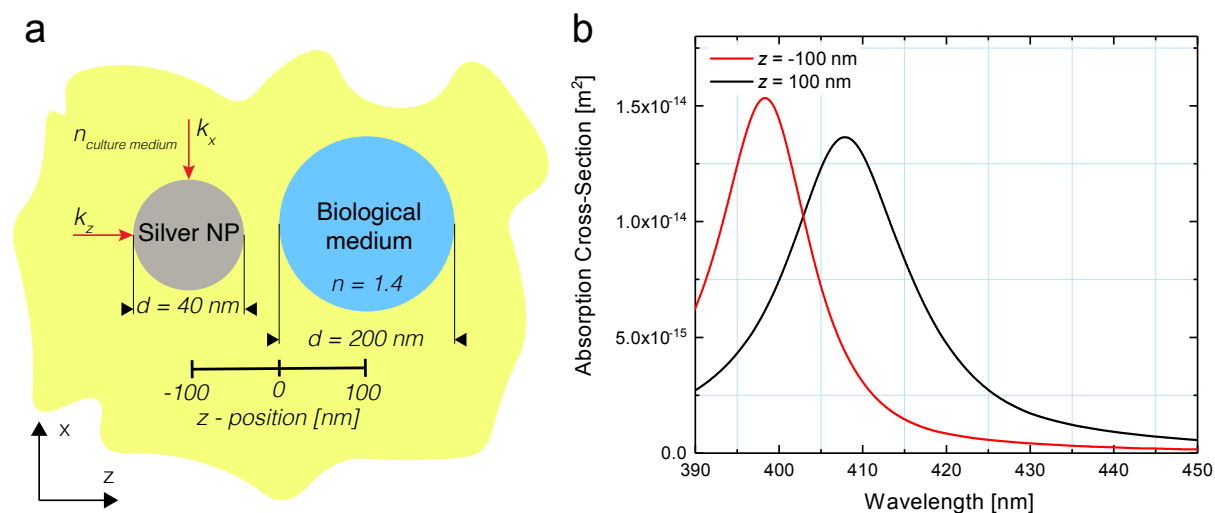
Figure 5.5: (a) The scheme of the numerical model, (b) the calculated absorption cross-section spectra of SNP for various values of z.

The cross-section spectra for a SNP with the diameter of 40 nm in a culture medium with refractive index $n_{\text{culture medium}}$ = 1.33 placed inside the biological medium (Figure 5.5 (b)) were calculated in the range of 350 - 450 nm. A culture medium is a medium for the cultivation of microorganisms such as macrophages. In Figure 5.5b, z = -100 nm corresponds to the case when the nanoparticle is far from the biological medium with n = 1.4, and for the opposite case z = 100 nm, the SNP is inside the sphere. It can be seen from the absorption cross-section

spectra that the embedding of SNP into homogeneous biological medium leads to the 9 nm red-shift.

The numerical results that demonstrate the plasmon band splitting are shown in Figure 5.6. This shows the nature of the resonant shift and splitting of the resonant wavelengths.
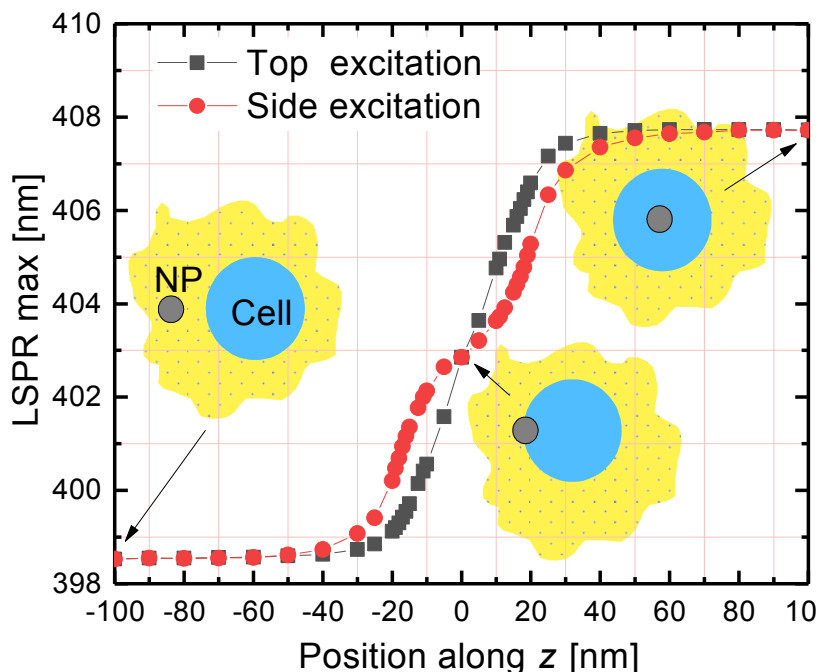
Figure 5.6: Splitting of resonance wavelengths of localized surface plasmons of SNP with the diameter of 40 nm in the process of their approaching and crossing the interface with two media with different refractive indices.

Additionally, there is a point corresponding to the degeneracy of the three modes, which manifests itself in the intersection of the curves in the graphs. The splitting starts when SNP approaches the boundary and reaches a maximum when a small part of the sphere is in the medium at z = -15 nm. At z > 0 nm, the splitting occurs again until it is in the center of the biological medium.

Despite the significant shift of LSPR achieved by penetration from a lower refractive index medium to a higher one, the real scenario is more complicated. It is well-known that cells contain the intercellular liquid, which in turn has an average refractive index around 1.37 [136]. Figure 5.7 shows the plasmon bands splitting of the nanoparticle approaching the cell, consisting of the membrane (thickness t= 5 nm and $n_{membrane} = 1.4$) and cellular liquid ($n_{cellular\ liquid}$ = 1.37). In fact, the behavior in Figure 5.7 is very similar to that in Figure 5.6, but the shift of the plasmon resonance band is slightly less. Nevertheless, considering the

membrane and intercellular liquid in the numerical calculation brings the results closer to a more realistic case of the NPs uptake process as a result of the endocytosis.
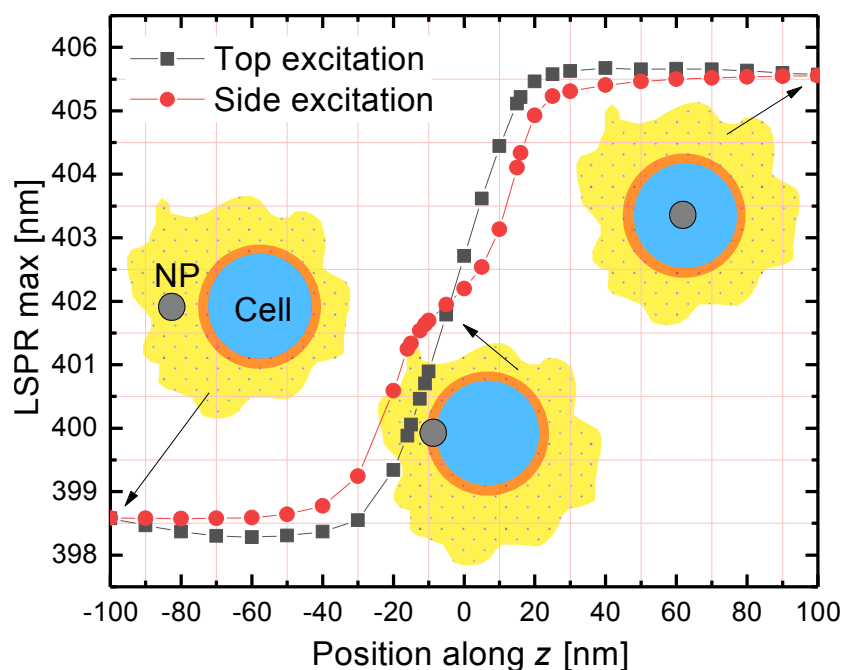
Figure 5.7: The plasmon resonance band splitting of SNP with the diameter of 40 nm during their approaching and crossing the interface with three media ($n_{\text{culture medium}}$ = 1.33, n_{membrane} = 1.4, and $n_{\text{cellular liquid}}$ = 1.37)

In order to evaluate the relative position of SNP with the highest splitting magnitude of plasmon resonance, the dependence of the splitting contrast on the z coordinate was plotted in Figure 5.8.

Even with a slight difference in the refractive indices of the culture medium, membrane, and intercellular liquid, the evidence of the plasmon resonance band splitting can be observed. In the experiments with cellular lines (e.g., macrophages), one can expect excitation of both eigenmodes. Thus, degeneracy lifting will manifest itself as an additional broadening of the plasmon band. The degeneracy revival leads to the non-monotonous behavior of the plasmon bandwidth: broadening is followed by narrowing, then broadening again, and final narrowing. Taking into account that the shifts themselves are at the limit of detection the awareness of the expected behavior of this additional parameter may be of crucial value for the interpretation of experimental results.
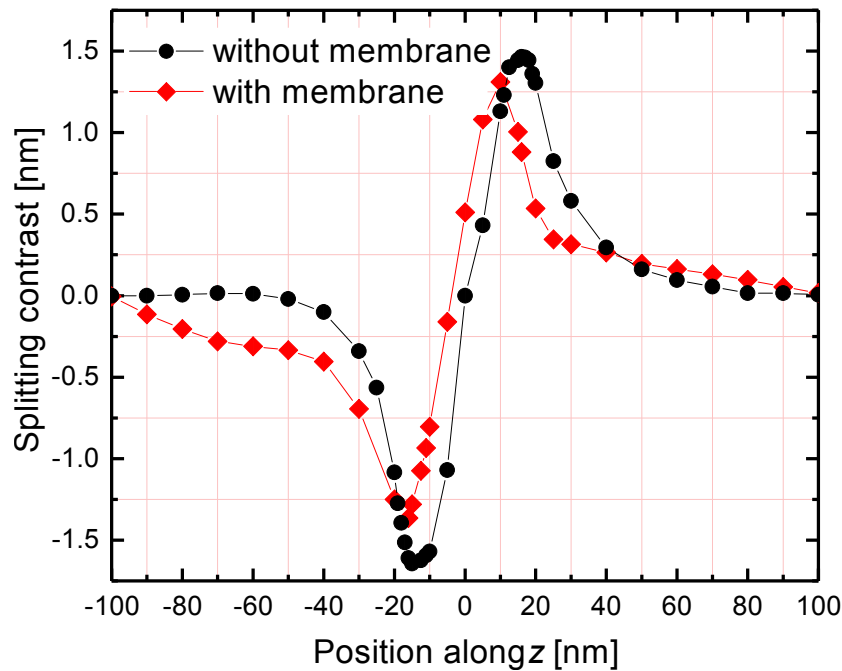
Figure 5.8: The plasmon resonance splitting contrast with 5 nm membrane (red curve) and without membrane (blue curve).

5.3   Summary

The possibility of using silver nanoparticles obtained in the form of the colloidal solution in distilled water by laser ablation of a metallic target have been explored. The silver nanoparticles with the dimensions of 20 to 50 nm without stabilizing agents, and stable for at least a month were fabricated. Due to the broad shape and size distributions of the obtained nanoparticles, the width of the plasmon band is larger than expected from the calculation pertinent to the monodisperse solutions. Despite that, the shift of the plasmon band maximum is measurable due to the refractive index change. To simulate the nanoparticle transition from subcutaneous water to the cellular membrane, the shift of the plasmon band maximum was measured when the nanoparticles were transferred from water with a refractive index of 1.33 to a bovine serum albumin solution with a refractive index of 1.4. In this case, the shift as large as 13 nm was observed. It was reasonable to proceed with numerical simulations of the plasmon position shifts in different situations relevant to endocytosis. The process involves a transition through the curved boundary between two media with different refractive indices: 1)transition through the thin film of a higher refractive index material representing the cell membrane, 2) transition of vesicle, which involves the nanoparticles surrounded by the membrane, is represented in

the numerical model by the core-shell structure. The results of simulations substantiate the feasibility of the proposed approach for endocytosis diagnostics by means of the far-field spectroscopy with noble metal nanoparticles.

6 Conclusion

This thesis investigates the application of plasmonic nanoparticles and their potential application towards label-free sensing.

In order to create an accessible method for producing nanoparticle ensembles with a specific plasmon resonance, I first performed theoretical optimization of the silver nanoparticle shape and size, such that their localized surface plasmon band are turned for the best overlap with the wide-band emission of chemiluminophores. These nanoparticles were fabricated using physical vapor deposition. In addition, experiments using an inert spacer layer and a silver film have shown that the catalytic action of the metal surface is of minor importance. I have designed plasmonic nanoparticles with a dielectric material substrate, which makes it possible to create a new generation of chemiluminescence-based devices. I showed 1.6-fold enhancement of chemiluminescence intensity upon direct contact of the reagents with a silver film with plasmon resonances in the chemiluminescence bands.

The next step would be to amplify the weak overtone transitions that reside in the near-infrared, for which I employed the resonant coupling between plasmonic nanoantennas and molecular vibrational excitations. By selecting of the suitable aspect ratio of the gold nanoantenna, their plasmon band may be brought in line with the expected position of the sought molecular vibration. I explored the differential extinction of forbidden molecular overtone transitions coupled to the localized surface plasmons. I showed a non-trivial interplay between the molecular absorption enhancement and suppression of plasmonic absorption in a coupled system in differential extinction spectra. Then I studied SENIRA in the framework of molecular overtones sensing using the gold metasurface. As a result of the combination of localized surface plasmon resonance in prolonged nanoparticles and Rayleigh anomaly of the lattice, the N-H overtone transition has been enhanced 22.5 times.

In order to use these plasmonic nanoparticles in biological sensing applications, I studied the influence of the surrounding media on the optical response of the silver nanoparticles. I

used a endocytosis model to study numerically the penetration of a nanoparticle through a thin cell membrane. It was shown that when the silver nanoparticle approaches the boundary of the cell membrane, plasmon degeneracy is partially lifted as can be seen in course of the plasmon band splitting. For the experimental verification, I fabricated silver nanoparticles without a stabilizing ligand through laser ablation. The fabricated nanoparticles were surrounded by a thin shell in order to demonstrate a shift in the LSPR. This thin shell is analogous to the thin shell membrane produced by endocytosis in the simulations, hence I conclude that endocytosis also produces a shift in the LSPR.

Bibliography

[1] Stefan A. Maier. Plasmonics: Fundamentals and Applications". Springer Science & Business Media, 2007.

[2] K Lance Kelly, Eduardo Coronado, Lin Lin Zhao, and George C Schatz. The optical properties of metal nanoparticles: the influence of size, shape, and dielectric environment, 2003.

[3] P. B. Johnson and R. W. Christy. Optical constants of the noble metals. Physical Review B, 6(12):4370–4379, 1972.

[4] D V Sotnikov, A V Zherdev, and B B Dzantiev. Detection of intermolecular interactions based on surface plasmon resonance registration. Biochemistry (Moscow), 80(13):1820–1832, 2015.

[5] Vasyl G Kravets, Andrei V Kabashin, William L Barnes, and Alexander N Grigorenko. Plasmonic surface lattice resonances: a review of properties and applications. Chemical reviews, 118(12):5912–5951, 2018.

[6] Mara Mirasoli, Massimo Guardigli, and Aldo Roda. Chemiluminescence in Biomedicine. In Applied Photochemistry, pages 427–458. Springer, 2016.

[7] Shahed Behzadi, Vahid Serpooshan, Wei Tao, Majd A Hamaly, Mahmoud Y Alkawareek, Erik C Dreaden, Dennis Brown, Alaaldin M Alkilany, Omid C Farokhzad, and Morteza Mahmoudi. Cellular uptake of nanoparticles: journey inside the cell. Chemical Society Reviews, 46(14):4218–4244, 2017.

[8] Vasily Klimov. Nanoplasmonics. CRC press, 2014.

[9] Stefan Alexander Maier. Plasmonics: fundamentals and applications. Springer Science & Business Media, 2007.

[10] Chris D Geddes. Metal-enhanced fluorescence. John Wiley & Sons, 2010.

[11] Z Starowicz, R Wojnarowska-Nowak, P Ozga, and EM Sheregii. The tuning of the plasmon resonance of the metal nanoparticles in terms of the sers effect. Colloid and polymer science, 296(6):1029–1037, 2018.

[12] Alina Karabchevsky, Aviad Katiyi, Muhammad Imran Mustafa Bin Abdul Khudus, and Alexey V Kavokin. Tuning the near-infrared absorption of aromatic amines on tapered fibers sculptured with gold nanoparticles. ACS Photonics, 5(6):2200–2207, 2018.

[13] J C Maxwell Garnett. VII. Colours in metal glasses, in metallic films, and in metallic solutions.—II. Phil. Trans. R. Soc. Lond. A, 205(387-401):237–288, 1906.

[14] Gustav Mie. Beiträge zur Optik trüber Medien, speziell kolloidaler Metallösungen. Annalen der physik, 330(3):377–445, 1908.

[15] Craig F Bohren and Donald R Huffman. Absorption and scattering of light by small particles. John Wiley & Sons, 2008.

[16] Cecilia Noguez. Surface plasmons on metal nanoparticles: The influence of shape and physical environment. Journal of Physical Chemistry C, 111(10):3606–3619, 2007.

[17] NV Voshchinnikov and VG Farafonov. Optical properties of spheroidal particles. Astrophysics and space science, 204(1):19–86, 1993.

[18] Edward M Purcell and Carlton R Pennypacker. Scattering and absorption of light by nonspherical dielectric grains. The Astrophysical Journal, 186:705–714, 1973.

[19] Bruce T Draine and Piotr J Flatau. Discrete-dipole approximation for scattering calculations. Josa a, 11(4):1491–1499, 1994.

[20] George C Schatz. Electrodynamics of nonspherical noble metal nanoparticles and nanoparticle aggregates. Journal of Molecular Structure: THEOCHEM, 573(1-3):73–80, 2001.

[21] Peter Nordlander and Emil Prodan. Plasmon hybridization in nanoparticles near metallic surfaces. Nano Letters, 4(11):2209–2213, 2004.

[22] Alastair D Humphrey and William L Barnes. Plasmonic surface lattice resonances on arrays of different lattice symmetry. Physical Review B, 90(7):075404, 2014.

[23] Mihai Stafe, Aurelian Marcu, and Niculae N Puscas. Pulsed laser ablation of solids: basics, theory and applications, volume 53. Springer Science & Business Media, 2013.

[24] Hongkun Huang, Jiancheng Lai, Jian Lu, and Zhenhua Li. Pulsed laser ablation of bulk target and particle products in liquid for nanomaterial fabrication. AIP Advances, 9(1):015307, 2019.

[25] Mengtao Sun and Hongxing Xu. A novel application of plasmonics: plasmon-driven surface-catalyzed reactions. Small, 8(18):2777–2786, 2012.

[26] Jianxun Liu, Huilin He, Dong Xiao, Shengtao Yin, Wei Ji, Shouzhen Jiang, Dan Luo, Bing Wang, and Yanjun Liu. Recent advances of plasmonic nanoparticles and their applications. Materials, 11(10):1833, 2018.

[27] Timothy J Davis, Daniel E Gómez, and Ann Roberts. Plasmonic circuits for manipulating optical information. Nanophotonics, 6(3):543–559, 2016.

[28] NC Panoiu, WEI Sha, DY Lei, and GC Li. Nonlinear optics in plasmonic nanostructures. Journal of Optics, 20(8):083001, 2018.

[29] Nikolai G Khlebtsov and Lev A Dykman. Optical properties and biomedical applications of plasmonic nanoparticles. Journal of Quantitative Spectroscopy and Radiative Transfer, 111(1):1–35, 2010.

[30] Bhavya Sharma, Renee R Frontiera, Anne-Isabelle Henry, Emilie Ringe, and Richard P Van Duyne. Sers: Materials, applications, and the future. Materials today, 15(1-2):16–25, 2012.

[31] Chris D Geddes, Haishi Cao, Ignacy Gryczynski, Zygmunt Gryczynski, Jiyu Fang, and Joseph R Lakowicz. Metal-enhanced fluorescence (mef) due to silver colloids on a planar surface: Potential applications of indocyanine green to in vivo imaging. The Journal of Physical Chemistry A, 107(18):3443–3449, 2003.

[32] Antonio M Brito-Silva, Luiz A Gómez, Cid B De Araújo, and André Galembeck. Laser ablated silver nanoparticles with nearly the same size in different carrier media. Journal of Nanomaterials, 2010, 2010.

[33] Vincenzo Amendola, Stefano Polizzi, and Moreno Meneghetti. Free silver nanoparticles synthesized by laser ablation in organic solvents and their easy functionalization. Langmuir, 23(12):6766–6770, 2007.

[34] SM Arakelyan, VP Veiko, SV Kutrovskaya, AO Kucherik, AV Osipov, TA Vartanyan, and TE Itina. Reliable and well-controlled synthesis of noble metal nanoparticles by continuous wave laser ablation in different liquids for deposition of thin films with variable optical properties. Journal of Nanoparticle Research, 18(6):155, 2016.

[35] Saeed Mozaffari, Wenhui Li, Coogan Thompson, Sergei Ivanov, Soenke Seifert, Byeongdu Lee, Libor Kovarik, and Ayman M Karim. Colloidal nanoparticle size control: experimental and kinetic modeling investigation of the ligand–metal binding role in controlling the nucleation and growth kinetics. Nanoscale, 9(36):13772–13785, 2017.

[36] Alina Karabchevsky, Ali Mosayyebi, and Alexey V Kavokin. Tuning the chemiluminescence of a luminol flow using plasmonic nanoparticles. Light: Science & Applications, 5(11):e16164, 2016.

[37] Filippo Barni, Simon W. Lewis, Andrea Berti, Gordon M. Miskelly, and Giampietro Lago. Forensic application of the luminol reaction as a presumptive test for latent blood detection. Talanta, 72(3):896–913, 2007.

[38] Shiro Yamashoji. Determination of viable mammalian cells by luminol chemiluminescence using microperoxidase. Analytical Biochemistry, 386(1):119–120, 2009.

[39] Mortaza Iranifam. Chemiluminescence reactions enhanced by silver nanoparticles and silver alloy nanoparticles: Applications in analytical chemistry. TrAC - Trends in Analytical Chemistry, 82:126–142, 2016.

[40] Ronit Freeman, Xiaoqing Liu, and Itamar Willner. Chemiluminescent and chemiluminescence resonance energy transfer (CRET) detection of DNA, metal ions,

and aptamer-substrate complexes using hemin/G-quadruplexes and CdSe/ZnS quantum dots. Journal of the American Chemical Society, 133(30):11597–11604, 2011.

[41] Lori L. Klopf and Timothy A. Nieman. Effect of Iron(II), Cobalt(II), Copper(II), and Manganese(II) on the Chemiluminescence of Luminol in the Absence of Hydrogen Peroxide. Analytical Chemistry, 55(7):1080–1083, 1983.

[42] Liu Wei, Zhang Zhujun, and Yang Liu. Chemiluminescence microfluidic chip fabricated in PMMA for determination of benzoyl peroxide in flour. Food Chemistry, 95(4):693–698, 2006.

[43] Ana Rubina Perestrelo, Ana C.P. Águas, Alberto Rainer, and Giancarlo Forte. Microfluidic organ/body-on-a-chip devices at the convergence of biology and microengineering. Sensors (Switzerland), 15(12):31142–31170, 2015.

[44] Pedro M Valencia, Omid C Farokhzad, Rohit Karnik, and Robert Langer. Microfluidic technologies for accelerating the clinical translation of nanoparticles. Nature nanotechnology, 7(10):623, 2012.

[45] Aziz Aziz, Chunyang Geng, Mengjie Fu, Xiaohui Yu, Kairong Qin, and Bo Liu. The Role of Microfluidics for Organ on Chip Simulations. Bioengineering, 4(2):39, 2017.

[46] Iulia M. Lazar, Phichet Trisiripisal, and Hetal A. Sarvaiya. Microfluidic liquid chromatography system for proteomic applications and biomarker screening. Analytical Chemistry, 78(15):5513–5524, 2006.

[47] Jing Yu, Jing Zhou, Alex Sutherland, Wei Wei, Young Shik Shin, Min Xue, and James R Heath. Microfluidics-based single-cell functional proteomics for fundamental and applied biomedical applications. Annual review of analytical chemistry, 7:275–295, 2014.

[48] Ana Valero, Janine Nicole Post, Jan William van Nieuwkasteele, Paulus Martinus ter Braak, W Kruijer, and Albert van den Berg. Gene transfer and protein dynamics in stem cells using single cell electroporation in a microfluidic device. Lab on a Chip, 8(1):62–67, 2008.

[49] Matthew R. Bennett and Jeff Hasty. Microfluidic devices for measuring gene network dynamics in single cells. Nature Reviews Genetics, 10(9):628–638, 2009.

[50] Kadir Aslan and Chris D. Geddes. Surface plasmon coupled chemiluminescence from zinc substrates: Directional chemiluminescence. Applied Physics Letters, 94(7):73104, 2009.

[51] Kadir Aslan and Chris D. Geddes. Metal-enhanced chemiluminescence: Advanced chemiluminescence concepts for the 21st century. Chemical Society Reviews, 38(9):2556–2564, 2009.

[52] Alina Karabchevsky. Microspot sensing based on surface-enhanced fluorescence from nanosculptured thin films. Journal of Nanophotonics, 6(1):061508, 2012.

[53] I Abdulhalim, Alina Karabchevsky, Christian Patzig, Bernd Rauschenbach, Bodo Fuhrmann, Evgeni Eltzov, Robert Marks, Jian Xu, Fan Zhang, and Akhlesh Lakhtakia. Surface-enhanced fluorescence from metal sculptured thin films with application to biosensing in water. Applied Physics Letters, 94(6):63106, 2009.

[54] J. LEE and H. H. SELIGER. Quantum Yields of the Luminol Chemiluminescence Reaction in Aqueous and Aprotic Solvents. Photochemistry and Photobiology, 15(2):227–237, 1972.

[55] Ryan Fobel, Andrea E Kirby, Alphonsus H C Ng, Ramin R Farnood, and Aaron R Wheeler. Paper microfluidics goes digital. Advanced materials, 26(18):2838–2843, 2014.

[56] Meigui Ou, Guowei Lu, Hong Shen, Armel Descamps, Christophe André Marquette, Loïc Jacques Blum, Gilles Ledoux, Stéphane Roux, Olivier Tillement, Bolin Cheng, and Pascal Perriat. Catalytic performance of nanoscale-corrugated gold and silver films for surface-enhanced chemiluminescence. Advanced Functional Materials, 17(12):1903–1909, 2007.

[57] Alina Karabchevsky, Olga Krasnykov, Mark Auslender, Benny Hadad, Adi Goldner, and Ibrahim Abdulhalim. Theoretical and experimental investigation of enhanced transmission through periodic metal nanoslits for sensing in water environment. Plasmonics, 4(4):281–292, 2009.

[58] Alina Karabchevsky. Dual-surface plasmon excitation with thin metallic nanoslits. Journal of Nanophotonics, 5(1):051821, 2011.

[59] Jacob B. Khurgin, Greg Sun, and Richard A. Soref. Enhancement of luminescence efficiency using surface plasmon polaritons: figures of merit. Journal of the Optical Society of America B, 24(8):1968, 2007.

[60] Tadesse Haile Fereja, Ariaya Hymete, and Thirumurugan Gunasekaran. A recent review on chemiluminescence reaction, principle and application on pharmaceutical analysis. Isrn Spectroscopy, 2013, 2013.

[61] Jeong-Eun Park, Jiyeon Kim, and Jwa-Min Nam. Emerging plasmonic nanostructures for controlling and enhancing photoluminescence. Chemical science, 8(7):4696–4704, 2017.

[62] Chris D Geddes. Surface Plasmon Enhanced, Coupled and Controlled Fluorescence. John Wiley & Sons, 2017.

[63] Peter W Atkins and Ronald S Friedman. Molecular quantum mechanics. Oxford university press, 2011.

[64] Irene Canton and Giuseppe Battaglia. Endocytosis at the nanoscale. Chemical Society Reviews, 41(7):2718–2739, 2012.

[65] B Devika Chithrani, Arezou A Ghazani, and Warren CW Chan. Determining the size and shape dependence of gold nanoparticle uptake into mammalian cells. Nano letters, 6(4):662–668, 2006.

[66] KV Baryshnikova, MI Petrov, and TA Vartanyan. Plasmon nanoruler for monitoring of transient interactions. physica status solidi (RRL)–Rapid Research Letters, 9(12):711–715, 2015.

[67] TA Vartanyan, KV Baryshnikova, and SG Przhibel'skii. Metal nanosphere at an interface: revival of degeneracy of a dipole plasmon. In Journal of Physics: Conference Series, volume 673, page 012005. IOP Publishing, 2016.

[68] Tigran A Vartanyan, Nikita B Leonov, Valerii V Khromov, Sergey G Przhibelskii, Nikita A Toropov, and Elena N Kaliteevskaya. Granular metal films on the surfaces of transparent dielectric materials studied and modified via optical means. In Photonics and Micro-and Nano-structured Materials 2011, volume 8414, page 841404. International Society for Optics and Photonics, 2012.

[69] Nikita A. Toropov, Igor A. Gladskikh, Peter S. Parfenov, and Tigran A. Vartanyan. Fabrication and laser-assisted modification of the Ag particles ensembles supporting quadrupole plasmon oscillations. Optical and Quantum Electronics, 49(4):154, 2017.

[70] J Bosbach, C Hendrich, F Stietz, T Vartanyan, and F Träger. Ultrafast dephasing of surface plasmon excitation in silver nanoparticles: influence of particle size, shape, and chemical surrounding. Physical review letters, 89(25):257404, 2002.

[71] Schott glass database. https://www.schott.com/d/advanced_optics/ac85c64c-60a0-4113-a9df-23ee1be20428/1.17/schott-optical-glass-collection-datasheets-english-may-2019.pdf. May 2019.

[72] Aviad Katiyi and Alina Karabchevsky. Figure of merit of all-dielectric waveguide structures for absorption overtone spectroscopy. Journal of Lightwave Technology, 35(14):2902–2908, 2017.

[73] A. Karabchevsky and A. V. Kavokin. Giant absorption of light by molecular vibrations on a chip. Scientific Reports, 6:21201, 2016.

[74] Max Born and Emil Wolf. Principles of optics: electromagnetic theory of propagation, interference and diffraction of light. Elsevier, 2013.

[75] Mustafa H Chowdhury, Kadir Aslan, Stuart N Malyn, Joseph R Lakowicz, and Chris D Geddes. Metal-enhanced chemiluminescence: Radiating plasmons generated from chemically induced electronic excited states. Applied physics letters, 88(17):173104, 2006.

[76] Mustafa H Chowdhury, Kadir Aslan, Stuart N Malyn, Joseph R Lakowicz, and Chris D Geddes. Metal-enhanced chemiluminescence. Journal of fluorescence, 16(3):295–299, 2006.

[77] N B Leonov, I A Gladskikh, V A Polishchuk, and T A Vartanyan. Evolution of the optical properties and morphology of thin metal films during growth and annealing. Optics and Spectroscopy, 119(3):450–455, 2015.

[78] Micah Weisenberg, Yongxia Zhang, and Chris D Geddes. Metal-enhanced chemiluminescence from chromium, copper, nickel, and zinc nanodeposits: Evidence for

a second enhancement mechanism in metal-enhanced fluorescence. Applied Physics Letters, 97(13):133103, 2010.

[79] Mustafa H Chowdhury, Stuart N Malyn, Kadir Aslan, Joseph R Lakowicz, and Chris D Geddes. Multicolor directional surface plasmon-coupled chemiluminescence. The Journal of Physical Chemistry B, 110(45):22644–22651, 2006.

[80] Fan Jiang, Ping Li, Chen Zong, and Hua Yang. Surface-plasmon-coupled chemiluminescence amplification of silver nanoparticles modified immunosensor for high-throughput ultrasensitive detection of multiple mycotoxins. Analytica Chimica Acta, 2020.

[81] Vasanthan Devaraj, Hyuk Jeong, Chuntae Kim, Jong-Min Lee, and Jin-Woo Oh. Modifying plasmonic-field enhancement and resonance characteristics of spherical nanoparticles on metallic film: Effects of faceting spherical nanoparticle morphology. Coatings, 9(6):387, 2019.

[82] Mark W. Knight, Yanpeng Wu, J. Britt Lassiter, Peter Nordlander, and Naomi J. Halas. Substrates matter: influence of an adjacent dielectric on an individual plasmonic nanoparticle. Nano Letters, 9(5):2188–2192, 2009.

[83] Xiaotong Liu, Dabing Li, Xiaojuan Sun, Zhiming Li, Hang Song, Hong Jiang, and Yiren Chen. Tunable Dipole Surface Plasmon Resonances of Silver Nanoparticles by Cladding Dielectric Layers. Scientific Reports, 5:12555, 2015.

[84] Christopher M. Hindson, Paul S. Francis, Graeme R. Hanson, Jacqui L. Adcock, and Neil W. Barnett. Mechanism of permanganate chemiluminescence. Analytical Chemistry, 82(10):4174–4180, 2010.

[85] Yi He and Hua Cui. Fabrication of luminol and lucigenin bifunctionalized gold nnanoparticles/graphene oxide nanocomposites with dual-wavelength chemiluminescence. Journal of Physical Chemistry C, 116(23):12953–12957, 2012.

[86] Ji Zhao Guo and Hua Cui. Lucigenin chemiluminescence induced by noble metal nanoparticles in the presence of adsorbates. Journal of Physical Chemistry C, 111(33):12254–12259, 2007.

[87] Takeyoshi Okajima and Takeo Ohsaka. Chemiluminescence of lucigenin by electrogenerated superoxide ions in aqueous solutions. Luminescence, 18(1):49–57, 2003.

[88] Bo Liu, Yi He, Chunfeng Duan, Na Li, and Hua Cui. Platinum nanoparticle-catalyzed lucigenin–hydrazine chemiluminescence. Journal of Photochemistry and Photobiology A: Chemistry, 217(1):62–67, 2011.

[89] Xijuan Yu, Qiujin Wang, Xiangnan Liu, and Xiliang Luo. A sensitive chemiluminescence method for the determination of cysteine based on silver nanoclusters. Microchimica Acta, 179(3-4):323–328, 2012.

[90] Shifeng Li, Xiangzi Li, Yanqi Zhang, Fei Huang, Fenfen Wang, and Xianwen Wei. Enhanced chemiluminescence of the luminol-kIO4system by ZnS nanoparticles. Microchimica Acta, 167(1):103–108, 2009.

[91] Lijuan Wang and Yuhai Tang. Determination of dipyridamole using TCPO-H2O2chemiluminescence in the presence of silver nanoparticles. Luminescence, 26(6):703–709, 2011.

[92] JC Manifacier, J Gasiot, and JP Fillard. A simple method for the determination of the optical constants n, k and the thickness of a weakly absorbing thin film. Journal of Physics E: Scientific Instruments, 9(11):1002, 1976.

[93] Alina Karabchevsky, Olga Krasnykov, Mark Auslender, Benny Hadad, Adi Goldner, and Ibrahim Abdulhalim. Theoretical and experimental investigation of enhanced transmission through periodic metal nanoslits for sensing in water environment. Plasmonics, 4(4):281, 2009.

[94] A Karabchevsky, S Karabchevsky, and I Abdulhalim. Fast surface plasmon resonance imaging sensor using radon transform. Sensors and Actuators B: Chemical, 155(1):361–365, 2011.

[95] Alina Karabchevsky, Serge Karabchevsky, and Ibrahim Abdulhalim. Nanoprecision algorithm for surface plasmon resonance determination from images with low contrast for improved sensor resolution. Journal of Nanophotonics, 5(1):051813, 2011.

[96] Alina Karabchevsky, James S Wilkinson, and Michalis N Zervas. Transmittance and surface intensity in 3d composite plasmonic waveguides. Optics express, 23(11):14407–14423, 2015.

[97] Stanislav I Maslovski and Constantin R Simovski. Purcell factor and local intensity enhancement in surface-enhanced raman scattering. Nanophotonics, 2018.

[98] Constantin Simovski. Circuit model of plasmon-enhanced fluorescence. In Photonics, volume 2, pages 568–593. Multidisciplinary Digital Publishing Institute, 2015.

[99] Yakov Galutin, Eran Falek, and Alina Karabchevsky. Invisibility cloaking scheme by evanescent fields distortion on composite plasmonic waveguides with si nano-spacer. Scientific reports, 7(1):12076, 2017.

[100] Alina Karabchevsky and Atef Shalabney. Strong interaction of molecular vibrational overtones with near-guided surface plasmon polariton. In Optical Sensing and Detection IV, volume 9899, page 98991T. International Society for Optics and Photonics, 2016.

[101] Alina Karabchevsky, Aviad Katiyi, Muhammad Imran Mustafa Bin Abdul Khudus, and Alexey V. Kavokin. Tuning the Near-Infrared Absorption of Aromatic Amines on Tapered Fibers Sculptured with Gold Nanoparticles. ACS Photonics, 5(6):2200–2207, 2018.

[102] Wei Chuan Shih, Greggy M. Santos, Fusheng Zhao, Oussama Zenasni, and Md Masud Parvez Arnob. Simultaneous chemical and refractive index sensing in the 1-2.5 μm near-infrared wavelength range on nanoporous gold disks. Nano Letters, 16(7):4641–4647, 2016.

[103] Daler R. Dadadzhanov, Alina Karabchevsky, and Tigran Vartanyan. Vibrational overtones spectroscopy enabled by plasmonic nanoantennas. In Proceedings of SPIE - The International Society for Optical Engineering, volume 10722, page 85, 2018.

[104] Ming Li, Scott K Cushing, and Nianqiang Wu. Plasmon-enhanced optical sensors: a review. Analyst, 140(2):386–406, 2015.

[105] Nche T Fofang, Tae-Ho Park, Oara Neumann, Nikolay A Mirin, Peter Nordlander, and Naomi J Halas. Plexcitonic nanoparticles: plasmon-exciton coupling in nanoshell-J-aggregate complexes. Nano letters, 8(10):3481–3487, 2008.

[106] Daler R Dadadzhanov, Tigran A Vartanyan, and Alina Karabchevsky. Vibrational overtones spectroscopy enabled by plasmonic nanoantennas. In Plasmonics: Design, Materials, Fabrication, Characterization, and Applications XVI, volume 10722, page 107222E. International Society for Optics and Photonics, 2018.

[107] Daler R Dadadzhanov, Tigran A Vartanyan, and Alina Karabchevsky. Differential extinction of vibrational molecular overtone transitions with gold nanorods and its role in surface enhanced near-ir absorption (senira). Optics express, 27(21):29471–29478, 2019.

[108] Daler R Dadadzhanov, Tigran A Vartanyan, Antonina I Dadadzhanova, and Alina Karabchevsky. Surface-enhanced near-infrared absorption (senira) of ch and nh groups with gold nanoarray. In Quantum Sensing and Nano Electronics and Photonics XVII, volume 11288, page 1128816. International Society for Optics and Photonics, 2020.

[109] AD Humphrey and WL Barnes. Plasmonic surface lattice resonances in arrays of metallic nanoparticle dimers. Journal of Optics, 18(3):035005, 2016.

[110] VG Kravets, F Schedin, AV Kabashin, and AN Grigorenko. Sensitivity of collective plasmon modes of gold nanoresonators to local environment. Optics letters, 35(7):956–958, 2010.

[111] Baptiste Auguié and William L Barnes. Collective resonances in gold nanoparticle arrays. Physical review letters, 101(14):143902, 2008.

[112] Parry Y Chen, Egor A Muljarov, and Yonatan Sivan. Lightning-fast solution of scattering problems in nanophotonics: an effortless modal approach (conference presentation). In Nanophotonics VIII, volume 11345, page 113450T. International Society for Optics and Photonics, 2020.

[113] Justin C Norman, Drew F DeJarnette, and D Keith Roper. Polylogarithm-based computation of fano resonance in arrayed dipole scatterers. The Journal of Physical Chemistry C, 118(1):627–634, 2014.

[114] Katherine N Kanipe, Philip PF Chidester, Galen D Stucky, Carl D Meinhart, and Martin Moskovits. Properly structured, any metal can produce intense surface enhanced raman spectra. The Journal of Physical Chemistry C, 121(26):14269–14273, 2017.

[115] Danqing Wang, Jun Guan, Jingtian Hu, Marc R Bourgeois, and Teri W Odom. Manipulating light–matter interactions in plasmonic nanoparticle lattices. Accounts of chemical research, 52(11):2997–3007, 2019.

[116] Charles Cherqui, Marc R Bourgeois, Danqing Wang, and George C Schatz. Plasmonic surface lattice resonances: Theory and computation. Accounts of chemical research, 52(9):2548–2558, 2019.

[117] Alejandro Manjavacas, Lauren Zundel, and Stephen Sanders. Analysis of the limits of the near-field produced by nanoparticle arrays. ACS nano, 13(9):10682–10693, 2019.

[118] Yukie Yokota, Kosei Ueno, Vygantas Mizeikis, Saulius Juodkazis, Keiji Sasaki, and Hiroaki Misawa. Optical characterization of plasmonic metallic nanostructures fabricated by high-resolution lithography. Journal of Nanophotonics, 1(1):011594, 2007.

[119] Johan Grand, Pierre-Michel Adam, Anne-Sophie Grimault, Alexandre Vial, Marc Lamy De La Chapelle, Jean-Louis Bijeon, Sergei Kostcheev, and Pascal Royer. Optical extinction spectroscopy of oblate, prolate and ellipsoid shaped gold nanoparticles: experiments and theory. Plasmonics, 1(2-4):135–140, 2006.

[120] J Luypaert, DL Massart, and Y Vander Heyden. Near-infrared spectroscopy applications in pharmaceutical analysis. Talanta, 72(3):865–883, 2007.

[121] Bart M Nicolai, Katrien Beullens, Els Bobelyn, Ann Peirs, Wouter Saeys, Karen I Theron, and Jeroen Lammertyn. Nondestructive measurement of fruit and vegetable quality by means of nir spectroscopy: A review. Postharvest biology and technology, 46(2):99–118, 2007.

[122] Nuria Prieto, Olga Pawluczyk, Michael Edward Russell Dugan, and Jennifer Lynn Aalhus. A review of the principles and applications of near-infrared spectroscopy to characterize meat, fat, and meat products. Applied spectroscopy, 71(7):1403–1426, 2017.

[123] Claudia A Teixeira Dos Santos, Miguel Lopo, Ricardo NMJ Páscoa, and João A Lopes. A review on the applications of portable near-infrared spectrometers in the agro-food industry. Applied spectroscopy, 67(11):1215–1233, 2013.

[124] Yu Xia, Yunfei Xu, Jiangbo Li, Chi Zhang, and Shuxiang Fan. Recent advances in emerging techniques for non-destructive detection of seed viability: A review. Artificial Intelligence in Agriculture, 2019.

[125] Lauren Zundel and Alejandro Manjavacas. Finite-size effects on periodic arrays of nanostructures. Journal of Physics: Photonics, 1(1):015004, 2018.

[126] Jiha Sung, Erin M Hicks, Richard P Van Duyne, and Kenneth G Spears. Nanoparticle spectroscopy: Plasmon coupling in finite-sized two-dimensional arrays of cylindrical silver nanoparticles. The Journal of Physical Chemistry C, 112(11):4091–4096, 2008.

[127] Akira Matsushima. Effect of periodicity in the light scattering from infinite and finite arrays of silver nanospheres. In 2017 IEEE International Conference on Computational Electromagnetics (ICCEM), pages 236–237. IEEE, 2017.

[128] Honghui Shen, Peter Bienstman, and Bjorn Maes. Plasmonic absorption enhancement in organic solar cells with thin active layers. Journal of Applied Physics, 106(7):073109, 2009.

[129] Anton A Starovoytov, Rezida D Nabiullina, Igor A Gladskikh, Vladimir A Polischuk, Peter S Parfenov, and Aisylu N Kamalieva. Plasmon-exciton interaction in the thin film of inhomogeneous ensemble of silver nanoparticles and cyanine j-aggregates. In Nanophotonics VII, volume 10672, page 106723O. International Society for Optics and Photonics, 2018.

[130] Stefan Alexander Maier. Plasmonics: fundamentals and applications. Springer Science & Business Media, 2007.

[131] R Barer and S Tkaczyk. Refractive index of concentrated protein solutions. Nature, 173(4409):821–822, 1954.

[132] Adam M Davidson, Mathias Brust, David L Cooper, and Martin Volk. Sensitive analysis of protein adsorption to colloidal gold by differential centrifugal sedimentation. Analytical chemistry, 89(12):6807–6814, 2017.

[133] AA Malina and Przhibelskiĭ. Variation of the plasma oscillation eigenfrequencies in metal nanoparticles upon their attachment to dielectric micro-objects.

[134] Graham A Dunn. Quantitative interference microscopy. In New Techniques of Optical Microscopy and Microspectroscopy, pages 91–118. Springer, 1991.

[135] Michael I Mishchenko, Joop W Hovenier, and Larry D Travis. Light scattering by nonspherical particles: theory, measurements, and applications, 2000.

[136] Andrew E Ekpenyong, Si Ming Man, Sarra Achouri, Clare E Bryant, Jochen Guck, and Kevin J Chalut. Bacterial infection of macrophages induces decrease in refractive index. Journal of biophotonics, 6(5):393–397, 2013.

appendix A

Self-organized plasmonic metasurfaces: the role of the Purcell effect in metal-enhanced chemiluminescence (MEC)

Daler R. Dadadzhanov[a,b], Igor A. Gladskikh[b], Mikhail A. Baranov[b], Tigran A. Vartanyan[b] and Alina Karabchevsky[a,*]

[a]School of Electrical and Computer Engineering, Ben-Gurion University of the Negev, Beer-Sheva 8410501, Israel
[b]ITMO University, 49 Kronverksky Ave., 197101, St. Petersburg, Russia

ARTICLE INFO

ABSTRACT

Chemiluminophores are entities, which exhibit wide-band light emission without any external light source, due to the chemical reaction that results. Since the chemiluminophores usually have low efficiency due to unfavorable competition of chemiluminescence with other channels of chemical energy, plasmonic nanoparticles can be employed to enhance the chemiluminescence quantum yield via acceleration of the radiative decay rate due to the Purcell effect. On the other hand, the catalytic action of metallic surface can contribute to chemical reaction rate. Both channels can lead to substantial chemiluminescence intensity enhancement of luminophores in contact with metal nanoparticles. Despite the numerous investigations devoted to MEC, the relative roles of the Purcell effect and catalysis in the chemiluminescence enhancement was not cleared up. In this paper, we use a thin inert spacer layer deposited on top of a silver metasurface to reveal the main contribution to chemiluminescence enhancement. We found that the mechanism of the chemiluminescence enhancement is a combined effect of electrodynamic mechanism connected to the localized surface plasmon excitation together with catalytic effect of metals. As the results were in favor of electrodynamic mechanism of MEC, silver nanoparticles with suitable properties have been fabricated via physical vapor deposition on substrate. We performed theoretical optimization of the silver nanoparticles shape and size distributions to tune their localized surface plasmon bands for the best overlap with emission of other chemiluminophores. Our design for plasmonic nanoparticles placed on the dielectric material may make it possible to create a new generation of chemiluminescence-based devices for sensing application.

1. Introduction

Chemiluminescence, or "liquid light" effect, is an emission of photons resulting in an exothermic reaction [1]. This fascinating optical effect finds its use in various applications from forensic science (e.g. for detection the blood traces at crime scene [2]) to industrial bio-chemistry [3, 4]. Luminol is the chemiluminophore (a chemical that exhibits chemiluminescence) which generates blue light under the certain conditions [5]. It is well known that forensic investigators use luminol to detect trace amounts of blood at crime scenes since it reacts with the iron in hemoglobin, while biologists use it in cellular assays to detect copper, iron, and specific proteins [6]. However, the intensity of the luminol chemiluminescence is very low, which significantly limits its potential applications.

One of the efficient experimental tools for observing the chemiluminescence effect is a microfluidic chip. Such chips are employed to study low volume samples by isolating key phenomena from the influential surrounding environment [7]. The flow-injection in microfluidic chips helps in obtaining the efficient chemical reaction when the chemiluminophores and their oxidants are mixed to emit light. Crucial developments for the fabrication approaches in the field of microfluidic technology platform have already created high-demanded applications such as the lung-on-a-chip platform [8–10], single-cell functional proteomics [11, 12]. Moreover, these developments allow measuring the dynamics of green fluorescence protein [13, 14]. The efficient emission of luminol is expected to find applications in forensic science-on-a-chip, accurate DNA profiling with active lasing dust.

In this paper, we report on the novel metal-enhanced chemiluminescence (MEC) sensor which has significantly improved resistance to organic solvents and mechanical damage. So far, all attempts to enhance the weak chemiluminescence of luminol by plasmonic nanoparticles have insufficient information on the enhancement mechanisms either catalysis or the effect of an enhanced near-field of nanoparticles. According to [4], both the purely chemical catalytic

✉ alinak@bgu.ac.il (A. Karabchevsky)
ORCID(s):

effect of the contact with the metal surface and the Purcell electromagnetic effect contribute to the MEC activity, but the relative role played by the two in the observed enhancement is not clearly determined. Table 1 represents a brief overview of the latest results related to the chemiluminescent enhancements of luminol as well as chemiluminescent species used in glow sticks [15–17]. The main peculiarity of luminol is biocompatibility which in turn allows its use for pharmaceuticals and biological sciences. Based on our recent work [1] using the colloidal solution of metal nanospheres with luminol flowing in a microfluidic chip, we have switched from large consumable volumes of nanoparticles to small ones by using a planar metasurface of silver nanoparticles. To the best of our knowledge, this is the first application of the plasmon metasurfaces fabricated on a dielectric substrate for luminol chemiluminescence enhancement. Our experimental results provide clear evidence that the catalytic action of silver is of minor importance as compared to the Purcell effect. In this regard, the metal metasurface optimization, which allows for chemiluminescence intensity enhancement by means of the electromagnetic effects is of particular importance. Numerical modelling let us to choose the experimentally realizable shape of metal nanoparticles that ensures perfect overlap between the plasmon bands of metal metasurface and chemiluminescent bands of chemiluminophores.

Table 1
An overview of Chemiluminiscence sensors using different enhancement strategies.

Chemiluminescent system	Comments	Reference
Ag and Au with luminol-NaOH	The CL enhancement in microfluidic chip initiated by small sphere nanoparticles. The enhancement factor is up to 4-fold.	[1]
Ag-luminol-H_2O_2-HRP	A silver modified immunoassay for determination mycotoxins using luminol with amplified chemiluminescence on the chip through the surface plasmon resonance phenomenon. The enhancement factor is ~ 2-fold.	[18]
Cr, Cu, Ni, and Zn metal films with green dye	The chemiluminescence intensity from chemiluminophore (commercially available kits, Omnioglow company - acridan oxalate system) was enhanced by metal films. The enhancement factor is up to 3-fold.	[15]
Al, Au, Ag metal films with red, green and blue dyes	The luminophores dyes excited the surface plasmons on thin continuous metal films without incident excitation light. The CL species/SPR coupling demonstrates a highly polarized and directional emission. The enhancement factor was not estimated.	[17]
Ag SIF with green dye-H_2O_2	The commercially available chemiluminophores from glow-stick (commercially available kits, Omnioglow company) was enhanced by metal films. The enhanced chemiluminescence intensity is around 20-fold.	[16]

It is important to note that the quantum efficiency of the chemiluminescence process is quite low due to the competition with a multitude of non-radiative decay processes [19]. Hence, radiative decay acceleration of the chemiluminophore excited state is a reliable way to enhance the chemiluminescence yield that attracts the attention of many scientists [1, 20, 21]. In turn, the surface plasmon resonance in metallic nanoparticles [22, 23] can be employed for the acceleration of these radiative transitions. Figure 1 summarizes the schematics of the chemiluminescence enhancement mechanism.

Figure 1a represents the luminol excitation in the course of a chemical reaction with oxidizer followed by two competitive decay routes: radiative and non-radiative. The effect of silver nanoparticles (AgNP) on the luminol emission is depicted in Figure 1c. The expected chemiluminescence enhancement originates due to the Purcell effect that couples the luminol emission with the enhanced local fields in the vicinity of AgNP [24]. As a result, the density of photon states increases and the process of chemiluminescence is boosted. This effect reaches its maximum in the close proximity of the nanoparticles and vanishes at larger distances. At the same time, a direct contact with the metal surface is known to lead to the luminescence quenching. Since the luminescence quantum yield (η) is determined by the

competition of radiative (γ_R) and non-radiative (γ_{NR}) decay processes then in case of γ_{NR} is larger or the same order of magnitude as γ_R growth of γ_R it leads to the substantial growth of the luminescence quantum yield provided the growth of γ_{NR} is smaller than the growth of γ_R. Therefore, the chemiluminescence quantum yield in the presence of metal nanoparticles grows according to the formula $\eta \propto \frac{\gamma'_R}{\gamma'_R + \gamma'_{NR}}$. Indeed, this phenomenon known as metal-enhanced fluorescence (MEF) was reported in previous research [25, 26]. As compared to MEF where the molecule initially has to be pumped by an external light, metal-enhanced chemiluminescence (MEC) stems from the chemical oxidation process [27, 28], as shown in the Jablonski diagram (Figure 1c). Thus, the chemiluminescence intensity can be increased by plasmon nanoparticles provided the condition of the increased radiative decay rate ($\gamma'_R > \gamma_R$) is fulfilled while γ_{NR} does not substantially grow.

To maximize the chemiluminophores-nanoparticles pair interaction, metal nanoparticles have to be placed at an optimum distance from the chemiluminophores [29]. The shape and material of the particles have to be accurately chosen to ensure the overlapping of their absorption plasmonic band with the emission band of the chemiluminophores[30]. In our previous work, the new proof-of-concept experiment was perfomed with the microfluidic chip [1], wherein we utilized the commercially available nanoparticles with non-optimized spectral location of the absorption plasmon absorption band. Therefore, the chemiluminescence quantum yield can be further improved with specially designed surfaces. In this article, we show that the self-organized metasurfaces with broadband and tunable plasmon resonances, which are necessary for effective interaction between nanoparticle acceptors and chemiluminophore donors, may be obtained by via previously developed manufacturing technology [31–33]. Moreover, we demonstrate the benefits of fabricating AgNPs on a quartz substrate using physical vapor deposition (PVD). We found that the width and the position of nanoparticles' plasmon bands are tuned via PVD process and subsequent annealing. The spectral position of the plasmon absorption band may be controlled by the amount of the sputtered metal in order to provide a spectral overlap with the emission bands of chemiluminescent species. Consequently, the fulfilment of the requirements for effective acceleration of radiative transitions in luminol seems feasible.

As a result, two conditions ought to be satisfied for the effective interaction between the plasmonic nanoparticle and the chemiluminophore: 1) the plasmon band has to overlap with the chemiluminescence emission band [1, 30, 34] and 2) the chemiluminophore molecules need to be in the close proximity with metal nanoparticles [1, 35]. In this work, we explore the possibility of fulfilling both conditions with AgNPs as *acceptors* and the chemiluminophore molecules as *donors* of energy quanta. As the plasmon band of small spherical AgNPs lies on the far blue wing of the luminol chemiluminescence band, we utilize two fabrication approaches to shift the plasmon band in the desired red direction: enlarging the nanosphere radius and changing the nanoparticle shape. To keep the transfer of the technology feasible, we rely on the well-established and rather affordable techniques of AgNPs production, namely, PVD on the dielectric substrate. According to our numerical predictions, plasmon resonances in truncated AgNPs are red-shifted and resonantly coupled with the luminol molecules.

2. Materials and methods

2.1. Synthesis of supported silver nanoparticles via physical vapor deposition

We fabricated AgNPs on the microscope glass slide using the physical vapor deposition in a vacuum chamber PVD-75 (Kurt J. Lesker). All microscope slides were preliminarily washed in ethanol and then washed with distilled water. AgNP ensemble was grown according to the Volmer-Weber mechanism. The equivalent thickness of AgNP ensemble was 5 nm and controlled by a quartz crystal microbalance during the growth. The silver plate (99,99% purity) was evaporated in high vacuum ($1 \cdot 10^{-6}$ Torr). Then, the obtained silver film was annealed at 200 °C. The spectral position of the plasmon absorption band was controlled by the amount of the evaporated metal and the evaporation rate as well as by the temperature and the duration of the subsequent annealing [31]. To obtain the ensemble of AgNPs, the silver deposition was used at a rate 0.1Å per second. The red-shift of the plasmon resonance band with a maximum around 482 nm was achieved by thermal annealing of the silver film for 30 minutes. To provide better adhesion of AgNPs to the substrate and ensure their stability in the oxidizing environment in the course of the chemiluminescence studies, the laser-assisted approach was conducted. The laser exposure was realized by the third harmonic (355 nm) of a Q-switched Nd:YAG laser (SOLAR Laser Systems). The pulse duration and the repetition rate were 10 ns and 10 Hz, respectively. The laser beam, with the diameter of 8 mm, was focused on the AgNP ensemble supported on the glass substrate and scanned over the entire film. The pulse energy was controlled by filters and set to 20 mJ. To reach stronger adhesion of silver nanoparticles to the substrate the samples were irradiated with 100 laser pulses. The AgNP

substrate covered with 2 nm SiO$_2$ layer was prepared to estimate the role of the catalysis effect from silver according to the procedure in ref. [36].

2.2. Characterization studies

Scanning electron microscope images of supported silver nanoparticles were obtained with MERLIN (Carl Zeiss) microscope at 15 kV. Optical extinction spectra of silver nanoparticles on the substrate were collected using an SF-56 spectrophotometer (LOMO) with 1 nm resolution in the range of 250 - 1100 nm at room temperature. The chemiluminescent spectra of luminol were recorded by a charge-coupled device (CCD), Lumenera Infinity 2-3C (Lumenera Corporation, 7 Capella Crt. Ottawa, Ontario, Canada). A digital photographic camera (Canon) with a high integration time was used to capture chemiluminescence light and record the images of glowing samples. In addition to the experiments with luminol, the chemiluminescent spectra of 9,10-diphenylanthracene (DPA) molecules were also obtained by a spectrofluorometer (Cary Eclipse) while the excitation source of the spectrofluorometer was off.

2.3. Complexes of AgNP@Chemiluminophore

A stock solution (*next denoted as "solution 1"*) of 3-aminophthalhydrazide (luminol) with the concentration of $2.8 \cdot 10^{-5}$ M in deionized water, purchased from Sigma Aldrich, was mixed with sodium hydroxide (NaOH), with the concentration of 1 mM. A 5% solution of sodium hypochlorite (NaOCl), was used as an oxidizing agent (*next denoted as "solution 2"*). Chemiluminescent radiation occurs as a result of a chemical reaction between organic chemiluminophore molecules and an oxidizing agent. In addition, we conducted an experiment with DPA. All chemiluminophore species were placed between two microscope glass slides, one of which was partially covered with silver nanoparticles embedded in advance.

2.4. Numerical simulation

The Finite-Element-Method (FEM) implemented in COMSOL Multiphysics 5.4 software (Wave Optics Module) was used to solve Maxwell's equations for stationary problems. We calculated absorption, scattering and extinction cross-section spectra of AgNPs varying their shapes and substrates to predict the behavior in combination with chemiluminophores. We have built a 3D box that contains two domains, with a width of 200 nm, intended for the dielectric substrate and surrounding media. A perfectly matched layer (PML) was included as a physical domain with the thickness of 150 nm to absorb scattered light. We define the thickness of PML as a half of the incident wavelength. The PML layer was divided by 8 equidistant layers. The silver nanoparticle was placed in the center domain with subsequent meshing in the form of tetrahedral elements. Maximum element size of the surrounding medium, dielectric substrate and nanoparticle were chosen as $\lambda/6$ when the electromagnetic incident field oscillated parallel to the substrate with a k-vector perpendicular to the substrate. The parametric sweep was used to calculate the absorption, scattering and extinction cross-sections of plasmonic nanoparticles as described in ref.[37], in the range of 350-750 nm. Since the dephasing time of plasmon silver nanoparticles (for $r > 10$ nm) deposited on a dielectric substrate remained practically unchanged as shown in [38], the correction for a quantum-confinement size effect was neglected. Thus, the complex refractive index of the AgNP from the experimental work of Johnson and Christy for bulk silver [39] was implemented for the modeling.

3. Results and Discussion

3.1. Experimental results

In this section we experimentally investigate the relative contributions of plasmonic and catalytic mechanisms in the chemiluminescence intensity enhancement due to the silver metasurface. Firstly let us consider the process scheme of step-by-step morphology modification starting from a deposited thin film to the inhomogeneous ensemble of silver nanoparticles as shown in Figure 2. This technique was used to obtain plasmonic nanoparticles optimized for the luminol chemiluminescence enhancement. Chemiluminescence of different chemiluminophores may be enhanced via the suggested technique, the dedicated choices of substrates, and annealing procedures [31].

Using the time/temperature dependence of the annealing process, we achieve the desired AgNPs shape and size distributions that lead to plasmonic band in the aimed spectral range. However, the fabricated self-organized metasurfaces of AgNPs were mechanically unstable and may be damaged by organic/non-organic solvents, i.e. water, ethanol, hexane and others. To overcome this limitation, we developed a novel approach for strong adhesion of AgNPs to the dielectric substrates. In particular, after annealing process, the thin silver film was exposed to the pulsed laser irradiation at the wavelength of 355 nm. Figure 2a shows the extinction spectrum of the continuous silver film, whose

plasmon absorption band is out of the spectral region necessary to overlap with the luminol emission band. As it is seen in Figure 2b, the extinction spectrum after the subsequent annealing process is characterized by the sharp absorption plasmon resonance band in the visible range. Under the laser irradiation, the plasmon band broadens whereas its overlap with chemiluminescence emission spectra becomes greater (Figure 2c). From the experimental point of view, it is essential to improve the chemical and mechanical stability of the metal films because the chemical reagents used in the chemiluminophore solution are very aggressive. We found that dripping of a mixer of *"solution 1"* and *"solution 2"* does not degrade the substrate with the AgNP metasurface. It is worth noting that the adhesion of AgNPs to the substrate was also improved (Figure 2c). This property was confirmed by scratching the film with a sharp object. Thus, the laser irradiation leads formation to stable in organic solvents and resistant to mechanical damages samples. These samples are suitable for chemiluminescence experiments, unlike the untreated samples.

To clarify the morphology of the prepared AgNP metasurface, we analyzed the SEM images before and after the annealing process as depicted in Figure 3. We observe two distinct ensembles of larger and smaller nanoparticles in both images. The image of AgNPs obtained after annealing procedure shows the presence of rather similar larger nanoparticles with diameters not exceeding 160 nm. After the laser irradiation, all AgNPs becomes larger and more rounded. At the same time, the size distribution becomes broader and the distinction between ensembles of larger and smaller particles becomes more pronounced (see Figure 3). Consequently, the extinction spectrum of the silver nanoparticles in Figure 2c shifts and broadens.

The measured extinction spectra of the AgNP metasurface after the laser irradiation exhibit the pronounced plasmon bands in range of 350 to 650 nm with a maximum at 482 nm (Figure 4). The inset of Figure 4 shows a photograph of the substrate (1) and the substrate with the AgNPs (2) fabricated via PVD and subjected to both the subsequent annealing and laser irradiation. We noticed that the film has a definite brown color that corresponds to the spectral position of the absorption band of the fabricated AgNPs, as shown in Figure 4. As it was mentioned above, to boost the chemiluminescent emission, the overlap between the chemiluminophore (donor) luminescent band and AgNPs (acceptor) absorption band is required. To show this overlap, the normalized chemiluminescent spectrum (CL) of luminol is plotted in the same graph. The chemiluminescent spectra of luminol consists of two overlapping emission bands with maxima at the wavelengths of 452 nm and at the wavelengths of 489 nm, respectively. The plasmon band of the prepared AgNP samples is overlapped with both luminol chemiluminescence emission bands. In addition, we observed that the DPA chemiluminescent emission band (Figure 4) spectrally is also overlapped with the absorption peak of plasmon band.

Finally, the enhanced near-field effect of synthesized AgNPs on chemiluminophore molecules has been investigated. We employed a straightforward, experimental procedure in order to show the MEC effect presence. We dripped 30 μl of *"solution 1"* onto the bare glass substrate just at the edge of AgNPs (as shown in the inset of Figure 4). Then, 30 μl of *"solution 2"* was dripped onto another glass slide and both slides are pressed to each other in such a way that both solutions are mixed. The thickness of the gap between two substrates was estimated as about 10 μm based on the simulation of the oscillations in the transmission spectrum [40]. Then we took photographs of the substrates with nanoparticles at the moment of luminol and DPA glowing. The normalized distribution of the CL intensities are demonstrated in Figure 5a for luminol and Figure 5b for DPA. The sharp jump in the chemiluminescence intensity of both luminol and DPA is clearly seen at the edges of AgNPs covered regions (Figure 5). In this respect, we observed that the chemiluminescence intensity of luminol with the presence of AgNPs is enhanced by 1.6 times, while in case of DPA the enhancement factor reaches 1.5.

3.2. Influence of the Purcell effect on the MEC

When reagents are contacted directly to the silver metasurface with plasmon resonances absorption band within the chemiluminescence bands of luminol, the chemiluminescence intensity is increased by 1.6 times. To clarify the relative role of the Purcell effect and the catalytic effect of silver in this enhancement, additional experiments were performed. First, an identical AgNPs substrate was covered with 2 nm SiO_2 spacer layer (the inset of Figure 6a). It was expected that the catalytic effect of AgNPs completely disappears, since it requires direct contact between the reactants and nanoparticles. Nevertheless, in spite of the increased distance between the reactants and AgNPs, the Purcell effect remains. Indeed, in the presence of the spacer, the enhancement factor drops to 1.3 factor (Figure 6a). It should also be noted that inhomogeneous distribution of the chemiluminescent intensity in the SiO_2 area that can be seen in Figure 6a is due to the tolerances of the applied pressure on microscope cover slip that leads to the slightly uneven distribution of the mixture. Yet, the jump of chemiluminescence intensity at the boundary of the metasurface is clearly visible.

Thus, the decisive role of the Purcell effect was confirmed. In this case, an increase in chemiluminescence enhancement with a decrease in the distance between reagents and AgNPs was naturally explained. In order to estimate the role of catalysis in chemiluminescence enhancement in the absence of the spacer, we also conducted the experiment with a silver film that has no plasmon resonances in the chemiluminescence bands of luminol. If chemiluminescence is also enhanced in this case, this enhancement should be attributed to the catalytic effect of silver. However, in Figure 6b one can observe no difference in the chemiluminescence intensities from the regions of the plain dielectric substrate and silver film without plasmon resonances. Consequently, the 1.6-fold enhancement of chemiluminescence observed upon direct contact of the reagents with the silver film with plasmon resonances in the chemiluminescence bands can be completely attributed to the Purcell electrodynamic effect.

3.3. Numerical studies for AgNP@luminol configuration

As shown in Figure 7, the main luminol chemiluminescence emission bands appear at 452 nm and 489 nm, respectively, while the plasmon resonances of small silver and gold nanospheres in aqueous environment have their maxima at the wavelengths of 415 nm and 528 nm respectively [1]. Hence, the most promising way to establish the desired resonance interaction is to choose the silver as the nanoparticles material, and change its 1) size, 2) shape and 3) surrounding. These three approaches may be employed to shift the localized surface plasmons in AgNPs to longer wavelengths. Thus, the dedicated plasmonic-chemiluminophore system design that takes advantage of plasmonic nanoparticles tuning can lead to efficient enhancement of the chemiluminescence effect. By taking advantage of the fabrication of AgNPs on dielectric substrates using PVD in ultrahigh vacuum, the long-wavelength shift of the plasmon bands of AgNPs can be achieved by: direct contact of the metal nanoparticles with a substrate having a higher dielectric permittivity than water, as well as the oblated shape of the nanoparticles obtained on surface of the substrate during the deposition process. To explore if these two mechanisms may be well-balanced to provide the desired conditions for the plasmon band, we considered common transparent dielectric substrates: glass, quartz (SiO_2), sapphire (Al_2O_3), magnesium fluoride (MgF_2), and titanium dioxide (TiO_2).

Figure 7 shows extinction, absorption and scattering cross-sections spectra computed for nanoparticles supported on the glass substrate. The supported AgNPs were assumed to be submerged in a luminol solution. Since luminol expected to be diluted with a high ratio in water, the refractive index of the surrounded media was set to that of water, 1.33. The shape of nanoparticles obtained by PVD was assumed to be a hemisphere while their diameter was continuously changed to match the absorption plasmon band to the chemiluminescent emission spectra of luminol. We found out that the absorption cross-section of the optimally-tuned AgNPs is 12 times larger than the geometrical cross-section of AgNPs. According to our calculations presented in Figure 7, an ideal matching with the first luminol emission peak at 489 nm is achieved for silver hemispheres with 20 nm diameter deposited on the glass substrate (refractive index $n = 1.51$).

However, the calculations show that the absorption plasmon band of AgNPs on the glass substrate provides no spectral overlap with the second luminol chemiluminescence emission peak located at 452 nm even using the smallest hemispheres nanoparticles. Yet the resonance condition between the absorption plasmon band and the luminol emission peak at 452 nm may be restored for the truncated sphere of 20 nm in diameter and the height of $h = 13$ nm. The possibility for resonance plasmon band tuning of gold nanoparticles toward long-wavelength range has been numerically demonstrated by means of the truncating the spherical nanoparticles [41]. We notice that the high refractive index substrates (e.g. sapphire having the refractive index as high as 1.77 [42, 43] and titanium dioxide substrate) lead to inefficient overlapping of silver absorption plasmon band with the luminol emission since the long-wavelength shift is too large even for the very small silver hemispheres. On the contrary, the high refractive index substrates can be considered for those chemiluminophore molecules that have emission band in long-wavelength side. Therefore, we assume that to enhance the chemiluminescence effect of luminol using the AgNPs array, the glass substrate is a more reasonable choice.

3.4. Numerical calculation for alternative metal-enhanced chemiluminescence configuration on dielectric substrate

As luminol is not the sole substance that is widely used in various applications as chemiluminophore, here we present a manifold of substrate-nanoparticle pairs optimized for surface-enhanced chemiluminescence. Following the well-known chemiluminophores: $KMnO_4$ in Figure 8, Lucigenin in Figure 9a, b, Ce (IV) in Figure 9c,d, and bis-(2,4,6-tricholorophenyl) oxalate (TCPO) in Figure 9e,f have been considered. We optimized the diameters of silver hemispheres for $KMnO_4$ chemiluminescent emission spectra (Figure 8) with the emission band maximum at

700 nm [44]. As an alternative example of a chemiluminescent agent, we considered Lucigenin. This substance is widely used in analytical science whereas its the emission band maximum is located at 480 nm. [45–48] (Figure 9a, b). The absorption, scattering and extinction cross-section spectra of silver hemisphere optimized for Cerium (IV) chemiluminescent emission spectra are presented in Figure 9c, d. The emission band maximum peak lies at $\sim$ 550 nm [49, 50]. Then, we calculated the suitable parameters for the plasmon nanoparticle on the top of dielectric substrate for TCPO chemiluminescence emission spectra. The emission band maximum is at 485 nm (Figure 9e,f) [51].

4. Conclusions

In summary, we proposed a novel approach in designing new materials assembled from nanoparticles for enhancing chemiluminescence and a number of other effects such as spasing, DNA profiling and others. All of them are promising in terms of delivering substantial enhancement in specific and accurate detection of analytes, which is not possible via traditional approaches. We used the proposed technique for fabrication of supported silver nanoparticles ensemble with the plasmon band that peaks at 482 nm and overlaps well with the luminol emission bands. Laser treatment is shown to provide the enhanced chemical and mechanical stability of the obtained thin films materials. Combining these materials with recent advances in chemiluminescence enhancement effect demonstrated using flow-injection systems opens the door for new chemiluminophores-based light sources. These light sources, where the poor quantum emitter (chemiluminophore) is replaced by high quantum efficiency of plasmonic nanoantenna, could not have been achieved by conventional manufacturing processes in which particles size and shape are fixed. We found out that the particle arrangement on the surface of the transparent dielectrics makes it possible to control the distance between the light-emitting species and nanoantennas to elucidate the Purcell effect role in the observed chemiluminescent enhancement. The inert layer, placed on the top of the self-organised metasurface of AgNPs, allows us to eliminate the contribution of catalytic effect in the MEC activity and shows a gain in the luminescence intensity of chemiluminophore molecules due to the retained Purcell effect. We conclude that the fabrication of AgNPs using the physical vapor deposition technique in vacuum, followed by the self-organization of nanoparticles, is an affordable and convenient method leading to plasmonic enhancement for the luminol and *9,10*-diphenylanthracene chemiluminescence.

Acknowledgement

References

[1] Alina Karabchevsky, Ali Mosayyebi, and Alexey V Kavokin. Tuning the chemiluminescence of a luminol flow using plasmonic nanoparticles. *Light: Science & Applications*, 5(11):e16164, 2016. ISSN 2047-7538.

[2] Filippo Barni, Simon W Lewis, Andrea Berti, Gordon M Miskelly, and Giampietro Lago. Forensic application of the luminol reaction as a presumptive test for latent blood detection. *Talanta*, 72(3):896–913, 2007. ISSN 0039-9140.

[3] Shiro Yamashoji. Determination of viable mammalian cells by luminol chemiluminescence using microperoxidase. *Analytical biochemistry*, 386(1):119–120, 2009. ISSN 0003-2697.

[4] Mortaza Iranifam. Chemiluminescence reactions enhanced by silver nanoparticles and silver alloy nanoparticles: applications in analytical chemistry. *TrAC Trends in Analytical Chemistry*, 82:126–142, 2016. ISSN 0165-9936.

[5] Ronit Freeman, Xiaoqing Liu, and Itamar Willner. Chemiluminescent and chemiluminescence resonance energy transfer (CRET) detection of DNA, metal ions, and aptamer-substrate complexes using hemin/G-quadruplexes and CdSe/ZnS quantum dots. *Journal of the American Chemical Society*, 133(30):11597–11604, 2011. ISSN 0002-7863.

[6] Lori L Klopf and Timothy A Nieman. Effect of iron (II), cobalt (II), copper (II), and manganese (II) on the chemiluminescence of luminol in the absence of hydrogen peroxide. *Analytical Chemistry*, 55(7):1080–1083, 1983. ISSN 0003-2700.

[7] Liu Wei, Zhang Zhujun, and Yang Liu. Chemiluminescence microfluidic chip fabricated in PMMA for determination of benzoyl peroxide in flour. *Food Chemistry*, 95(4):693–698, 2006. ISSN 0308-8146.

[8] Ana Rubina Perestrelo, Ana C P Águas, Alberto Rainer, and Giancarlo Forte. Microfluidic organ/body-on-a-chip devices at the convergence of biology and microengineering. *Sensors*, 15(12):31142–31170, 2015.

[9] Pedro M Valencia, Omid C Farokhzad, Rohit Karnik, and Robert Langer. Microfluidic technologies for accelerating the clinical translation of nanoparticles. *Nature nanotechnology*, 7(10):623, 2012. ISSN 1748-3395.

[10] Aziz Ur Rehman Aziz, Chunyang Geng, Mengjie Fu, Xiaohui Yu, Kairong Qin, and Bo Liu. The role of microfluidics for organ on chip simulations. *Bioengineering*, 4(2):39, 2017.

[11] Iulia M Lazar, Phichet Trisiripisal, and Hetal A Sarvaiya. Microfluidic liquid chromatography system for proteomic applications and biomarker screening. *Analytical chemistry*, 78(15):5513–5524, 2006. ISSN 0003-2700.

[12] Jing Yu, Jing Zhou, Alex Sutherland, Wei Wei, Young Shik Shin, Min Xue, and James R Heath. Microfluidics-based single-cell functional proteomics for fundamental and applied biomedical applications. *Annual review of analytical chemistry*, 7:275–295, 2014. ISSN 1936-1327.

[13] Ana Valero, Janine Nicole Post, Jan William van Nieuwkasteele, Paulus Martinus ter Braak, W Kruijer, and Albert van den Berg. Gene transfer and protein dynamics in stem cells using single cell electroporation in a microfluidic device. *Lab on a Chip*, 8(1):62–67, 2008.

[14] Matthew R Bennett and Jeff Hasty. Microfluidic devices for measuring gene network dynamics in single cells. *Nature Reviews Genetics*, 10 (9):628, 2009. ISSN 1471-0064.

[15] Micah Weisenberg, Yongxia Zhang, and Chris D Geddes. Metal-enhanced chemiluminescence from chromium, copper, nickel, and zinc nanodeposits: Evidence for a second enhancement mechanism in metal-enhanced fluorescence. *Applied Physics Letters*, 97(13):133103, 2010.

[16] Mustafa H Chowdhury, Kadir Aslan, Stuart N Malyn, Joseph R Lakowicz, and Chris D Geddes. Metal-enhanced chemiluminescence: Radiating plasmons generated from chemically induced electronic excited states. *Applied physics letters*, 88(17):173104, 2006.

[17] Mustafa H Chowdhury, Stuart N Malyn, Kadir Aslan, Joseph R Lakowicz, and Chris D Geddes. Multicolor directional surface plasmon-coupled chemiluminescence. *The Journal of Physical Chemistry B*, 110(45):22644–22651, 2006.

[18] Fan Jiang, Ping Li, Chen Zong, and Hua Yang. Surface-plasmon-coupled chemiluminescence amplification of silver nanoparticles modified immunosensor for high-throughput ultrasensitive detection of multiple mycotoxins. *Analytica Chimica Acta*, 2020.

[19] J Lee and H H Seliger. Quantum yields of the luminol chemiluminescence reaction in aqueous and aprotic solvents. *Photochemistry and Photobiology*, 15(2):227–237, 1972. ISSN 0031-8655.

[20] Ryan Fobel, Andrea E Kirby, Alphonsus H C Ng, Ramin R Farnood, and Aaron R Wheeler. Paper microfluidics goes digital. *Advanced materials*, 26(18):2838–2843, 2014. ISSN 0935-9648.

[21] M G Ou, G W Lu, Hong Shen, Armel Descamps, Christophe Andre Marquette, Loic Jacques Blum, Gilles Ledoux, Stephane Roux, Olivier Tillement, and B L Cheng. Catalytic Performance of Nanoscale-Corrugated Gold and Silver Films for Surface-Enhanced Chemiluminescence. *Advanced Functional Materials*, 17(12):1903–1909, 2007. ISSN 1616-301X.

[22] Alina Karabchevsky, Olga Krasnykov, Mark Auslender, Benny Hadad, Adi Goldner, and Ibrahim Abdulhalim. Theoretical and experimental investigation of enhanced transmission through periodic metal nanoslits for sensing in water environment. *Plasmonics*, 4(4):281, 2009. ISSN 1557-1955.

[23] Alina Karabchevsky, Mark Auslender, and Ibrahim Abdulhalim. Dual-surface plasmon excitation with thin metallic nanoslits. *Journal of Nanophotonics*, 5(1):51821, 2011. ISSN 1934-2608.

[24] Kadir Aslan and Chris D Geddes. Metal-enhanced chemiluminescence: advanced chemiluminescence concepts for the 21st century. *Chemical Society Reviews*, 38(9):2556–2564, 2009.

[25] Alina Karabchevsky, Ibrahim Abdulhalim, Chinmay Khare, and Bernd Rauschenbach. Microspot sensing based on surface-enhanced fluorescence from nanosculptured thin films. *Journal of Nanophotonics*, 6(1):61508, 2012. ISSN 1934-2608.

[26] I Abdulhalim, Alina Karabchevsky, Christian Patzig, Bernd Rauschenbach, Bodo Fuhrmann, Evgeni Eltzov, Robert Marks, Jian Xu, Fan Zhang, and Akhlesh Lakhtakia. Surface-enhanced fluorescence from metal sculptured thin films with application to biosensing in water. *Applied Physics Letters*, 94(6):63106, 2009. ISSN 0003-6951.

[27] E M Hicks and S Zou. EM Hicks, S. Zou, GC Schatz, KG Spears, RP Van Duyne, L. Gunnarsson, T. Rindzevicius, B. Kasemo, and M. Käll, Nano Lett. 5, 1065 (2005). *Nano Lett.*, 5:1065, 2005.

[28] Kadir Aslan and Chris D Geddes. Surface plasmon coupled chemiluminescence from zinc substrates: Directional chemiluminescence. *Applied Physics Letters*, 94(7):73104, 2009. ISSN 0003-6951.

[29] Jacob B Khurgin, Greg Sun, and Richard A Soref. Enhancement of luminescence efficiency using surface plasmon polaritons: figures of merit. *JOSA B*, 24(8):1968–1980, 2007. ISSN 1520-8540.

[30] Tadesse Haile Fereja, Ariaya Hymete, and Thirumurugan Gunasekaran. A recent review on chemiluminescence reaction, principle and application on pharmaceutical analysis. *Isrn Spectroscopy*, 2013, 2013.

[31] Nikita A Toropov, Igor A Gladskikh, Peter S Parfenov, and Tigran A Vartanyan. Fabrication and laser-assisted modification of the Ag particles ensembles supporting quadrupole plasmon oscillations. *Optical and Quantum Electronics*, 49(4):154, 2017. ISSN 0306-8919.

[32] N B Leonov, I A Gladskikh, V A Polishchuk, and T A Vartanyan. Evolution of the optical properties and morphology of thin metal films during growth and annealing. *Optics and Spectroscopy*, 119(3):450–455, 2015. ISSN 0030-400X.

[33] Nikita Toropov and Tigran Vartanyan. Noble Metal Nanoparticles: Synthesis and Optical Properties. In David L. Andrews, Robert H. Lipson, and Thomas Nann, editors, *Comprehensive Nanoscience and Nanotechnology (Second Edition)*, pages 61 – 88. Academic Press, Oxford, second edition edition, 2019. ISBN 978-0-12-812296-9.

[34] Jeong-Eun Park, Jiyeon Kim, and Jwa-Min Nam. Emerging plasmonic nanostructures for controlling and enhancing photoluminescence. *Chemical science*, 8(7):4696–4704, 2017.

[35] Chris D Geddes. *Surface plasmon enhanced, coupled and controlled fluorescence*. John Wiley & Sons, 2017. ISBN 1118027930.

[36] Nikita A Toropov, Aisylu N Kamalieva, Roman O Volkov, Ekaterina P Kolesova, Dominika-Olga A Volgina, Sergey A Cherevkov, Aliaksei Dubavik, and Tigran A Vartanyan. Direct enhancement of luminescence of $Cd_xZn_{1-x}Se_yS_{1-y}$/ZnS nanocrystals with gradient chemical composition by plasmonic nanoantennas. *Optics & Laser Technology*, 121:105321, 2020.

[37] Daler R Dadadzhanov, Tigran A Vartanyan, and Alina Karabchevsky. Differential extinction of vibrational molecular overtone transitions with gold nanorods and its role in surface enhanced near-ir absorption (senira). *Optics express*, 27(21):29471–29478, 2019.

[38] J Bosbach, C Hendrich, F Stietz, T Vartanyan, and F Träger. Ultrafast dephasing of surface plasmon excitation in silver nanoparticles: influence of particle size, shape, and chemical surrounding. *Physical review letters*, 89(25):257404, 2002.

[39] Peter B Johnson and R-W_ Christy. Optical constants of the noble metals. *Physical review B*, 6(12):4370, 1972.

[40] JC Manifacier, J Gasiot, and JP Fillard. A simple method for the determination of the optical constants n, k and the thickness of a weakly

absorbing thin film. *Journal of Physics E: Scientific Instruments*, 9(11):1002, 1976.

[41] Vasanthan Devaraj, Hyuk Jeong, Chuntae Kim, Jong-Min Lee, and Jin-Woo Oh. Modifying plasmonic-field enhancement and resonance characteristics of spherical nanoparticles on metallic film: Effects of faceting spherical nanoparticle morphology. *Coatings*, 9(6):387, 2019.

[42] Mark W Knight, Yanpeng Wu, J Britt Lassiter, Peter Nordlander, and Naomi J Halas. Substrates matter: influence of an adjacent dielectric on an individual plasmonic nanoparticle. *Nano letters*, 9(5):2188–2192, 2009. ISSN 1530-6984.

[43] Xiaotong Liu, Dabing Li, Xiaojuan Sun, Zhiming Li, Hang Song, Hong Jiang, and Yiren Chen. Tunable dipole surface plasmon resonances of silver nanoparticles by cladding dielectric layers. *Scientific reports*, 5:12555, 2015. ISSN 2045-2322.

[44] Christopher M Hindson, Paul S Francis, Graeme R Hanson, Jacqui L Adcock, and Neil W Barnett. Mechanism of permanganate chemiluminescence. *Analytical chemistry*, 82(10):4174–4180, 2010. ISSN 0003-2700.

[45] Yi He and Hua Cui. Fabrication of luminol and lucigenin bifunctionalized gold nnanoparticles/graphene oxide nanocomposites with dual-wavelength chemiluminescence. *The Journal of Physical Chemistry C*, 116(23):12953–12957, 2012. ISSN 1932-7447.

[46] Ji-Zhao Guo and Hua Cui. Lucigenin chemiluminescence induced by noble metal nanoparticles in the presence of adsorbates. *The Journal of Physical Chemistry C*, 111(33):12254–12259, 2007. ISSN 1932-7447.

[47] Takeyoshi Okajima and Takeo Ohsaka. Chemiluminescence of lucigenin by electrogenerated superoxide ions in aqueous solutions. *Luminescence: The journal of biological and chemical luminescence*, 18(1):49–57, 2003. ISSN 1522-7235.

[48] Bo Liu, Yi He, Chunfeng Duan, Na Li, and Hua Cui. Platinum nanoparticle-catalyzed lucigenin-hydrazine chemiluminescence. *Journal of Photochemistry and Photobiology A: Chemistry*, 217(1):62–67, 2011. ISSN 1010-6030.

[49] Xijuan Yu, Qiujin Wang, Xiangnan Liu, and Xiliang Luo. A sensitive chemiluminescence method for the determination of cysteine based on silver nanoclusters. *Microchimica Acta*, 179(3-4):323–328, 2012. ISSN 0026-3672.

[50] Shi-Feng Li, Xin-Ming Zhang, Zi-Jian Yao, Rui Yu, Fei Huang, and Xian-Wen Wei. Enhanced chemiluminescence of the rhodamine 6G-cerium (IV) system by Au- Ag alloy nanoparticles. *The Journal of Physical Chemistry C*, 113(35):15586–15592, 2009. ISSN 1932-7447.

[51] Lijuan Wang and Yuhai Tang. Determination of dipyridamole using TCPO-H2O2 chemiluminescence in the presence of silver nanoparticles. *Luminescence*, 26(6):703–709, 2011. ISSN 1522-7235.

[52] Mara Mirasoli, Massimo Guardigli, and Aldo Roda. Chemiluminescence in Biomedicine. In *Applied Photochemistry*, pages 427–458. Springer, 2016.
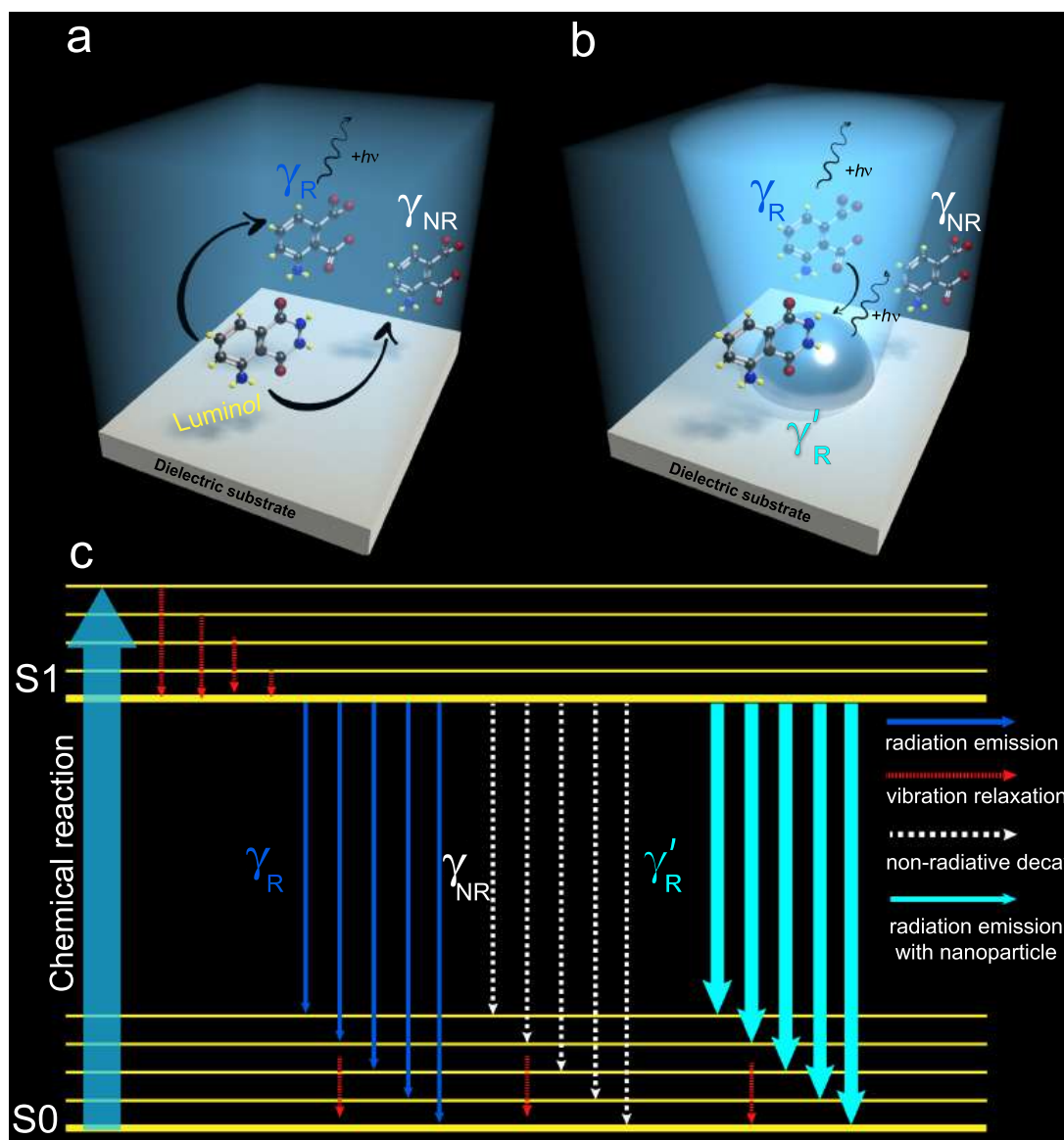
Figure 1: Schematic enhancement mechanism of the chemiluminescence effect. (a) the luminol oxidation leads to competitive processes of radiative decay (emission of a photon) and non-radiative decay (production of heat). The blue color emission is attributed to the luminol emission. (b) The proposed mechanism of the metal-enhanced chemiluminescence in the presence of AgNP. (c) The general Jablonski energy level diagram modified for the chemiluminescence emission in the presence of AgNP[52]. The chemiluminescence emission origin as a result of chemical oxidation process. The molecular transition from the excited ($S1$) to the electron ground state ($S0$) leads to the photon emission and heat production. γ_R and γ_{NR} are the radiative and non-radiative decay rates of the luminol molecules. $\gamma_{R'}$ is the radiative decay rate of luminol molecules in the vicinity of AgNP.
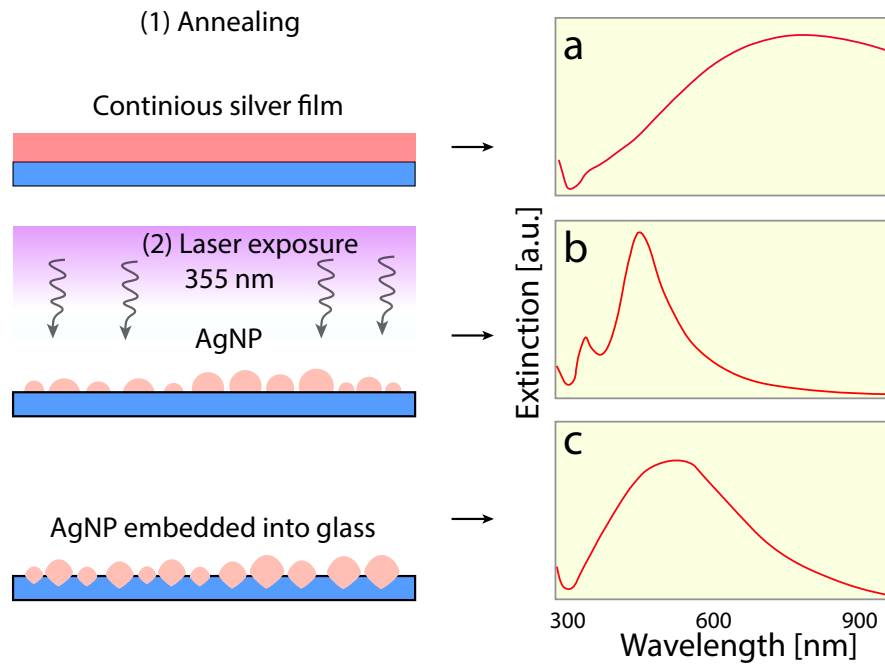
Figure 2: The proposed process scheme of silver nanoparticles ensemble preparation and the extinction spectra evolution: (a) a continuous film, (b) after annealing treatment, and (c) after laser exposure.
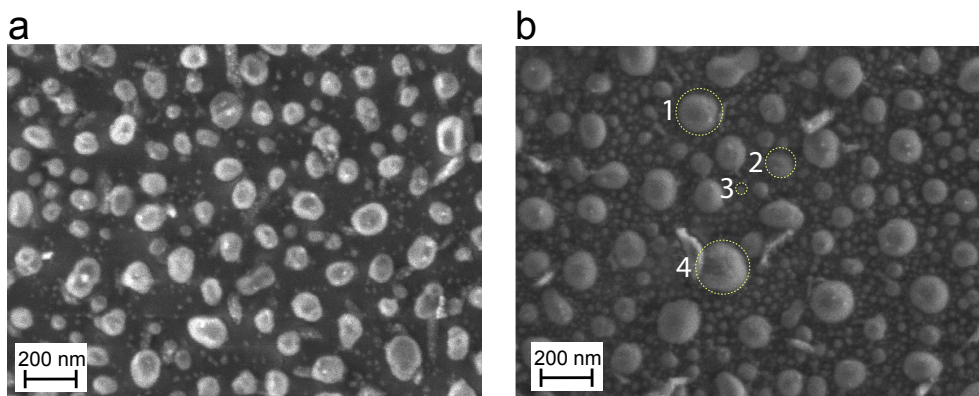
Figure 3: Scanning electron microscope images of AgNPs on the glass substrate. The scale bar is 200 nm. The size distribution of AgNPs before (a) and after laser exposure (b). AgNPs in (b) varing from 10 to 200 nm (1 - 155 nm, 2 - 105 nm, 3 - 20 nm, 4 - 200 nm).
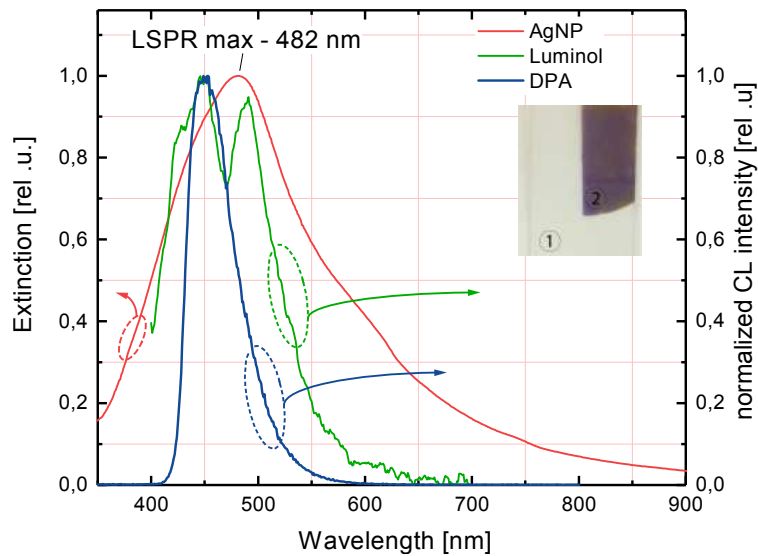
Figure 4: The extinction spectra overlap of AgNPs obtained via PVD with subsequent thermal annealing/laser exposure (red curve) with the chemiluminescence (CL) emission spectra of: luminol (green curve) and DPA (blue curve). The inset shows a photograph of the cover-glass (1) partially covered with AgNPs (2). All spectra are normalized. The arrows on the curves point towards of the corresponding axis.
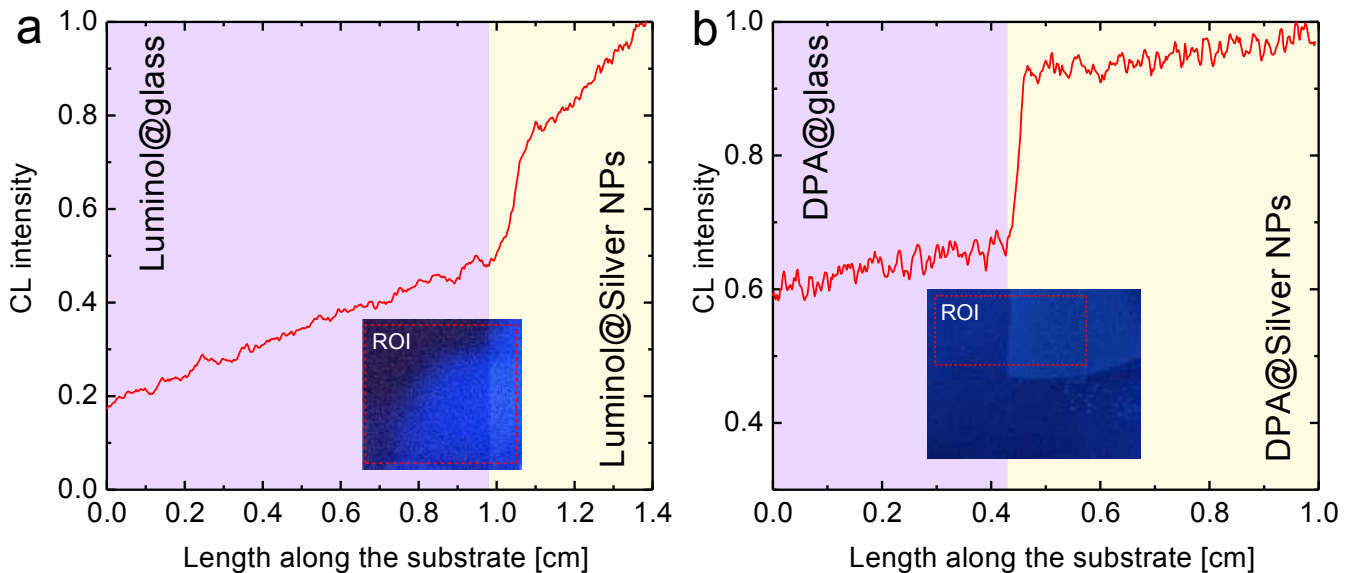
Figure 5: Distribution of chemiluminescence intensities over the indicated regions of interest (ROI). Red curves represent the chemiluminescence intensity integrated over the vertical axes and plotted against the horizontal axes of the corresponding chemiluminescent images. The jumps at the borders of the dedicated silver metasurfaces are clearly seen both in the pictures and in the plots. The plots background colors are used to guide the eyes. Luminol (a) and DPA (b).
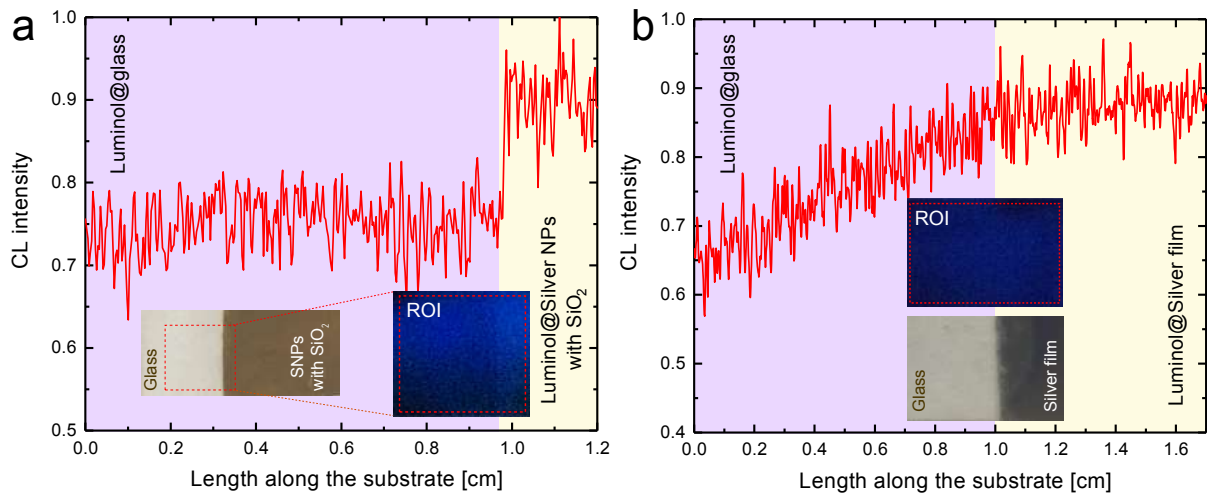
Figure 6: Distribution of chemiluminescence intensities over the indicated ROI for luminol on the dedicated silver meta-surface covered by a 2 nm thick SiO_2 spacer (a) and on the silver film that have plasmon resonances detuned from the chemiluminescence bands of luminol (b). The insets show also the images of the substrates before the luminol addition.
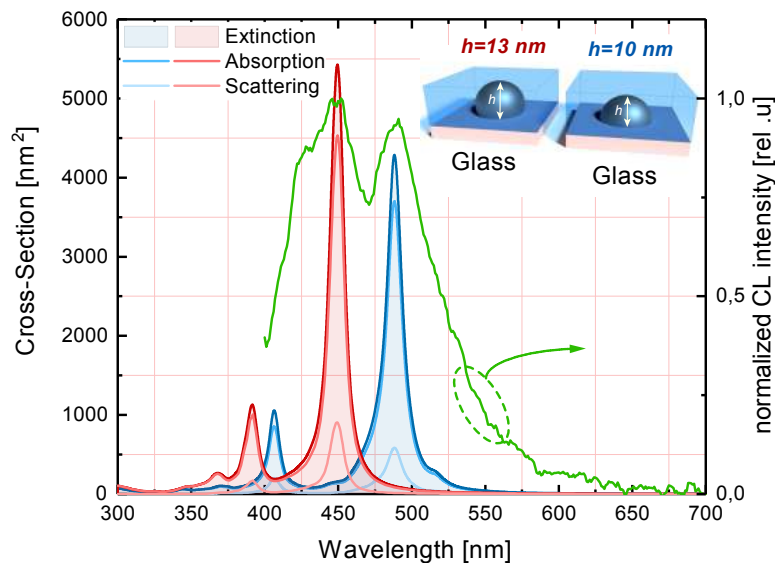
Figure 7: The overlap between the normalized chemiluminescence intensity spectra of luminol solution (green line) and the calculated extinction spectra of AgNPs supported on different substrates and submerged into luminol solution. Extinction cross-section spectra of AgNPs with $h = 13$ nm for the enhancement of luminol chemiluminescence emission band at 452 nm and with $h = 10$ nm for the luminol band at 489 nm. The diameters of AgNPs in both cases are 20 nm. The 3D models of silver nanoparticles placed on the respective substrates and submerged into the luminol solution are illustrated in the inserts. The arrow on the green curve points towards of the corresponding axis.
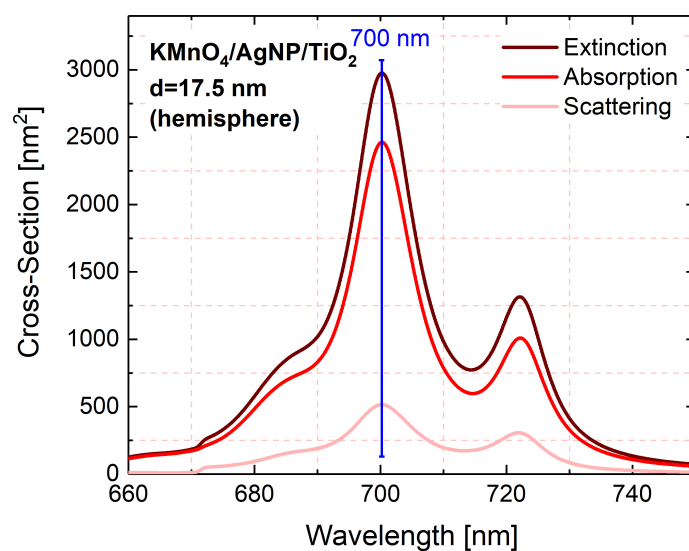
Figure 8: Calculated absorption, scattering and extinction cross-section spectra of the silver nanoparticles deposited on the TiO$_2$ substrate. The diameter of the hemisphere is $d = 17.5$ nm.
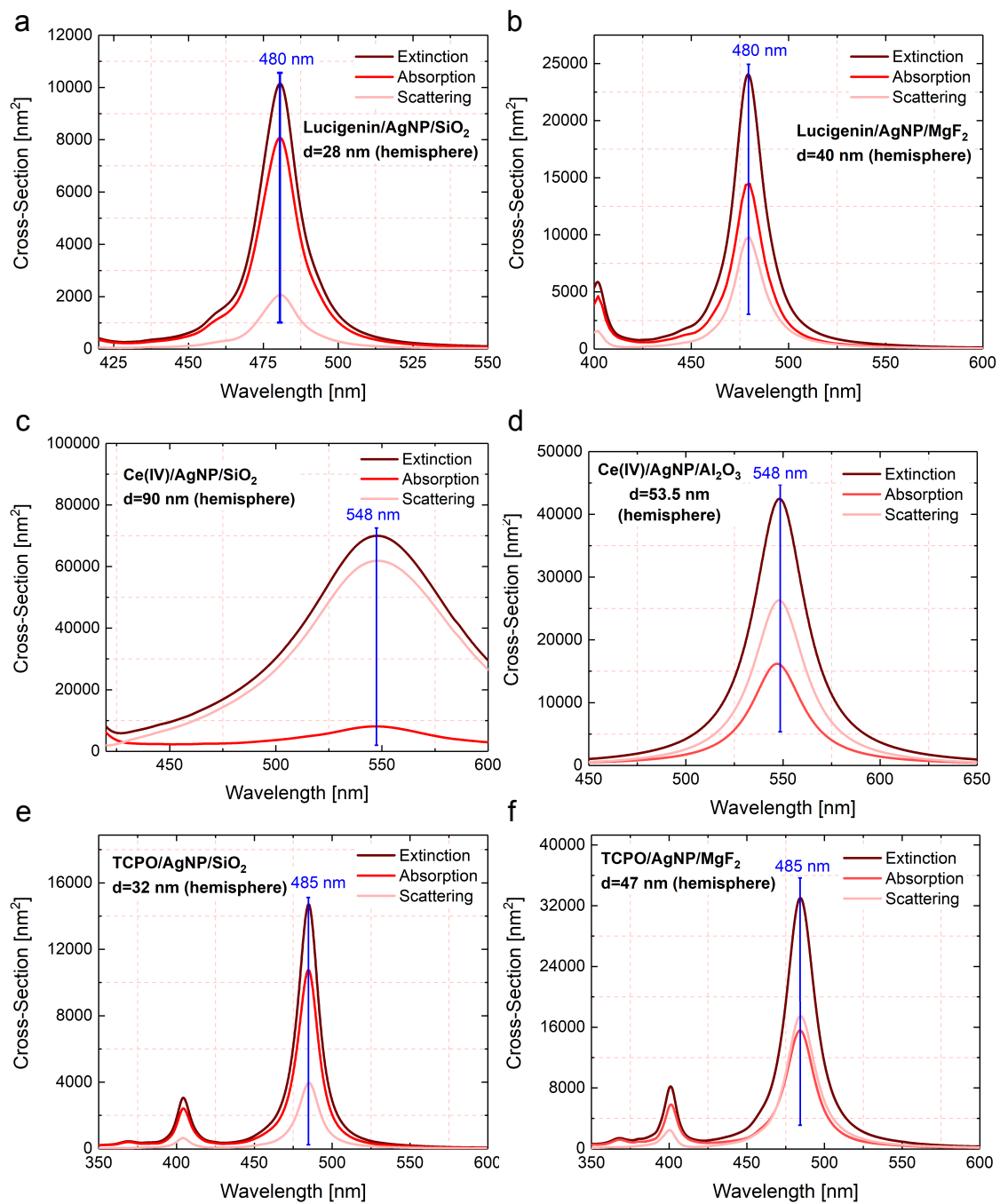
Figure 9: Calculated absorption, scattering and extinction cross-section spectra of the silver nanoparticle: (a) deposited on the SiO$_2$ substrate for Lucigenin. The diameter of hemisphere is d = 28 nm. (b) the silver nanoparticle on the MgF$_2$ substrate with diameter of 49 nm for Lucigenin system; (c) deposited on the SiO$_2$ substrate for Ce (IV). The diameter of hemisphere is d = 90 nm. (d) the silver nanoparticle on the Al$_2$O$_3$ substrate (d = 53.5 nm); (e) deposited on the SiO$_2$ substrate for TCPO system. The diameter of hemisphere is 32 nm. (f) the silver nanoparticle on the MgF$_2$ substrate with diameter of 47 nm for overlapping with TCPO chemiluminophore.

appendix B

Differential extinction of vibrational molecular overtone transitions with gold nanorods and its role in surface enhanced near-IR absorption (SENIRA)

DALER R. DADADZHANOV,[1,2,3] (ID) **TIGRAN A. VARTANYAN,[1]** AND **ALINA KARABCHEVSKY[2,3,*]** (ID)

[1]*ITMO University, 49 Kronverksky pr., St. Petersburg 197101, Russia*
[2]*School of Electrical and Computer Engineering, Ben-Gurion University of the Negev, Beer-Sheva, 8410501, Israel*
[3]*Center for Quantum Science & Technology, Ben-Gurion University of the Negev, Beer-Sheva 8410501, Israel*
[*]*alinak@bgu.ac.il*

Abstract: Resonant coupling between plasmonic nanoantennas and molecular vibrational excitations is employed to amplify the weak overtone transitions that reside in the near-infrared. We explore for the first time the differential extinction of forbidden molecular overtone transitions coupled to the localized surface plasmons. We show a non-trivial interplay between the molecular absorption enhancement and suppression of plasmonic absorption in a coupled system. When the resonance conditions are met at 1.5 μm, two orders of magnitude enhancement of differential extinction as compared to the extinction of the same amount of free probe molecules is achieved. Our results pave a road toward a new class of surface enhanced near-infrared absorption-based sensors.

1. Introduction

Near-infrared (NIR) spectroscopy focuses on interaction of near-infrared radiation with matter and is an important analytical technique for detection and recognition of chemical substances based on vibrational modes of their molecular constituents in pharmaceutical analysis, food quality determination, non-destructive analysis of biological materials to name a few [1–3]. However, molecular overtone bands lying in the NIR spectral region are forbidden in harmonic oscillator approximations. Such bands arise only from the anharmonicity of molecular vibrations which is rather weak leading to the overtone bands with the absorption cross-section of an order of magnitude smaller than the fundamental modes of the same degree of freedom [4]. Nevertheless, recent numerical and experimental results demonstrated that the overtone molecular vibration of aniline and N-methylaniline can be detected utilizing a silicon nanostrip rib waveguide [5].

Here we explore for the first time the mechanism of local field enhancement in molecular overtones. The local field enhancement can be realized with plasmonic materials by means of collective oscillations of free electrons in form of extended surface plasmon-polariton (SPP) in thin metal films [6–11] or localized surface plasmon resonance (LSPR) in plasmonic nanoantennas [12–15]. Meanwhile, we explored the influence of extended surface plasmon on absorption by molecular overtones, and showed that 100 times enhancement can be achieved [16]. This enhancement was observed when the absorption band of the molecular vibration N-H was detuned from the plasmonic resonance. It should be mentioned that enhancement and localization of electromagnetic fields in the close proximity of nanoantennas depend on their material, size, shape and the surrounding media [12]. Previously we found that the electronegative gold nanospheres are readily adsorbed on the tapered microfiber and electrostatically bonded to

amine-based molecules. Despite the non-resonant condition between the gold nanospheres and the amine-based molecules, we showed that the enhancement of the integrated overtone absorption in diffuse light propagation depends on the concentration of nanospheres [17]. Very interesting results were reported in [18]. The authors prepared porous gold nanodiscs that possess a broad plasmon resonance in the near-infrared range. When a random array of such nanodiscs is covered by a thin film of a material possessing absorption bands in the same spectral region, enhanced absorption of the composite material may be observed. Very large, up to four orders of magnitude, enhancement claimed in [18] is due to the use of analyte in the form of a self-assembled monolayer. In this case analyte presents exclusively in hot-spot regions. In general case, analyte occupies much larger volumes where the field enhancement is lower. Hence, the overall enhancement becomes lower as well. Despite this experimental observation of surface enhanced near-infrared absorption (SENIRA) of molecular overtones with plasmonic nanoantennas, this effect was not explored theoretically. The first work related to coupling of vibrational mode and plasmonic dipole oscillation of gold nanorods was theoretically implemented using a homogeneous weakly absorbing medium [19].

In this work we theoretically explore yet unclear possibility to enhance absorption by molecular overtone transitions in the near-field of plasmonic nanoantennas such as gold nanorods (GNRs) due to the combination of localized plasmon resonance and lightning rod effect [20]. Below we show that when the resonance conditions are met at 1.5 μm the differential extinction due to the excitation of overtones of N-H and C-H stretching modes can be enhanced by two orders of magnitude as compared to the ordinary extinction of the same amount of molecules.

2. Theoretical model

Figure 1 shows the system we study. Weakly absorbing medium, described by the complex permittivity of N-Methylaniline molecule, encapsulates a gold nanorod and nanoellipsoid in a homogeneous shell-like manner. The incident beam is directed perpendicular to the gold nanoparticles as indicated by vector $\mathbf{k}$ and polarized along the gold nanoparticles.
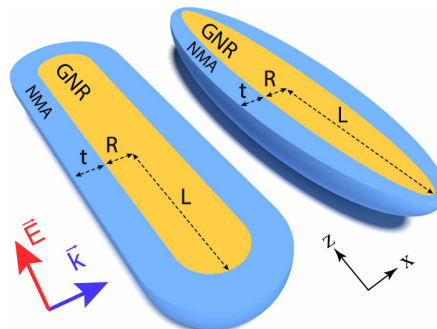
Fig. 1. Schematics of systems with gold nanorods (left) studied in numerical simulations and nanoellipsoids (right) used in the analytical model. The shells are made of N-Methylaniline (NMA). L and R are semi-major and semi-minor axises of gold nanoparticles respectively, while t is the thickness of molecular shells. The incident wave is polarized along the rod.

We study the contribution of GNR parameters in effect of SENIRA by molecular overtones. For this we built an analytical model of a confocal ellipsoidal core-shell nanoparticle. In the framework of quasi-static approximation, we express the absorption, scattering, and extinction

cross-sections through the particle polarizability [21,22]

$$\alpha = \frac{v\left((\varepsilon_2 - \varepsilon_m)\left[\varepsilon_2 + (\varepsilon_1 - \varepsilon_2)\left(S^{(1)} - fS^{(2)}\right)\right] + f\varepsilon_2(\varepsilon_1 - \varepsilon_2)\right)}{\left(\left[\varepsilon_2 + (\varepsilon_1 - \varepsilon_2)\left(S^{(1)} - fS^{(2)}\right)\right]\left[\varepsilon_m + (\varepsilon_2 - \varepsilon_m)S^{(2)}\right] + fS^{(2)}\varepsilon_2(\varepsilon_1 - \varepsilon_2)\right)},\tag{1}$$

$$\sigma_{ext} = \sigma_{abs} + \sigma_{sc} = 4\pi k\,\mathrm{Im}\{\alpha\} + \frac{8\pi}{3}k^4\,|\alpha|^2,\tag{2}$$

where S^i (i=1,2) are the geometrical factors of the core and the shell in the direction of the polarization (Fig. 1); ϵ_1, ϵ_2, ϵ_m are the frequency-dependent dielectric permittivity function of the gold core, the molecular shell and surrounding media, correspondently; v is the full volume of the nanoparticle with the shell and f is the ratio of the inner core volume to v; k is the wavenumber in the medium defined as $2\pi/\lambda$.

As the input parameters we consider the core and shell semi-axises and the frequency-dependent dielectric permittivities of the metal core, the shell and the surrounding medium, which was considered to be air.

To calculate the absorption, scattering and extinction cross-section spectra of complex systems comprising gold nanoparticles and molecular shells we used 3D full-wave computational models implemented in the commercial software COMSOL Multiphysics 5.4. In particular, the wave optics module for electromagnetic waves in the frequency domain was utilized. We included the perfectly matched layer (PML) in the form of a physical domain to absorb all scattered light. Gold nanorods were modeled as cylinders capped by hemispheres on both sides. Dimensions of all elements are given in the text and figure captions. The incident field oscillates in the z-direction with a k-vector pointing in the x- direction as shown in Fig. 1. The absorption cross-section (σ_{abs}) was calculated by integrating the power loss density over the particle volume. The scattering cross-section (σ_{sc}) was derived by integrating the Poynting vector over an imaginary sphere around the particle. Extinction cross section is the sum of both. The complex refractive index of the gold was obtained from the experimental work of Johnson and Christy [23].

The N-Methylaniline (NMA) was chosen as a representative probe-molecule example of an organic molecule that possesses overtone bands in the NIR spectral range [24–26]. The absorption bands at wavelengths of 1494 nm and 1676 nm are associated with the first overtones of N-H and C-H stretching modes. These bands are accompanied by the anomalous dispersion regions calculated based on a measured absorption spectra k as it follows from the Kramers-Kronig relations (presented in Figure 7(d) in [24]).

3.   Results and discussion

First, we analyzed how the LSPR position depends on the analyte shell thickness, t. Since the enhanced near-field rapidly decays with the distance from the surface, effective interaction is possible here only at distances comparable to the nanoantenna dimensions. In addition, the aspect ratio of the nanoantenna should provide the resonant interaction between the longitudinal plasmon and an overtone excitation. Therefore, we choose the semi-minor axis of the gold nanoellipsoid as 5 nm, while varying the semi-major axis until the LSPR band overlaps with an overtone mode.

For this, we calculated extinction cross-sections of gold nanoellipsoids covered by thin shells of NMA in the form of confocal ellipsoids. Figure 2(a) shows the extinction cross-section of GNR as a function of the NMA shell thickness. The semi-major axis of the gold core is $L = 55.9$ nm that leads to the exact resonance with the first overtone of N-H mode when the shell thickness is $t = 20$ nm. Figure 2(b) shows the same dependence when the semi-major axis of the gold core is $L = 68.1$ nm that leads to the exact resonance with the first overtone of C-H mode when the shell thickness is $t = 20$ nm. The long wavelength shift of plasmon bands as a function
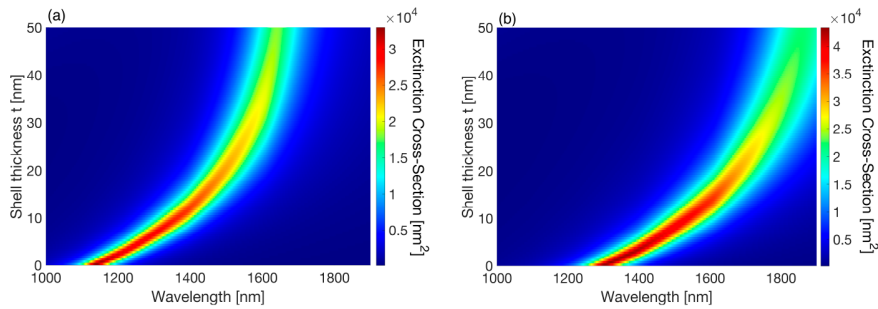
Fig. 2. Extinction cross-sections of gold nanoellipsoids with NMA shells of different thicknesses. (a) the semi-major axis of the gold core is $L = 55.9$ nm (b) the semi-major axis of the gold core is $L = 68.1$ nm. The semi-minor axis is $R = 5$ nm in both cases.

of the shell thickness t is rather strong at small shell thicknesses for $t < 40$ nm but saturates at shell thicknesses larger than $t > 40$ nm.

As proof-of-concept numerical simulations we built numerical model using COMSOL and show the tuning of the plasmon bands of GNR with the NMA overtone bands. Figure 3 shows calculated extinction (ECS), absorption (ACS) and scattering (SCS) cross-section of gold nanorods with NMA shell for $L = 49.9$ nm (Fig. 3(a)) and for $L = 60.6$ nm (Fig. 3(b)). The nanorod diameter is 10 nm. We choose the length of GNR such that it overlaps with the overtone bands of N-H located at 1494 nm and C-H located at 1676 nm. Considering the results presented in Fig. 3 one concludes that extinction is governed by absorption, while the scattering contribution is negligible.
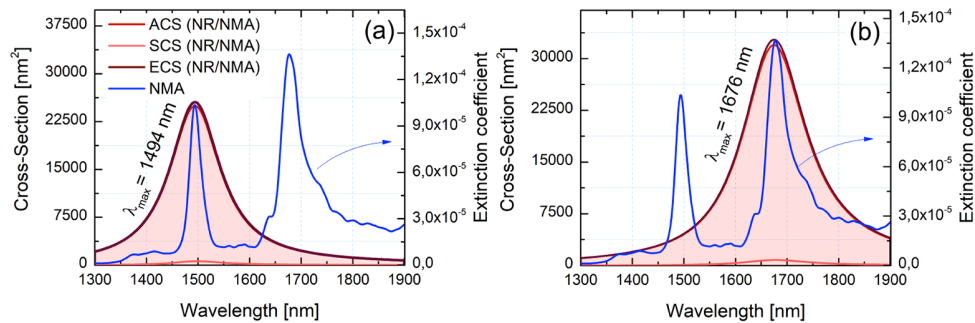
Fig. 3. Extinction (*brown*), absorption (*red*) and scattering (*pink*) cross-sections of gold nanorods with NMA shell. The nanorod diameter is set to 10 nm for (a) $L = 49.9$ nm, (b) $L = 60.6$ nm. The thickness of the NMA molecular shell is homogeneous and equals to $t = 20$ nm. Extinction coefficient of NMA (*blue*) is also shown for comparison.

The advantage of using GNR becomes evident when the concept of differential extinction is employed [16]. Experimentally, the differential absorption can be realized by comparing the extinction cross-section of a GNR surrounded by the analyte shell with that of a GNR surrounded by a shell of non-absorbing material that mimic only the mean value of the analyte's refractive index. Thus, the difference between cross-sections of absorbing and non-absorbing materials represents the influence of the analyte absorption and anomalous dispersion on the LSPR intensity and spectral position. On the other hand, it includes also the influence of the LSPR on the analyte absorption.

Quantitatively, *differential extinction*, DE, as [16,19]:

$$DE = \sigma_{ext}^{NR/NMA} - \sigma_{ext}^{NR/NMA^*}, \qquad (3)$$

where the first term $\sigma_{ext}^{NR/NMA}$ represents the extinction cross-section of GNR with NMA shell, while the second term σ_{ext}^{NR/NMA^*} represents the same value with NMA replaced by a dummy medium of constant dielectric permittivity. Figure 4 shows the calculated DE in spectral ranges of the first overtones of the N-H and C-H stretching modes. Interestingly, the sign of the wavelength dependent DE alternates in both cases.
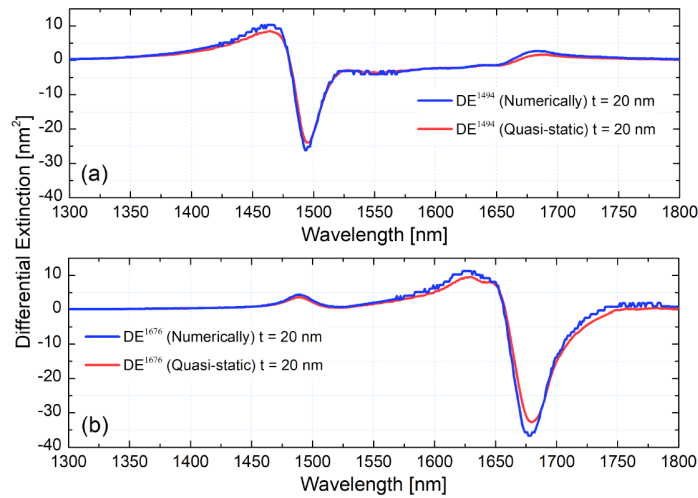
Fig. 4. Comparative analysis of differential extinction (DE) spectra of gold nanorod and nanoellipsoid with NMA shells: (a) with semi-major axes $L = 49.9$ (nanorod) and $L = 55.9$ nm (*nanoellipsoid*); (b) $L = 60.6$ (*nanorod*) and $L = 68.1$ nm (*nanoellipsoid*). Blue curves correspond to numerically calculated results (*nanorod*) while the red curves correspond to results obtained in the quasi-static approximation (*nanoellipsoid*)

Figure 4 shows the calculated DE in spectral ranges of the first overtones of the N-H and C-H stretching modes. Interestingly, the sign of wavelength dependent DE alternates in both cases.

We choose the aspect ratio of nanorods for the Fig. 4 as $L/R = 9.98$ and the aspect ratio of nanorods for the Fig. 4(b) as $L/R = 12.12$. Numerically calculated DEs (blue) are very well reproduced by the DEs obtained in the quasi-static approximation (red) (Eq.1) provided the aspect ratios of the GNRs are adjusted to match the plasmon resonance with the corresponding overtone ($L/R = 11.18$ Fig. 4(a) and $L/R = 13.62$ in Fig. 4(b)). It is important to note that in the case exact resonance between the plasmon in the GNR and the molecular overtone transition the sign of DE alternates. Contrary to that in the non-resonant case DE is strictly positive. It may be clearly seen in Fig. 4 for C-H overtone transition at 1676 nm when the plasmon in the nanorod is tuned on 1494 nm (Fig. 4(a)) and for N-H overtone transition at 1494 nm when the plasmon in the nanorod is tuned on 1676 nm.

To explore the role of GNRs in the detectivity enhancement of small amounts of NMA, extinction cross-sections of pure NMA shells (without GNR) were compared with the DE. Figure 5 shows the dependence of both values on the NMA shell thickness. When the resonance conditions are met, the DE values exceed the extinction cross-sections of the pure NMA shells by two orders of magnitude. In particular, the first overtone of N-H stretching mode located at 1494 nm is enhanced 114 times, while the first overtone of C-H stretching mode located at 1676 nm is enhanced 135 times. Figure 5(a) shows variations in cross-sections versus shell thickness

for λ = 1494 nm and the GNR semi-major axis is equal 49.9 nm. The resonance conditions for the plasmon excitation are met when the shell thickness is equal to 20 nm. Similarly, the optical properties in the form of ECS and ACS as function of the shell thickness are presented in Fig. 5(b) whereby λ = 1676 nm with GNR semi-major axis L = 60.6 nm.
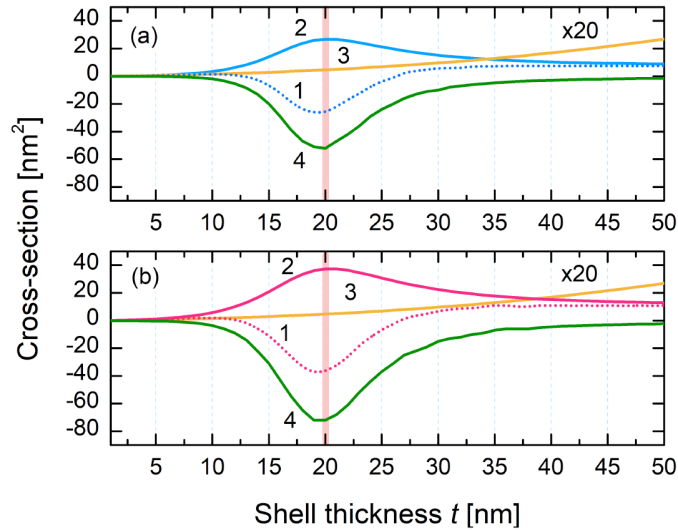
Fig. 5. (a) Optical cross-section as function of shell thickness of NMA: (1) differential extinction, (2) absorption cross-section of NMA shell encapsulating GNR, (3) extinction cross-section of the NMA shell without the GNR, and (4) the difference between ACSs of the GNR -with and -without the NMA shell GNR semi-major axis (a) L is 49.9 nm and the wavelength is set to 1494 nm. Absorption cross-section of the NMA shell when the GNR is absent is multiplied by 20. (b) same graphs as in subplot (a) for the case when the wavelength is set to 1676 nm, while L is 60.6 nm.

Enhanced absorption in the NMA shell due to the plasmon near-field is accompanied by reduced absorption in the GNR due to the screening effect [27]. As a matter of fact, neither enhanced absorption in the shell nor the reduced absorption in the core can be observed in the far-field separately. However, they combine favorably leading to very large DE values.

DE dependence on both: the NMA thickness and the incident radiation wavelength based on analytical model is presented in Fig. 6. In both plots the dark curve corresponds to the maxima of the LSPR. The vertical dashed lines mark the location of overtone bands, while the horizontal dashed lines correspond to NMA thickness of 20 nm that leads to coincidence of the LSPR in the chosen nanorod with the corresponding overtone band. Inspection of Fig. 6 to the conclusion that the main features of DE already noted in particular cases presented in Fig. 4 and Fig. 5 namely, that the largest absolute value of DE is obtained at the resonance and the sign of this largest DE value is negative are confirmed.
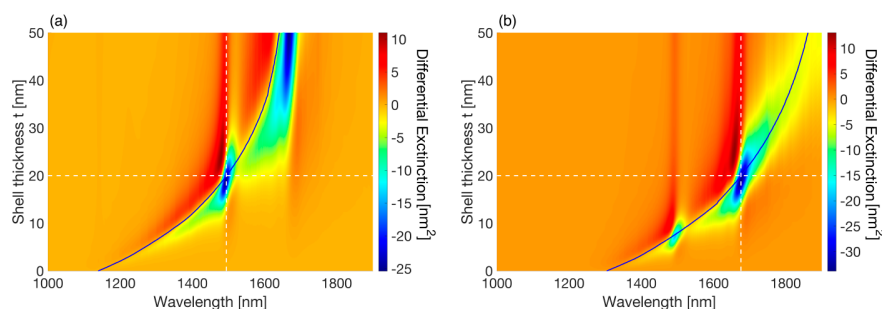
Fig. 6. (a) Differential extinction (DE) values are given as the functions of the NMA shell thickness and the incident radiation wavelength for GNR with semi-major axis of: $L = 55.9$ nm (a) and $L = 68.1$ nm (b), respectively. The vertical dashed lines show the position of two overtone bands, while the horizontal dashed lines mark the shell thickness ($t = 20$ nm) that leads to tuned plasmon resonance with the corresponding overtone band. The dark curve is drawn through the maxima of the plasmon resonances.

4.   Conclusion

In conclusion, we explored for the first time the *differential extinction* of forbidden molecular overtone transitions coupled to the localized surface plasmons. We showed that the differential extinction provides the SENIRA with two orders of magnitude enhancement. The non-trivial consequence of the simulations is that the enhanced absorption in the analyte is accompanied by the reduced absorption in the gold nanorods that overruns the absorption enhancement of the analyte and forms the signal that may be readily sensed in the far-field. Hence, local field enhancement of nanoparticle can result in the considerable sensitivity improvements of overtone spectroscopy in the NIR spectral range.

Disclosures

The authors declare that there are no conflicts of interest related to this article.

References

1. H. Cen and Y. He, "Theory and application of near infrared reflectance spectroscopy in determination of food quality," Trends Food Sci. Technol. **18**(2), 72–83 (2007).
2. M. Manley, "Near-infrared spectroscopy and hyperspectral imaging: non-destructive analysis of biological materials," Chem. Soc. Rev. **43**(24), 8200–8214 (2014).
3. M. Jamrógiewicz, "Application of the near-infrared spectroscopy in the pharmaceutical technology," J. Pharm. Biomed. Anal. **66**, 1–10 (2012).
4. B. C. Smith, *Infrared spectral interpretation: a systematic approach* (CRC press, 2018).
5. A. Katiyi and A. Karabchevsky, "Si Nanostrip Optical Waveguide for On-Chip Broadband Molecular Overtone Spectroscopy in Near-Infrared," ACS Sens. **3**(3), 618–623 (2018).

6. S. A. Maier, *Plasmonics: Fundamentals and Applications, Springer, New York, New York, 2007.* (Springer Science and Business Media, 2007).

7. V. Klimov, *Nanoplasmonics* (Pan Stanford, 2014).

8. A. Karabchevsky, O. Krasnykov, M. Auslender, B. Hadad, A. Goldner, and I. Abdulhalim, "Theoretical and experimental investigation of enhanced transmission through periodic metal nanoslits for sensing in water environment," Plasmonics **4**(4), 281–292 (2009).

9. A. Karabchevsky, S. Karabchevsky, and I. Abdulhalim, "Fast surface plasmon resonance imaging sensor using radon transform," Sens. Actuators, B **155**(1), 361–365 (2011).

10. A. Karabchevsky, S. Karabchevsky, and I. Abdulhalim, "Nanoprecision algorithm for surface plasmon resonance determination from images with low contrast for improved sensor resolution," J. Nanophotonics **5**(1), 051813 (2011).

11. A. Karabchevsky, J. S. Wilkinson, and M. N. Zervas, "Transmittance and surface intensity in 3d composite plasmonic waveguides," Opt. Express **23**(11), 14407–14423 (2015).

12. A. Karabchevsky, A. Mosayyebi, and A. V. Kavokin, "Tuning the chemiluminescence of a luminol flow using plasmonic nanoparticles," Light: Sci. Appl. **5**(11), e16164 (2016).

13. S. I. Maslovski and C. R. Simovski, "Purcell factor and local intensity enhancement in surface-enhanced raman scattering," Nanophotonics **8**(3), 429–434 (2019).

14. C. Simovski, "Circuit model of plasmon-enhanced fluorescence," in *Photonics*, vol. 2 (Multidisciplinary Digital Publishing Institute, 2015), pp. 568–593.

15. Y. Galutin, E. Falek, and A. Karabchevsky, "Invisibility cloaking scheme by evanescent fields distortion on composite plasmonic waveguides with si nano-spacer," Sci. Rep. **7**(1), 12076 (2017).

16. A. Karabchevsky and A. Shalabney, "Strong interaction of molecular vibrational overtones with near-guided surface plasmon polariton," in *Optical Sensing and Detection IV*, vol. 9899 (International Society for Optics and Photonics, 2016), p. 98991T.

17. A. Karabchevsky, A. Katiyi, M. I. M. Bin Abdul Khudus, and A. V. Kavokin, "Tuning the Near-Infrared Absorption of Aromatic Amines on Tapered Fibers Sculptured with Gold Nanoparticles," ACS Photonics **5**(6), 2200–2207 (2018).

18. W. C. Shih, G. M. Santos, F. Zhao, O. Zenasni, and M. M. P. Arnob, "Simultaneous chemical and refractive index sensing in the 1-2.5 μm near-infrared wavelength range on nanoporous gold disks," Nano Lett. **16**(7), 4641–4647 (2016).

19. D. R. Dadadzhanov, A. Karabchevsky, and T. Vartanyan, "Vibrational overtones spectroscopy enabled by plasmonic nanoantennas," in *Proceedings of SPIE - The International Society for Optical Engineering*, vol. 10722 (2018), p. 85.

20. M. Li, S. K. Cushing, and N. Wu, "Plasmon-enhanced optical sensors: a review," Analyst **140**(2), 386–406 (2015).

21. C. F. Bohren and D. R. Huffman, *Absorption and scattering of light by small particles* (John Wiley and Sons, 2008).

22. K. L. Kelly, E. Coronado, L. L. Zhao, and G. C. Schatz, "The optical properties of metal nanoparticles: the influence of size, shape, and dielectric environment," J. Phys. Chem. B **107**(3), 668–677 (2003).

23. P. B. Johnson and R. W. Christy, "Optical constants of the noble metals," Phys. Rev. B **6**(12), 4370–4379 (1972).

24. A. Katiyi and A. Karabchevsky, "Figure of merit of all-dielectric waveguide structures for absorption overtone spectroscopy," J. Lightwave Technol. **35**(14), 2902–2908 (2017).

25. A. Karabchevsky and A. V. Kavokin, "Giant absorption of light by molecular vibrations on a chip," Sci. Rep. **6**(1), 21201 (2016).

26. A. Karabchevsky, A. Katiyi, M. I. M. Bin Abdul Khudus, and A. V. Kavokin, "Tuning the near-infrared absorption of aromatic amines on tapered fibers sculptured with gold nanoparticles," ACS Photonics **5**(6), 2200–2207 (2018).

27. N. T. Fofang, T.-H. Park, O. Neumann, N. A. Mirin, P. Nordlander, and N. J. Halas, "Plexcitonic nanoparticles: plasmon-exciton coupling in nanoshell-J-aggregate complexes," Nano Lett. **8**(10), 3481–3487 (2008).

appendix C

Lattice Rayleigh Anomaly Associated Enhancement of NH and CH Stretching Modes on Gold Metasurfaces for Overtone Detection

Daler R. Dadadzhanov [1,2,*] [ID], **Tigran A. Vartanyan** [1] [ID] and **Alina Karabchevsky** [2,*] [ID]

[1] School of Photonics, Center of Information Optical Technology, ITMO University, 49 Kronverksky pr., St. Petersburg 197101, Russia; tigran.vartanyan@mail.ru

[2] School of Electrical and Computer Engineering, Ben-Gurion University of the Negev, Beer-Sheva 8410501, Israel

* Correspondence: dadadzhanov@itmo.ru (D.R.D.); alinak@bgu.ac.il (A.K.)

Abstract: Molecular overtones stretching modes that occupy the near-infrared (NIR) are weak compared to the fundamental vibrations. Here we report on the enhancement of absorption by molecular vibrations overtones via electromagnetic field enhancement of plasmonic nanoparallelepipeds comprising a square lattice. We explore numerically, using finite element method (FEM), gold metasurfaces on a transparent dielectric substrate covered by weakly absorbing analyte supporting N-H and C-H overtone absorption bands around 1.5 μm and around 1.67 μm, respectively. We found that the absorption enhancement in N-H overtone transition can be increased up to the factor of 22.5 due to the combination of localized surface plasmon resonance in prolonged nanoparticles and lattice Rayleigh anomaly. Our approach may be extended for sensitive identification of other functional group overtone transitions in the near-infrared spectral range.

Keywords: metasurface; localized surface plasmon resonance; surface-enhanced near-infrared absorption; overtone spectroscopy

1. Introduction

Near-infrared (NIR) spectroscopy is a powerful method of non-destructive material analysis based on the excitation of overtones and combination bands of molecular vibrations [1–4]. An important advantage of NIR spectroscopy over the spectroscopes in the longer wavelengths is the availability of effective radiation sources and sensitive detectors [5,6]. On the other hand, NIR transitions, being forbidden in the harmonic approximation, are much weaker than the transitions corresponding to the fundamental vibration modes [7,8]. Hence, to be applicable in small sample analysis, NIR absorption should be substantially enhanced. Due to this fact, searching for the means of NIR absorption amplification has recently become the focus of many studies [4,9–16].

Localized surface plasmon resonance (LSPR) excited in metal nanoparticles has been known to provide substantial absorption enhancement by nearby molecules [17–19]. Previously, we have shown that the size and the aspect ratio of prolate gold nanospheroids may be chosen in such a way that their LSPR bands overlap with the first-order overtones of C-H and N-H stretching modes of organic substances [20]. Next, the size and the shape of a rod-like gold nanoparticle was optimized to achieve the maximum overtone absorption enhancement [21]. However, using the isolated gold nanoparticles implies that only a very small fraction of the analyte is placed in the amplified near-field. This circumstance limits the overall enhancement provided by LSPR. To get the most of the plasmon field amplification, metal nanoparticles are to be arranged in a dense array forming a metasurface. Consequently, the larger portion of the analyte molecules may be placed in the regions of enhanced

near-field [22]. Moreover, an electromagnetic interaction between the adjacent nanoparticles leads to an additional mechanism of local field enhancement when the conditions for the Rayleigh anomaly are fulfilled [23–32]. Fabrication of nanoparticle arrays of required density is feasible via electron beam lithography (EBL) [33,34], although the shapes of the nanoparticles defined by EBL on a substrate are closer to the nanoscale parallelepipeds (NPs) rather than to the nanorods or nanospheroids.

Therefore, this study is devoted to planar metasurfaces consisting of nanoparallelepipeds (NPs) that can be fabricated easily and prepared specifically for overtone detection in near-infrared. The proposed structure utilizes a combination of localized plasmon resonance in isolated gold NP with Rayleigh anomalies of their periodic array. By incorporating the plasmonic metasurface into a weakly absorbing organic medium, a 22.5-fold enhancement of the first overtone of N-H stretching mode in the NIR has been demonstrated for the first time. Application of the designed gold metasurface may be beneficial in biomedicine [35], non-destructive testing [36], and food quality analysis [37–39].

2. Numerical Model

To obtain a realistic model we consider an infinite array of gold nanoantennas in the form of parallelepipeds arranged in a square lattice on a dielectric substrate and covered by a thin layer of analyte molecules. To be specific, as a probe molecule, we work with the well-known organic compound and derivative of Ammonia, N-Methylaniline ($C_6H_5NH(CH_3)$) [9,40]. Recently, we have thoroughly studied the optical properties of N-Methylaniline in bulk samples and, using Kramers–Kronig relations, obtained its complex dielectric permittivity in the NIR [4,9,10,41]. The absorption bands (Figure 1) at wavelengths of 1494 and 1676 nm are associated with the first overtones of N-H and C-H stretching modes and accompanied by the anomalous dispersion.
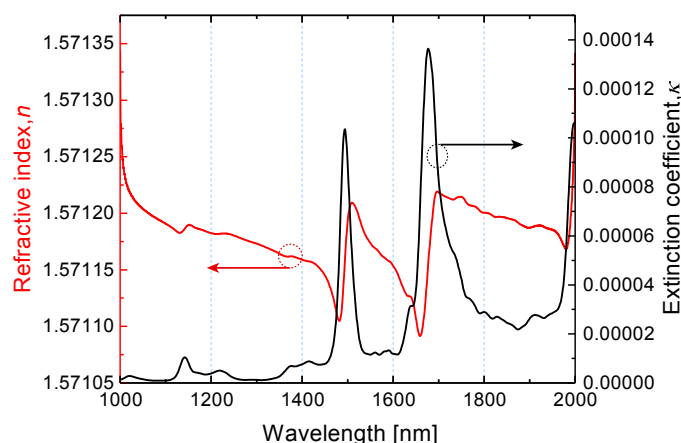
Figure 1. Dispersion characteristic of the N-Methylaniline (NMA) molecules as a function of the wavelength in the near-infrared.

Numerical simulations via finite-element-method (FEM) were conducted in the COMSOL Multiphysics environment. The capabilities of the software allow us to calculate plasmonic properties of gold metasurface of studied geometry with high accuracy based on a straightforward solution of Maxwell's equations under certain boundary conditions. Here, perfectly matching layers are used to absorb reflected and transmitted light from the sample when the linearly polarized wave (E_x) is launched perpendicular to the $x - y$ plane through the excitation port placed immediately under the top of a perfectly matched layer. This model also comprises an air gap, as well as the analyte layer and a transparent BK7 glass substrate (see Figure 2). A 2D periodic array of NPs illustrated in Figure 2a was modeled using the Floquet type boundary conditions that were imposed on the side walls of an elementary cell shown in Figure 2b. More details on the model description are given in [22]. Thus, the gold metasurface is modeled as a square lattice of prolonged NPs with variable length L, while width w and height h were fixed and equal to 20 nm (depicted in Figure 2a,b). The dispersion

of dielectric properties of gold was obtained from the experimental work of Johnson and Christy for bulk material [42] without modification because the nanoparticles dimensions are large enough for the possible changes to be insignificant in our case [43,44]. Dispersion of BK7 used as a substrate was taken from [45].

Since we used the periodic boundary conditions, the results are strictly valid for the infinite structures, while all the real structures are finite. There are several studies devoted to the relation between the optical properties of finite structures of different sizes and the corresponding infinite structure [46–48]. Although there is no general solution, in most cases several hundreds of periods are enough for the convergence.

To facilitate the comparison of the obtained theoretical results with the future experimental data, we introduce the notion of '*Differential transmission*', which helps to explore the effect of the gold metasurface on the overtone absorption intensity. The differential transmission is computed as a difference between transmissions of analyte and immersion oil films of the same thickness. Related notions of differential extinction and differential absorption were previously introduced in [21,41]. A transparent dielectric film characterized by a negligible dispersion was used as a reference for the differential transmission calculations. The refractive index of this film was chosen to be the same as the mean value of the N-Methylaniline (NMA) refractive index in the actual spectral range (n_{av} = 1.5712). Experimentally, such a film may be readily realized utilizing an appropriate immersion oil. Transmission spectra of plane parallel films without gold nanoparticles were calculated analytically [49].
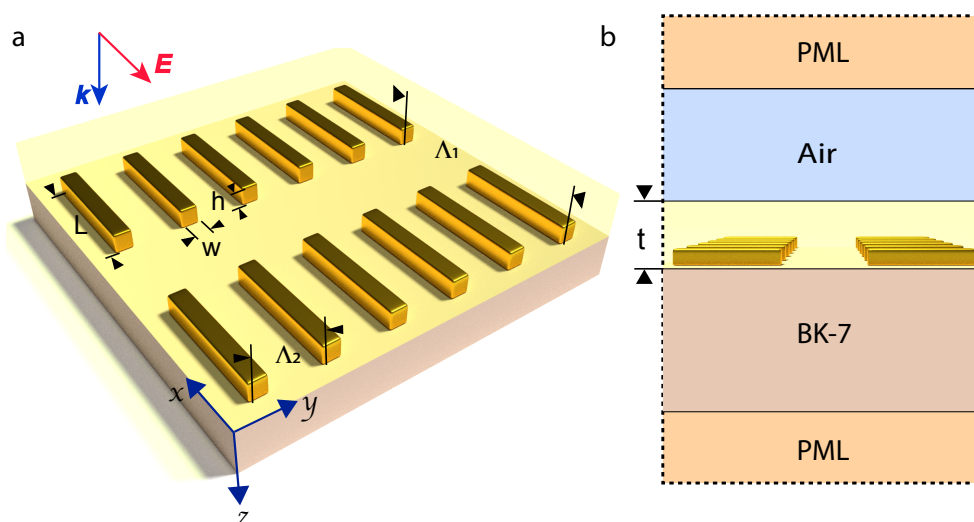
Figure 2. (**a**) 3D schematics of the gold metasurface modeled in COMSOL Multiphysics software. The width and height of gold nanoparallelepipeds (NPs) in the array are of $w = h = 20$ nm, while the length is varied. The longitudinal and transverse lattice constants are defined as Λ_1 and Λ_2. t designates the analyte film thickness. The incident light propagation direction k and polarization E are also shown. (**b**) Schematics of 2D cross-section of the model. Furthermore, the gold metasurface submerged into the analyte layer, the structure involves a BK7 glass substrate and an air layer with refractive index n = 1. The sample is placed between perfectly matched layers (PML).

3. Optimization of the Metasurface

When the lattice periods become comparable to the sizes of the individual nanoantennas, plasmon resonances start to interact with the lattice resonances. Hence, the optimization procedure becomes very complex. To facilitate the optimization, we study the Rayleigh anomaly that corresponds to the first diffraction order which starts to propagate into the substrate with the refractive index $n = 1.5$ at the wavelength of N-H overtone $\lambda = 1494$ nm (in vacuum). The rough approximation of the lattice constant is $\Lambda_1 = \lambda/n$, as shown in Figure 2a, gives a value of 1 μm. Next, the length of

the nanoantenna is to be chosen in such a way that the effective polarizability of the nanoantennas comprising the metasurface α^* reaches its maximum value. According to the well-developed theory of diffractively coupled localized plasmon resonances in the framework of the coupled dipole approximation (CDA) [24], α^* may be calculated as follows:

$$\alpha^* = \frac{1}{\frac{1}{\alpha} - S} \tag{1}$$

where α denotes the polarizability of an isolated nanoantenna that depends solely on its size and shape (at the fixed wavelength). The dipole sum S accounts for the dipole-dipole interaction between nanoantennas and only depends on the lattice periods Λ_1, Λ_2 (see Figure 2a). According to Equation (1) α^* reaches its maximum when the real parts of S and α^{-1} are equal. From the calculated results presented in [24], we learn that S is very small anywhere but at the narrow window around $\frac{\Lambda_2}{\lambda} \approx 1$ it has a maximum. On the other hand, the LSPR wavelength of NP of a fixed cross-section is a monotonic function of its length as it may be seen in Figures 3 and A1. Hence, to maximize the effective polarizability at the wavelength of the molecular overtone transition, the length of the nanoantenna should vary together with the lattice periods. The length of the resonance antenna is expected to have a minimum as a function of the lattice period. Considering this, we performed the numerical simulation and found the structures of gold metasurfaces with certain LSPR bands optimized for sensing of functional groups overtone transitions at $\lambda = 1494$ nm and $\lambda = 1676$ nm.
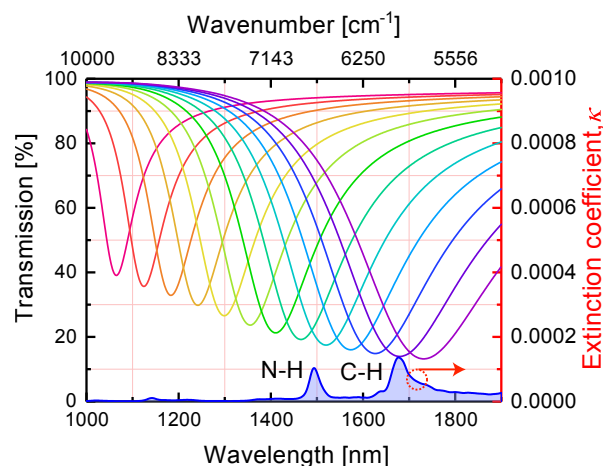

Figure 3. Calculated transmission spectra of gold metasurfaces with NPs of lengths L varied from 100 (crimson curve) to 220 (purple curve) nm in 10 nm steps, whereas lattice periods were fixed at $\Lambda_1 = 400$ nm and $\Lambda_2 = 200$ nm. The extinction coefficient of NMA is shown below the transmission curves. The gold metasurface was embedded in NMA with a thickness of 100 nm.

4. Dependence of the Collective LSPR Spectral Position on the Gold Metasurface Parameters

The dependence of the transmission dip location on the nanoparticle length has been investigated. We performed the simulations for the light polarized along the length of gold NPs (x-axis) at normal incidence. Figure 3 shows the transmission spectra of gold metasurfaces with fixed lattice periods and varying lengths of nanoantennas. In close analogy to the well-known dependence of the LSPR spectral position on the aspect ratio of an isolated prolate spheroid, the dip in transmission shifts toward the long-wavelength range when the NPs length L grows. At particular values of length L the transmission dip is defined by collective LSPR overlaps with and couples to the N-H and C-H overtone absorption bands in near-infrared. The transmission dip location depends linearly on the NPs length L, as can be seen in Figure A1.

5. Near-Field Enhancement

In this section, we analyze the distribution of the enhanced near-field around the gold NP. The incident field is polarized along the *x*-axis while the lattice constants are fixed at Λ_1 = 400 nm and Λ_2 = 200 nm, respectively. Figure 4 shows the near-field distribution around one of the gold nanoantennas in the array when the collective LSPR of the metasurface is tuned to coincide with one of the analyte overtones at 1494 nm. The top (a) and side (b) views are both shown in Figure 4. Electric near-field polarized along the long axis of the NP exhibits strong enhancement and localization around the antenna tips. Figures 4c,d show the corresponding field distributions along the *x* and *z* axes. We note that the calculated results shown in Figure 4 demonstrate the lightning-rod effect (subplots a, b) as well as the rapid near-field decay (subplots c, d) inside the homogeneous layer of organic molecules and the dielectric substrate. Indeed, the length of NP is more than eight times larger than its width and height. Hence, the main prerequisite for the field concentration at the sharp edges of the nanoparticle and the lightning-rod effect observation is fulfilled. Large jumps of the electric field at the metal surfaces seen in Figure 4 is due to the large value of the real part of gold permittivity at λ = 1494 nm (about minus one hundred).
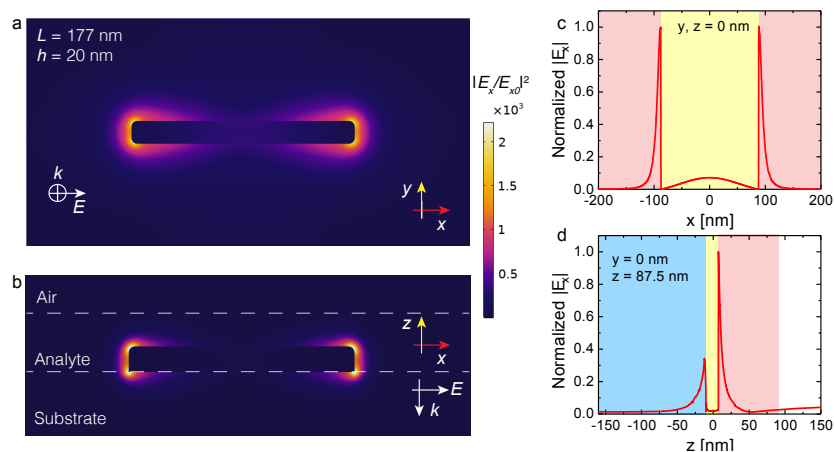

Figure 4. The electric field enhancement $|E_x/E_{x0}|^2$ distribution around the gold NP in an array (Λ_1 = 400 nm and Λ_2 = 200 nm) surrounded by NMA layer: top view (**a**) and side view (**b**). Normalized electric field distribution along the *x*-axis goes through the NP center (**c**); the same for the *z*-axis (**d**) at *x* = 87.5 nm. Color encoding in (**c**,**d**): blue—the BK-7 glass substrate, yellow—gold nanoparticle, red—thin layer of NMA layer, white—air. The excitation wavelength is λ = 1494 nm. The colorbar corresponds for colormaps in (**a**,**b**) subplots.

## 6. Differential Transmission Computations

Computation of the differential transmission (DT) spectra is an important step in metasurface design for sensing purposes where the crucial feature is the detection of a small amount of analyte. In particular, the enhanced absorption of the analyte molecules in the near-field of the metasurface is still much smaller than the own absorption of the metasurface in the absence of molecules. In this regard, to reveal the contribution of the gold metasurface, the NPs absorption excluding the presence of molecules must be subtracted from the measured absorption with molecules. Furthermore, it is important to take into account that the metasurface absorption spectra shift when the permittivity of surrounding changes. Therefore, measurement of the metasurface transmission in air seems infeasible. Instead, the metasurface transmission in contact with a thin film of a transparent material should be considered. The refractive index (RI) of this material should be chosen close to the RI mean value of analyte in the actual spectral range and the film thickness should be the same as that of an analyte. Based on that, calculation of DT becomes a reliable way to reveal the presence of analyte and the spectral position of its absorption bands [22]. Figure 5 displays an example of the DT spectrum. Compared to what is shown in the literature [50,51], the plasmon enhanced absorption DT spectrum

demonstrates complex behavior (see Figure 5). DT changes its sign as a result of combined action of absorption and anomalous dispersion of the analyte in the spectral ranges of overtone transitions. The regions of enhanced and reduced transmission alternate. Figure A2a,b demonstrate the spectral regions where the counterintuitive relation between transmission of the metasurface embedded in NMA and transmission of the same metasurface embedded in immersion oil takes place. The structure covered by a dispersive and absorptive NMA film transmits more light than the same structure embedded in the transparent and dispersionless immersion oil film.
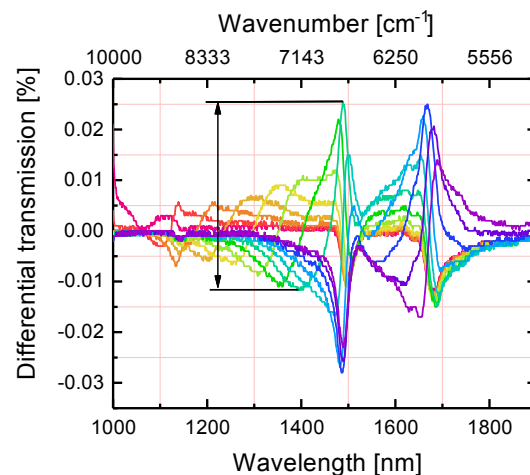
Figure 5. Differential transmission (DT) of metasurfaces with 100 nm thick analyte overlayers. The length of NPs varies from 100 (crimson curve) to 220 (purple curve) nm with steps of 10 nm while the lattice periods are of $\Lambda_1 = 400$ nm and $\Lambda_2 = 200$ nm. The DT contrast is defined as the difference between the maximum and minimum values of DT in the spectral range of the N-H overtone transition and is shown by an arrow for one of the metasurfaces.

For the sensing purposes, the difference between the DT maximum and minimum (hereinafter referred to as '*DT contrast*') is of paramount importance, since it is the variation magnitude that determines the metasurface sensitivity. Then, the enhancement factor (EF) can be expressed as $EF = \frac{DT}{DT_0}$, where DT_0 is the DT value of the same analyte film placed on a bare substrate without gold metasurface. DT_0 values were obtained via elementary calculations and presented in Figure 6a for a range of analyte film thicknesses up to $t = 100$ nm. Figure 6b shows the DT contrasts for the arrays of nanoantennas of different lengths presented in Figure 5. We note that the EF provided by metasurface utilization depends on the nanoantennas lengths. Hence, the optimization procedure is essential to maximize the EF for the particular overtone transition.
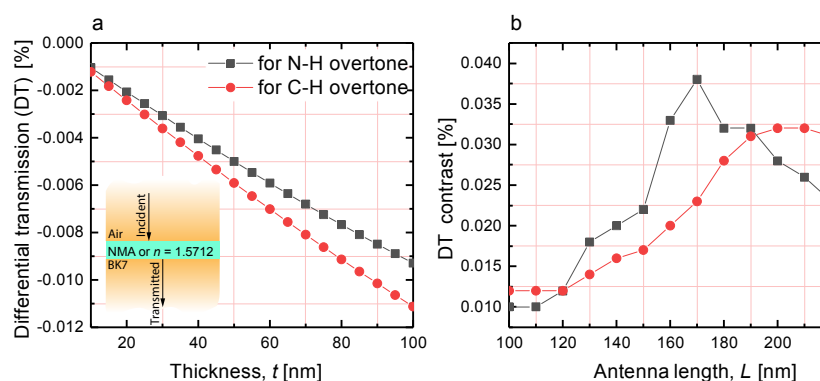
Figure 6. (**a**) DT of NMA films on a bare substrate as function of the film thickness. The insert shows the structure of the parallel films used for the calculation under the normal incidence illumination. (**b**) The DT contrast estimated from the data presented in Figure 5 as a function of the nanoantenna length.

7. Enhancement Factors of the Optimized Metasurfaces

In this section, we discuss how the DT enhancement factor depends on the lattice periods. While exploring the metasurface configuration optimized for the enhancement of the particular overtone transition, the nanoantenna lengths as well as both periods of the square lattice were varied. To reach the maximum field enhancement, the nanoantenna length that maximizes the collective polarizability at the desired wavelength was found for a number of lattice periods combinations. At the final step, the enhancement factors were calculated as presented in Figures 7 and 8. The analyte film thickness was set to 35 nm. This choice provides reasonable utilization of the near-field enhancement region. Indeed, according to Figure 4d, the maximum field enhancement is achieved at the surface of the nanoparticle and rapidly drops with the distance. Hence, from the perspective of the sensitivity enhancement, the analyte layers should not be thicker than 35 nm.
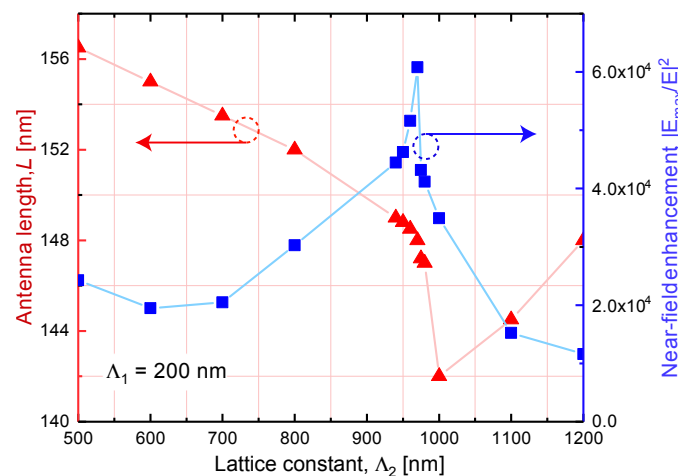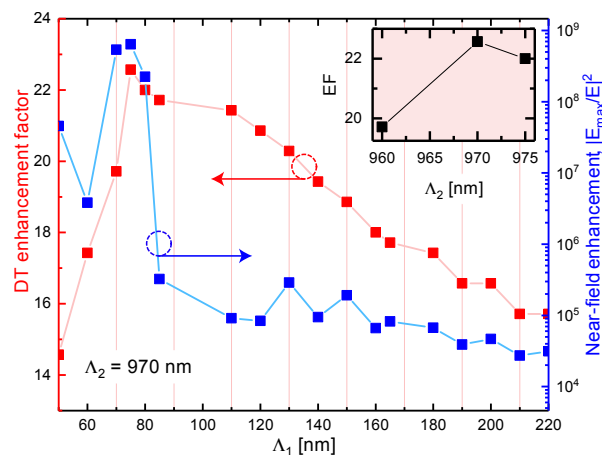

Figure 7. Variation of the local field enhancement (blue curve) and the resonant nanoantenna length L (red curve) with the lattice period Λ_2 when the other lattice period is fixed at $\Lambda_1 = 200$ nm and ensuring constant collective Localized surface plasmon resonance (LSPR) band at $\lambda = 1494$ nm. The analyte film thickness $t = 35$ nm.

The red curve in Figure 7 shows the variation of the resonant nanoantenna length L with the lattice period Λ_2 when the other lattice period is fixed at $\Lambda_1 = 200$ nm and ensuring constant collective LSPR band at $\lambda = 1494$ nm. In agreement with the numerical results presented in Figure 7, L reaches a minimum near the wavelength corresponding to the Rayleigh anomaly at about 1000 nm. Almost simultaneously, at $\Lambda_2 = 970$ nm the near-field enhancement reaches its maximum (blue curve in Figure 7). Qualitatively, this behavior may be understood as follows: if we assume that $\Lambda_2 > 996$ nm, then the first diffraction order of the radiation with the wavelength λ of 1494 nm (in vacuum) can propagate in the substrate with refractive index $n_{sub} = 1.5$. However, when $\Lambda_2 < 996$ nm, all diffraction orders becomes evanescent since $\Lambda_2 < \lambda n_{sub}$. The evanescent wave decays fast from the boundary. In addition, it carries no energy. Therefore, its amplitude may exceed the incident wave amplitude without violation of energy conservation law. This is the origin of the lattice contribution to the local field enhancement.

Subsequently, we fixed Λ_2 at 970 nm and adjusted the second lattice period Λ_1 varying it from 50 to 220 nm, as it is illustrated in Figure 8 (blue curve). Simultaneously with Λ_1 variation, the NPs length L was adjusted to keep the collective LSPR of the metasurface at the resonance with the overtone transition in NMA, as it is illustrated in Figure A3. The absolute maximum was found at $\Lambda_1 = 75$ nm that corresponds to the field enhancement of 2×10^8. Finally, we checked that this metasurface design also provides for the largest enhancement factor for sensing application which reaches an unprecedented value of 22.5 (red curve, Figure 8). To double check that the absolute maximum of the DT enhancement

factor is evaluated, we varied again the Λ_2 around the value of 970 nm. The inset of Figure 8 supports the conclusion that the absolute maximum is found.

Figure 8. Variation of the local field enhancement (blue curve) and the DT enhancement factor (EF) with the lattice period Λ_1 when the other lattice period is fixed at $\Lambda_2 = 970$ nm. The inset shows EF against the lattice constant Λ_2 at fixed $\Lambda_1 = 75$ nm. Additionally, the direction and color of the horizontal arrow indicate the corresponding axis for the red and blue curves.

8. Conclusions

In summary, we have numerically demonstrated the sensing capabilities of the rectangular lattice of gold nanoparallelepipeds on a transparent substrate while tuned on the specific transitions in the near-infrared. The shape of the metasurface unit-cells was adjusted to be readily manufacturable by electron beam lithography or focused ion beam milling. To optimize the metasurface for a particular overtone transition registration, we varied the periods of the lattice and the elements lengths simultaneously. We found that one of the optimized lattice periods is very close to that corresponding to the Rayleigh anomaly. As we are trying to anticipate the response of the actual applications, we do not place the analyte within the near-field enhancement factor maxima, but rather, as a 35 nm thick homogeneous film covering the whole metasurface. Because of that, relatively small proportion of the analyte experiences the largest field enhancement. Consequently, the structure optimized for the sensing of N-H overtone transition at 1494 nm has shown the differential transmission enhancement factor of 22.5. This rather large enhancement may be explained by the concerted action of the LSPR, the lattice resonance and the high surface density of gold nanoparticles on the substrate. Thus, we have demonstrated the way to optimize the gold metasurface for sensing the weak overtone transitions in the near-infrared. This approach may be extended for sensitive registration of other functional group overtones in the near-infrared by tailoring the lattice periods and the aspect ratios of a metasurface unit-cells.

To conclude, we leverage the rapid spectral variation of the refractive index in the spectral range of the analyte anomalous dispersion. As the anomalous dispersion is associated with its overtone absorption band, by measuring the differential transmission of a metasurface tuned to the specified spectral range the tiny amount of an analyte may be detected. In practice, several arrays of nanoparallelepipeds tuned to different spectral ranges may be fabricated on a single chip [1]. In this case, the combination of the responses of all arrays in the chip will lead to the recognition and characterization of the analyte.

Author Contributions: D.R.D. carried out the calculations and prepared the initial draft; project supervision was performed by T.A.V. and A.K. All authors discussed the results and prepared the manuscript. All authors have read and agreed to the published version of the manuscript.

Conflicts of Interest: The authors declare no conflict of interest.

Abbreviations

The following abbreviations are used in this manuscript:

NIR	Near-infrared
LSPR	Localized surface plasmon resonance
EBL	Electron beam lithography
NPs	Nanoparallelepipeds
NMA	N-Methylaniline
DT	Differential transmission
RI	Refractive index

Appendix A

Figure A1 shows the dependence of LSPR spectral position as a function of NPs length. The gold metasurface was covered by a 100 nm-thick NMA film. The long-wavelength shift of LSPR in longer nanoparticles corresponds to the known from the quasistatics theory behavior of LSPR in prolate particles.
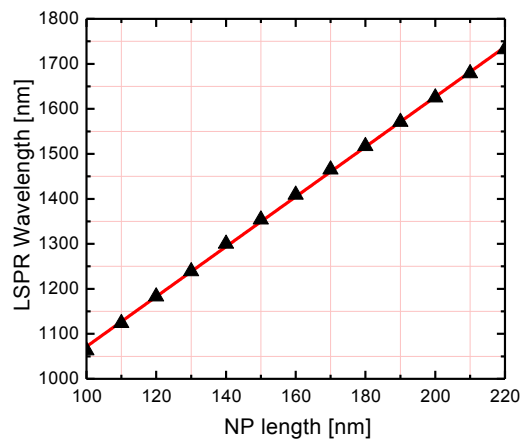
Figure A1. The LSPR spectral position as a function of NPs length *L*. The metasurface parameters were set to the following values: $w = h = 20$ nm, $t = 100$ nm, $\Lambda_1 = 400$ nm, and $\Lambda_2 = 200$ nm.

Figure A2 clarifies the origin of the negative values obtained for the differential transmission. Transmission of the NMA covered metasurface is larger than that of immersion oil covered metasurface. Transmission spectra in (a) and (b) were computed for the NPs lengths optimized for sensing of the corresponding overtone transitions.
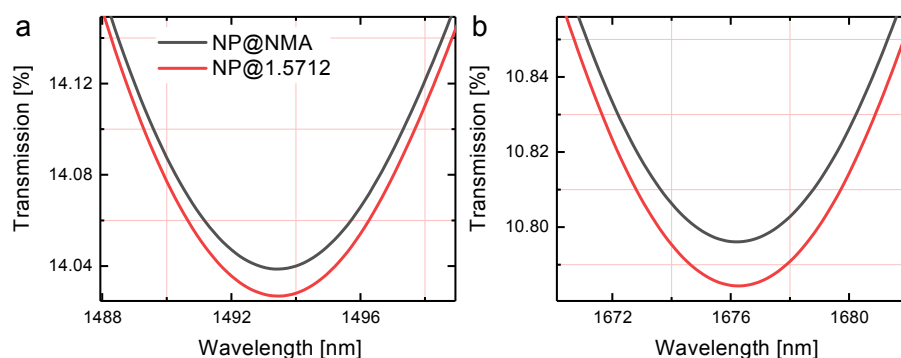
Figure A2. A closer look at the transmission spectra of metasurfaces covered by the NMA layer (black curves) and immersion oil with $n_{av} = 1.5712$ (red curves) of the same thickness $t = 35$ nm. The NPs lengths L were chosen to provide for the coincidence of the collective LSPRs of the metasurfaces with the NMA overtone transitions: (**a**) $L = 196$ nm for N-H band and (**b**) $L = 234$ nm for C-H band .

To keep the collective LSPR of a metasurface in resonance with the chosen overtone transition of NMA, the length of the NPs L must be adjusted correspondingly. Figure A3 illustrates how the length of the resonant antenna L depends on the lattice period Λ_1. As $\Lambda_1 \ll \lambda$, the Rayleigh anomaly is far away. Because of that, the resonance L depends on the inter-particle distance in the predictable from quasistatic arguments monotonic way.
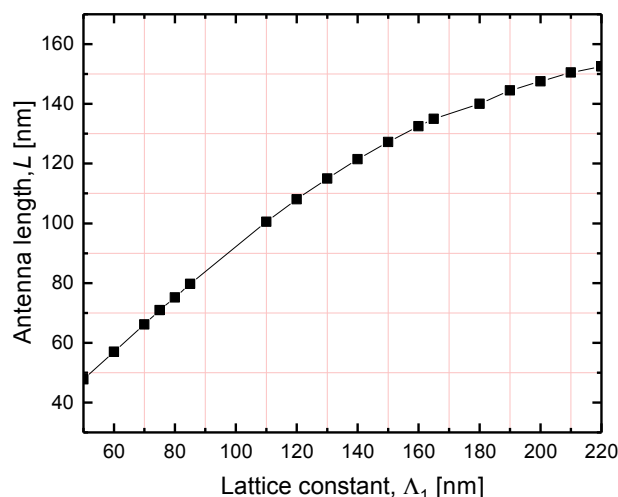
Figure A3. Dependence of the resonance antenna length L on the longitudinal lattice period Λ_1 at the fixed $\Lambda_2 = 970$ nm.

References

1. Karbchevsky, A.; Katiyi, A.; Ang, A.S.; Hazan, A. On-chip nanophotonics and future challenges. *Nanophotonics* **2020**. doi:10.1515/nanoph-2020-0204. [CrossRef]
2. Blanco, M.; Villarroya, I. NIR spectroscopy: A rapid-response analytical tool. *TrAC Trends Anal. Chem.* **2002**, *21*, 240–250. [CrossRef]
3. Siesler, H.W.; Ozaki, Y.; Kawata, S.; Heise, H.M. *Near-Infrared Spectroscopy: Principles, Instruments, Applications*; John Wiley & Sons: Hoboken, NJ, USA, 2008.
4. Katiyi, A.; Karabchevsky, A. Deflected Talbot mediated overtone spectroscopy in near-infrared as a label-free sensor on a chip. *ACS Sens.* **2020** . doi:10.1021/acssensors.0c00325. [CrossRef]
5. Ozaki, Y.; Genkawa, T.; Futami, Y. *Near-Infrared Spectroscopy*; John Wiley & Sons: Hoboken, NJ, USA, 2017.
6. Türker-Kaya, S.; Huck, C.W. A review of mid-infrared and near-infrared imaging: principles, concepts and applications in plant tissue analysis. *Molecules* **2017**, *22*, 168. [CrossRef]

7. Ozaki, Y. Near-infrared spectroscopy—Its versatility in analytical chemistry. *Anal. Sci.* **2012**, *28*, 545–563. [CrossRef]

8. Atkins, P.W.; Friedman, R.S. *Molecular Quantum Mechanics*; Oxford University Press: Oxford, UK, 2011.

9. Karabchevsky, A.; Kavokin, A. Giant absorption of light by molecular vibrations on a chip. *Sci. Rep.* **2016**, *6*, 21201. [CrossRef]

10. Katiyi, A.; Karabchevsky, A. Figure of merit of all-dielectric waveguide structures for absorption overtone spectroscopy. *J. Lightwave Technol.* **2017**, *35*, 2902–2908. [CrossRef]

11. Katiyi, A.; Zorea, J.; Halstuch, A.; Elkabets, M.; Karabchevsky, A. Surface roughness-induced absorption acts as an ovarian cancer cells growth sensor-monitor. *Biosens. Bioelectron.* **2020**, 112240. doi:10.1016/j.bios.2020.112240. [CrossRef] [PubMed]

12. Katiyi, A.; Karabchevsky, A. Si nanostrip optical waveguide for on-chip broadband molecular overtone spectroscopy in near-infrared. *ACS Sens.* **2018**, *3*, 618–623. [CrossRef] [PubMed]

13. Ray, G.J.; Anderson, T.N.; Caton, J.A.; Lucht, R.P.; Walther, T. OH sensor based on ultraviolet, continuous-wave absorption spectroscopy utilizing a frequency-quadrupled, fiber-amplified external-cavity diode laser. *Opt. Lett.* **2001**, *26*, 1870–1872. [CrossRef] [PubMed]

14. Arsad, N.; Li, M.; Stewart, G.; Johnstone, W. Intra-cavity spectroscopy using amplified spontaneous emission in fiber lasers. *J. Lightwave Technol.* **2010**, *29*, 782–788. [CrossRef]

15. Karabchevsky, A.; Katiyi, A.; Bin Abdul Khudus, M.I.M.; Kavokin, A.V. Tuning the Near-Infrared Absorption of Aromatic Amines on Tapered Fibers Sculptured with Gold Nanoparticles. *ACS Photonics* **2018**, *5*, 2200–2207. [CrossRef]

16. Borovkova, O.; Ignatyeva, D.; Sekatskii, S.; Karabchevsky, A.; Belotelov, V. High-Q surface electromagnetic wave resonance excitation in magnetophotonic crystals for supersensitive detection of weak light absorption in the near-infrared. *Photonics Res.* **2020**, *8*, 57–64. [CrossRef]

17. Klimov, V. *Nanoplasmonics*; CRC Press: Boca Raton, FL, USA, 2014.

18. Chen, H.; Shao, L.; Li, Q.; Wang, J. Gold nanorods and their plasmonic properties. *Chem. Soc. Rev.* **2013**, *42*, 2679–2724. [CrossRef] [PubMed]

19. Giannini, V.; Fernández-Domínguez, A.I.; Heck, S.C.; Maier, S.A. Plasmonic nanoantennas: fundamentals and their use in controlling the radiative properties of nanoemitters. *Chem. Rev.* **2011**, *111*, 3888–3912. [CrossRef] [PubMed]

20. Dadadzhanov, D.R.; Vartanyan, T.A.; Karabchevsky, A. Vibrational overtones spectroscopy enabled by plasmonic nanoantennas. In *Plasmonics: Design, Materials, Fabrication, Characterization, and Applications XVI*; International Society for Optics and Photonics: Bellingham, WA, USA, 2018; Volume 10722, p. 107222E.

21. Dadadzhanov, D.R.; Vartanyan, T.A.; Karabchevsky, A. Differential extinction of vibrational molecular overtone transitions with gold nanorods and its role in surface enhanced near-IR absorption (SENIRA). *Opt. Express* **2019**, *27*, 29471–29478. [CrossRef] [PubMed]

22. Dadadzhanov, D.R.; Vartanyan, T.A.; Dadadzhanova, A.I.; Karabchevsky, A. Surface-enhanced near-infrared absorption (SENIRA) of CH and NH groups with gold nanoarray. In *Quantum Sensing and Nano Electronics and Photonics XVII*; International Society for Optics and Photonics: Bellingham, WA, USA, 2020; Volume 11288, p. 1128816.

23. Humphrey, A.; Barnes, W. Plasmonic surface lattice resonances in arrays of metallic nanoparticle dimers. *J. Optics* **2016**, *18*, 035005. [CrossRef]

24. Kravets, V.G.; Kabashin, A.V.; Barnes, W.L.; Grigorenko, A.N. Plasmonic surface lattice resonances: A review of properties and applications. *Chem. Rev.* **2018**, *118*, 5912–5951. [CrossRef]

25. Kravets, V.; Schedin, F.; Kabashin, A.; Grigorenko, A. Sensitivity of collective plasmon modes of gold nanoresonators to local environment. *Opt. Lett.* **2010**, *35*, 956–958. [CrossRef]

26. Auguié, B.; Barnes, W.L. Collective resonances in gold nanoparticle arrays. *Phys. Rev. Lett.* **2008**, *101*, 143902. [CrossRef]

27. Chen, P.Y.; Muljarov, E.A.; Sivan, Y. Lightning-fast solution of scattering problems in nanophotonics: An effortless modal approach (Conference Presentation). In *Nanophotonics VIII*; International Society for Optics and Photonics: Bellingham, WA, USA, 2020; Volume 11345, p. 113450T.

28. Norman, J.C.; DeJarnette, D.F.; Roper, D.K. Polylogarithm-based computation of Fano resonance in arrayed dipole scatterers. *J. Phys. Chem. C* **2014**, *118*, 627–634. [CrossRef]

29. Kanipe, K.N.; Chidester, P.P.; Stucky, G.D.; Meinhart, C.D.; Moskovits, M. Properly structured, any metal can produce intense surface enhanced Raman spectra. *J. Phys. Chem. C* **2017**, *121*, 14269–14273. [CrossRef]

30. Wang, D.; Guan, J.; Hu, J.; Bourgeois, M.R.; Odom, T.W. Manipulating light–matter interactions in plasmonic nanoparticle lattices. *Acc. Chem. Res.* **2019**, *52*, 2997–3007. [CrossRef]

31. Cherqui, C.; Bourgeois, M.R.; Wang, D.; Schatz, G.C. Plasmonic Surface Lattice Resonances: Theory and Computation. *Acc. Chem. Res.* **2019**, *52*, 2548–2558. [CrossRef] [PubMed]

32. Manjavacas, A.; Zundel, L.; Sanders, S. Analysis of the Limits of the Near-Field Produced by Nanoparticle Arrays. *ACS Nano* **2019**, *13*, 10682–10693. [CrossRef] [PubMed]

33. Yokota, Y.; Ueno, K.; Mizeikis, V.; Juodkazis, S.; Sasaki, K.; Misawa, H. Optical characterization of plasmonic metallic nanostructures fabricated by high-resolution lithography. *J. Nanophotonics* **2007**, *1*, 011594.

34. Grand, J.; Adam, P.M.; Grimault, A.S.; Vial, A.; De La Chapelle, M.L.; Bijeon, J.L.; Kostcheev, S.; Royer, P. Optical extinction spectroscopy of oblate, prolate and ellipsoid shaped gold nanoparticles: experiments and theory. *Plasmonics* **2006**, *1*, 135–140. [CrossRef]

35. Luypaert, J.; Massart, D.; Vander Heyden, Y. Near-infrared spectroscopy applications in pharmaceutical analysis. *Talanta* **2007**, *72*, 865–883. [CrossRef]

36. Nicolai, B.M.; Beullens, K.; Bobelyn, E.; Peirs, A.; Saeys, W.; Theron, K.I.; Lammertyn, J. Nondestructive measurement of fruit and vegetable quality by means of NIR spectroscopy: A review. *Postharvest Biol. Technol.* **2007**, *46*, 99–118. [CrossRef]

37. Prieto, N.; Pawluczyk, O.; Dugan, M.E.R.; Aalhus, J.L. A review of the principles and applications of near-infrared spectroscopy to characterize meat, fat, and meat products. *Appl. Spectrosc.* **2017**, *71*, 1403–1426. [CrossRef]

38. Dos Santos, C.A.T.; Lopo, M.; Páscoa, R.N.; Lopes, J.A. A review on the applications of portable near-infrared spectrometers in the agro-food industry. *Appl. Spectrosc.* **2013**, *67*, 1215–1233. [CrossRef] [PubMed]

39. Xia, Y.; Xu, Y.; Li, J.; Zhang, C.; Fan, S. Recent advances in emerging techniques for non-destructive detection of seed viability: A review. *Artif. Intell. Agric.* **2019**, *1*, 35–47. [CrossRef]

40. Shaji, S.; Eappen, S.M.; Rasheed, T.; Nair, K. NIR vibrational overtone spectra of N-methylaniline, N, N-dimethylaniline and N, N-diethylaniline—A conformational structural analysis using local mode model. *Spectrochim. Acta Part A Mol. Biomol. Spectrosc.* **2004**, *60*, 351–355. [CrossRef]

41. Karabchevsky, A.; Shalabney, A. Strong interaction of molecular vibrational overtones with near-guided surface plasmon polariton. In *Optical Sensing and Detection IV*; International Society for Optics and Photonics: Bellingham, WA, USA, 2016

42. Johnson, P.B.; Christy, R.W. Optical constants of the noble metals. *Phys. Rev. B* **1972**, *6*, 4370–4379. doi:10.1103/PhysRevB.6.4370. [CrossRef]

43. Stietz, F.; Bosbach, J.; Wenzel, T.; Vartanyan, T.; Goldmann, A.; Träger, F. Decay times of surface plasmon excitation in metal nanoparticles by persistent spectral hole burning. *Phys. Rev. Lett.* **2000**, *84*, 5644. [CrossRef] [PubMed]

44. Bosbach, J.; Hendrich, C.; Stietz, F.; Vartanyan, T.; Träger, F. Ultrafast dephasing of surface plasmon excitation in silver nanoparticles: influence of particle size, shape, and chemical surrounding. *Phys. Rev. Lett.* **2002**, *89*, 257404. [CrossRef]

45. SCHOTT Glass Database. Number 517642.251. Available online: https://www.schott.com/d/advanced_optics/ac85c64c-60a0-4113-a9df-23ee1be20428/1.17/schott-optical-glass-collection-datasheets-english-may-2019.pdf (accessed on 1 February 2014).

46. Zundel, L.; Manjavacas, A. Finite-size effects on periodic arrays of nanostructures. *J. Phys. Photonics* **2018**, *1*, 015004. [CrossRef]

47. Sung, J.; Hicks, E.M.; Van Duyne, R.P.; Spears, K.G. Nanoparticle spectroscopy: Plasmon coupling in finite-sized two-dimensional arrays of cylindrical silver nanoparticles. *J. Phys. Chem. C* **2008**, *112*, 4091–4096. [CrossRef]

48. Matsushima, A. Effect of periodicity in the light scattering from infinite and finite arrays of silver nanospheres. In Proceedings of the 2017 IEEE International Conference on Computational Electromagnetics (ICCEM), Kumamoto, Japan, 8–10 March 2017; pp. 236–237.

49. Born, M.; Wolf, E. *Principles of Optics: Electromagnetic Theory of Propagation, Interference and Diffraction of Light*; Elsevier: Amsterdam, The Netherlands, 2013.

50. Shen, H.; Bienstman, P.; Maes, B. Plasmonic absorption enhancement in organic solar cells with thin active layers. *J. Appl. Phys.* **2009**, *106*, 073109. [CrossRef]

51. Starovoytov, A.A.; Nabiullina, R.D.; Gladskikh, I.A.; Polischuk, V.A.; Parfenov, P.S.; Kamalieva, A.N. Plasmon-exciton interaction in the thin film of inhomogeneous ensemble of silver nanoparticles and cyanine J-aggregates. In *Nanophotonics VII*; International Society for Optics and Photonics: Bellingham, WA, USA, 2018; Volume 10672, p. 106723O.

תקציר

חיישנים ללא סמנים, המשמשים ככלי אנליטי, נחקרו בצורה נרחבת על ידי חוקרים רבים במהלך העשורים האחרונים בגלל מהפוטנציאל הגבוה שלהם ליישומים של חיישנים כימיים וביולוגיים. חיישנים אלו מאפשרים זיהוי בזמן אמת של אינטראקציות עם חומרים שונים ברגישות גבוה ובלי צורך בסמנים. אחת מהשיטות הייחודיות של חישה כימית וביולוגית ללא סמן מבוססת על אוסף אוסילציות של אלקטרונים חופשיים – פלזמוני שטח. ניתן לעורר פלזמוני שטח בחומרים מוליכים ננומטריים המורכבים ממתכות, בהינתן שגודל האובייקט קטן מאוד מאורך הגל של האור הפוגע בו[1]. הננו־חלקיקים פלזמונים יוצרים את הבסיס למערכות חיישנים הנקראים חיישני תהודת פלזמון משטחיית כתוצאה מהרגישות הגבוהה לסביבה דיאלקטרית והשדה אלקטרומגנטי המרוכז בסביבתם. בנוסף, התכונות האופטיות של ננו־חלקיקים מתכתיים תלויות באופן משמעותי בצורה שלהם. תלות זאת מאפשרת כיוונון של התדר של הפלזמונים המקומיים על מנת ליצור אינטראקציה יעילה של חומרים כימיים וביולוגיים [2]. כתוצאה מהעצמה של השדות החשמליים המקומיים, הננו־חלקיקים הפלזמונים משמשים באופן נרחב בהרבה תחומים ביניהם אופטיקה לא־ליניארית, ספקטרוסקופיה ראמן, ואחרים. ננו־חלקיקים מתכתיים יכולים לשמש לפתרון בעיות שונות ברפואה, ביולוגיה, אלקטרוניקה ופוטוניקה. מטרת הדוקטורט היא ניתוח תאורטי וידוי ניסויי של האינטראקציה של ננו־חלקיקים פלזמונים ממתכות אציליות בין פולט קוונטי, בולע קוונטי וחומר ביולוגי.

אוניברסיטת בן־גוריון בנגב

הפקבית הספר להנדסת חשמל ומחשבים היחידה להנדסת אלקטרואופטיקה ופוטוניקה

שננואנטנות אופטיות לאפליקציות של חיישנים כימיים וביולוגיים

מחקר לשם מילוי חלקי של הדרישות לקבלת תואר "דוקטור לפילוסופיה"

דלר דאדאדזאנוב

הוגש לסינאט אוניברסיטת בן גוריון בנגב

אקטאבבער 2020

אוניברסיטת בן-גוריון בנגב

הפקבית הספר להנדסת חשמל ומחשבים היחידה להנדסת אלקטרואופטיקה ופוטוניקה

שננואנטנות אופטיות לאפליקציות של חיישנים כימיים וביולוגיים

מחקר לשם מילוי חלקי של הדרישות לקבלת תואר "דוקטור לפילוסופיה"

דלר דאדאדזאנוב

הוגש לסינאט אוניברסיטת בן גוריון בנגב

25/10/2020

אישור המנחה _____

אישור דיקן בית הספר ללימודי מחקר מתקדמים ע"ש קרייטמן _____

אקטאבבער 2020

העבודה נעשתה בהדרכת

במחלקה _____

בפקולטה _____

<u>הצהרת תלמיד המחקר עם הגשת עבודת הדוקטור לשיפוט</u>

אני החתום מטה מצהיר/ה בזאת:

חיברתי את חיבורי בעצמי, להוציא עזרת ההדרכה שקיבלתי מאת מנחה/ים.

החומר המדעי הנכלל בעבודה זו הינו פרי מחקרי מתקופת היותי תלמיד/ת מחקר

בעבודה נכלל חומר מחקרי שהוא פרי שיתוף עם אחרים, למעט עזרה טכנית הנהוגה בעבודה ניסיונית. לפי כך מצורפת בזאת הצהרה על תרומתי ותרומת שותפי למחקר, שאושרה על ידם ומוגשת בהסכמתם.

תאריך : ___25/10/2020___ שם התלמיד/ה : ___Dadadzhanov D.R.___ חתימה: _____

2

Ben-Gurion University of the Negev

School of Electrical and Computer Engineering

Electro-Optics and Photonics Engineering Department

Optical nanoantennas for applications in label-free chemical and biological sensors

Thesis submitted in partial fulfillment of the requirements

for the degree of "DOCTOR OF PHILOSOPHY"

by

Daler R. Dadadzhanov

Submitted to the Senate of Ben-Gurion University of the Negev

October 2020

Beer-Sheva

Ben-Gurion University of the Negev

School of Electrical and Computer Engineering

Electro-Optics and Photonics Engineering Department

Optical nanoantennas for applications in label-free chemical and biological sensors

Thesis submitted in partial fulfillment of the requirements

for the degree of "DOCTOR OF PHILOSOPHY"

by

Daler R. Dadadzhanov

Submitted to the Senate of Ben-Gurion University of the Negev

Approved by the advisor   25/10/2020

Approved by the Dean of the Kreitman School of Advanced Graduate Studies

October 2020

Beer-Sheva

This work was carried out under the supervision of Dr. Alina Karabchevsky and Dr. Tigran Vartanyan

In the Electro-Optics and Photonics Engineering Department

Research-Student's Affidavit when Submitting the Doctoral Thesis for Judgment

I Daler Dadadzhanov, whose signature appears below, hereby declare that

I have written this Thesis by myself, except for the help and guidance offered by my Thesis Advisors.

The scientific materials included in this Thesis are products of my own research, culled from the period during which I was a research student.

This Thesis incorporates research materials produced in cooperation with others, excluding the technical help commonly received during experimental work. Therefore, I am attaching another affidavit stating the contributions made by myself and the other participants in this research, which has been approved by them and submitted with their approval.

Date: 25/10/2020   Student's name: Dadadzhanov D.R.   Signature: _____